AN ABSTRACT OF THE DISSERTATION OF

Chad N Teters for the degree of Doctor of Philosophy in Chemistry presented

on September 4, 2009

Title: The Transient Electric Birefringence of Nanomaterials: Alignment Mechanism, Characterization, and its Application Towards Aligned Polymer Nanocomposites.

Abstract approved:

Wei Kong

The experimental and theoretical bases of transient electric birefringence (TEB) and its application in a variety of nanomaterials, including Na-montmorillonite, cellulose nanocrystals (CNXL), and CdSe quantum dots (QDs) will be presented. TEB is a phenomenon attributed to the alignment of particles in response to an applied electric field and has been used for the determination of particle sizes, optical anisotropies, polarizability anisotropies $\Delta\alpha$, and permanent dipole moments μ. In this thesis, I will present the relations between the physical parameters just mentioned and the experimental measurements of the rise, saturation, and decay of particle alignment. Detailed experimental setup and data analysis procedures will also be discussed. In the case of Na-montmorillonite, our findings imply a wide size and shape distribution and that the shape of the material is best modeled somewhere between a rod and a disk. The alignment mechanism was dominated by an induced-dipole, with some of the data suggesting the presence of a small permanent dipole; however, the later findings were inconclusive. CNXL, on the other hand, is shown to be polydisperse

only in size and is modeled well as a rigid rod. At intermediate field strength, the alignment response was governed by both an induced (~95%) and permanent moment (~5%). CNXL was also shown to produce very large birefringence, owing to its equally large optical anisotropy. CdSe QDs are nearly monodisperse in both size and shape, and are an ideal representation of a rigid rod. Their alignment mechanism contained a large permanent dipole contribution (~88%), which is attributed to their wurtzite crystalline structure. In the last chapter, preliminary results on nanocomposites containing carbon nanotubes (CNTs) and QDs are presented. Results for the nanoparticles in polylaurylmethacrylate are promising. TEM images of both composites showed a net alignment of particles in the field direction. However, aggregation of the CNTs in the polymer was a problem and further work is needed to keep them adequately exfoliated during the curing process. Aggregation of the QDs was not observed.

The Transient Electric Birefringence of Nanomaterials: Alignment Mechanism, Characterization, and its Application Towards Aligned Polymer Nanocomposites.

by
Chad N Teters

A DISSERTATION

Submitted to

Oregon State University

in partial fulfillment of
the requirements for the
degree of

Doctor of Philosophy

Presented September 4, 2009
Commencement June 2010

Doctor of Philosophy dissertation of Chad N Teters presented on September 4, 2009.

APPROVED:

Major Professor, representing Chemistry

Chair of the Department of Chemistry

Dean of the Graduate School

I understand that my dissertation will become part of the permanent collection of Oregon State University libraries. My signature below authorizes release of my dissertation to any reader upon request.

Chad N Teters, Author

ACKNOWLEGEMENTS

I would like to express my deepest appreciation to my advisor, Dr Wei Kong, for the consistent support and guidance she gave me throughout my graduate career. Wei, thank you for your unwavering belief in my ability and the encouragement you gave me when I needed it most. I've come to respect Dr Kong not only for her exceptional skill as an experimentalist, but also as a person, whose character I hope to pattern in my own life. I would also like to thank the following:

- Dr Joseph Nibler – for the use of equipment that was essential for my research and for numerous discussions which often helped resolve key issues.
- Dr Glenn Evans – for developing the field dependent alignment theory, which I used as a component of the theoretical analysis presented here.
- Dr John Simonsen – for supplying me with a key component of my research (cellulose nanocrystals) and for numerous discussions which helped me understand their properties.
- Dr Philip Watson – for serving on my committee, along with the professors just mentioned.
- Jessica – for being a great group member and helping me out in the lab when I needed an extra hand.
- Francis – for writing the computer program I used for fitting much of my data.

Finally, I would like to thank my daughters, Allie and Cassie, for being my biggest fans and repeating their mantra "you can do it dad," which was often the greatest motivator when I doubted myself most. I love you guys!

TABLE OF CONTENTS

TABLE OF CONTENTS (Continued)

Page

TABLE OF CONTENTS (Continued)

Page

TABLE OF CONTENTS (Continued)

Page

LIST OF FIGURES

LIST OF FIGURES (Continued)

LIST OF FIGURES (Continued)

LIST OF FIGURES (Continued)

LIST OF FIGURES (Continued)

LIST OF TABLES

The Transient Electric Birefringence of Nanomaterials: Alignment Mechanism, Characterization, and its Application Towards Aligned Polymer Nanocomposites

1. Overview

1.1. Literature Review

Optical anisotropy was discovered at the end of the nineteenth and beginning of the twentieth century. In the 1870s Maxwell observed the flow birefringence of Canada balsam, and the technique played a prominent role in the study of artificially induced birefringence for several years.[1] Studies of the magnetic birefringence effect, discovered by Kerr (1901), were extended by Cotton and Mouton (1907) on colloidal solutions of ferric hydroxide.[2-5] However, there has been limited advancement in the field past the work of Mekshenkov (1965).[6-8] The electric birefringence effect was first observed in 1875 by Kerr who further established the proportionality of the birefringence to the square of the field strength.[9] For the next several decades, the study of electric birefringence was restricted to pure liquids and colloidal solutions using high DC voltages and sinusoidal fields. Limited by their conductivity, biological macromolecules in aqueous solutions were studied only after pulsed techniques had been developed.

The invention of the oscilloscope further accelerated the development of pulsed techniques further, and in 1947 Kaye and Devaney described a generator producing sequential rectangular pulses.[10] Tolstoi and Feofilov also developed the use of this technique for colloidal solutions and drew attention to its potential for use

in the study of relaxation processes.[11] Because of its large size and strong birefringence, tobacco mosaic virus (TMV) was the first biological macromolecule to be investigated. In the 1950s, Benoit investigated aqueous solutions of TMV, DNA, and vanadium pentoxide using a mechanical switch for pulse generation.[12, 13] He also derived the basic theory of the transient phenomena for the build-up and decay of the birefringence.

A series of articles devoted to the study of the transient electric birefringence (TEB) of macromolecules was published by the O'Konski group at Berkeley.[14] The use of a single pulse to orient the particles, in place of a train of pulses, strongly reduced electrolysis and heating effects which were particularly critical in the study of aqueous solutions. Shortly after O'Konski's work, several reviews concerning the Kerr effect in liquids, polymers, and proteins, were published.[15-18]

In more recent years, TEB has become the standard form of measurement for many solutions which show promise in the electronic display industry.[19-21] The reason for this is that the technique provides a simple method for the determination of a solution's Kerr constant. The Kerr constant is defined as $K = \Delta n/\lambda E^2$ and is an important physical parameter of a solution; as a higher value for the Kerr constant allows for more complete transmission of light to be achieved with a smaller applied electric field (a phenomenon that will be addressed in detail in a later section).

The fundamental theoretical framework on TEB was established by Langevin (1908)[22] and Born (1918),[23] and later developed in more detail by Peterlin and Stuart (1939).[24-29] The basic assumption of the theory is orientation of the particles

under the influence of the external electric field through their permanent and/or induced-dipole moments. Further extensions of the basic theory, including saturation behavior at high fields, were addressed by O'Konski, Yoshioka, and Orttung (1959).[30-33]

1.2. References

1. Serdyuk, I.N., et al., *Methods in molecular biophysics*. 2007, New York: Cambridge University Press.

2. Cotton, A. and H. Mouton, *Magnetic Birefringence of Pure Liquids.* Phys. Z., 1912. **12**: p. 953-5.

3. Cotton, A. and H. Mouton, *The Magnetic Double Refraction of Pure Liquids. Comparison with the Electro-optical Phenomenon of Kerr.* J. physique, [5] , 1911. **1**: p. 60-73.

4. Cotton, A. and H. Mouton, *Absolute Measurement of the Magnetic Double Refraction of Nitrobenzene.* Compt. rend., 1911. **151**: p. 862-4.

5. Cotton, A. and H. Mouton, *A New Optical Property (Magnetic Double Refraction) of Certain Non-Colloidal Organic Liquids.* Compt. rend. , 1907. **145**: p. 229-30.

6. Mekshenkov, M.I., *Theory of the Cotton-Mouton effect in polymer solutions. II. Model of a wormlike chain.* Biofizika , 1967. **12**(1): p. 157-9.

7. Mekshenkov, M.I., *Study of the structure and conformation of ribonucleic acids by the birefringence method in magnetic field.* Biofizika , 1965. **10**(5): p. 747-54.

8. Mekshenkov, M.I., *Magneto-Optic Effects in Nucleic Acid Solutions.* Biofizika , 1964. **9**: p. 128-31.

9. Hecht, E., *Optics*. 4th ed. 2002, Upper Saddle River: Pearson Education, Inc.

10. Fredericq, E. and C. Houssier, *Electric Dichroism and Electric Birefringence*. 1973, Clarendon: Oxford.

11. Skanavi, G.I., et al., *Application of the new method of investigation of relaxation processes to the study of relaxation polarization of dielectrics.* Zh. Eksp. Teor. Fiz. , 1949. **19**: p. 1121-9.

12. Benoit, H., *Electric birefringence of thymonucleic acid.* Journal de Chimie Physique et de Physico-Chimie Biologique, 1951. **48**: p. 612-14.

13. Benoit, H., *The Kerr effect demonstrated by dilute solutions of rigid macromolecules.* Ann. phys., 1951. **6**: p. 561-609.

14. O'Konski, C.T. and A.J. Haltner, *Characterization of the monomer and dimer of tobacco-mosaic virus by transient electric birefringence.* J. Am. Chem. Soc. , 1956. **78**: p. 3604-10.

15. Cathou, R.E. and C.T. O'Konski, *Transient electric birefringence study of the structure of specific IgG antibody.* J. Mol. Biol. , 1970. **48**(1): p. 125-31.

16. Yoshioka, K. and C.T. O'Konski, *Electric properties of macromolecules. XIII. Transient electric birefringence of sodium poly(ethylenesulfonate) solutions.* J. Polym. Sci., Polym. Phys. Ed. , 1968. **6**(2): p. 421-31.

17. Yoshioka, K. and C.T. O'Konski, *Electric properties of macromolecules. IX. Dipole moment, polarizability, and optical anisotropy factor of collagen in solution from electric birefringence.* Biopolymers , 1966. **4**(5): p. 499-507.

18. Krause, S. and C.T. O'Konski, *Electric properties of macromolecules. VIII. Kerr constants and rotational diffusion of some proteins in water and in glycerol-water solutions.* Biopolymers, 1963. **1**(6): p. 503-15.

19. Ge, Z., et al., *Electro-optics of polymer-stabilized blue phase liquid crystal displays.* Appl. Phys. Lett., 2009. **94**(10): p. 101104/1-101104/3.

20. Choi, S.-W., et al., *Optically isotropic-nanostructured liquid crystal composite with high Kerr constant.* Appl. Phys. Lett., 2008. **92**(4): p. 043119/1-043119/3.

21. Khoshsima, H., et al., *Kerr effect investigations in liquid crystals containing the isothiocyanato and cyano groups with identical flexible tails.* Mol. Cryst. Liq. Cryst., 2006. **460**: p. 93-106.

22. Langevin, P., *Theory of the Brownian Movement.* Compt. rend., 1908. **146**: p. 530.

23. Born, M., *The electronic theory of the natural optical activity of isotropic and anisotropic liquids.* Ann. Phys. (Berlin, Ger.), 1918. **55**: p. 177-240.

24. Peterlin, A., *Influence of solvent on the optical anisotropy of macromolecules.* Makromol. Chem., 1954. **13**: p. 102.

25. Peterlin, A., *The shape of the linear unbranched macromolecule in solution.* Bull. Soc. Chim. Belg., 1951. **No. Jugilaire 1897-1947**: p. 215-31.

26. Stuart, H.A. and A. Peterlin, *Optical anisotropy and shape of chain molecules. I. Depolarization of light scattered in solution. II. Birefringence.* J. Polym. Sci., 1950. **5**: p. 543-9,551-63.

27. Peterlin, A. and H.A. Stuart, *Effect of the restriction of rotation and of anisotropy of the internal field on the polarization of liquids.* Z. Phys., 1939. **113**: p. 663-96.

28. Peterlin, A. and H.A. Stuart, *The determination of the size and shape, as well as the electrical, optical and magnetic anisotropy of submicroscopic particles with the aid of artificial double refraction and inner viscosity.* Z. Phys., 1939. **112**: p. 129-47.

29. Peterlin, A. and H.A. Stuart, *The theory of streaming double refraction of colloids and of large molecules in solution.* Z. Phys., 1939. **112**: p. 1-19.

30. Orttung, W.H. and J.A. Meyers, *The Kerr constant of water.* J. Phys. Chem., 1963. **67**(9): p. 1905-10.

31. Orttung, W.H. and J.M. Orttung, *The Kerr constants of aqueous solutions of glycine peptides.* J Phys Chem, 1970. **74**(10): p. 2143-7.

32. Orttung, W.H., *Anisotropy of proton fluctuations and the Kerr effect of protein solutions. Theoretical considerations.* J Phys Chem, 1968. **72**(12): p. 4058-66.

33. Orttung, W.H., *Evidence for a Permanent Dipole Moment in Hemoglobin from Kerr Effect Optical Dispersion.* J Am Chem Soc, 1965. **87**: p. 924-6.

2. Propagation of Light

Propagation of an electromagnetic wave through a vacuum or a dielectric material is described using Maxwell's equations. The following section follows the discussion by Fowles and highlights the basic theory behind the interaction of light with anisotropic systems.[1]

2.1. Propagation of Light in an Isotropic Medium

In an isotropic, nonconducting medium, the electrons are bound to the atoms with no preferential direction or orientation. Thus, if the electrons are displaced some distance r from their equilibrium position by a static field E, the resulting polarization of the medium is given by:

$$P = \frac{Ne^2}{K} E \qquad \textbf{(2.1)}$$

where N is the number of electrons, and K is the force constant that equals $-eE/r$. If the field varies with time, the following differential equation of motion results:

$$m\frac{d^2 r}{dt^2} + my\frac{dr}{dt} + Kr = -eE \qquad \textbf{(2.2)}$$

where my is a proportionality constant which accounts for the frictional damping force experienced by the electrons. Assuming that the field affecting the electrons varies harmonically as $e^{-i\omega t}$, Eq. **(2.2)** becomes:

$$\left(-m\omega^2 - i\omega my + K\right)r = -eE \tag{2.3}$$

and the polarization represented by **(2.1)** is given by:

$$P = \frac{Ne^2}{-m\omega^2 - i\omega my + K}E \tag{2.4}$$

When $\omega = 0$, Eq. **(2.4)** reduces to the static field scenario represented by Eq. **(2.1)**. A more physically important representation of Eq. **(2.4)** can be established by introducing the resonant frequency ω_o of the bound electrons:

$$P = \frac{Ne^2/m}{\omega_o^2 - \omega^2 + i\omega y}E \tag{2.5}$$

where $$\omega_o = \sqrt{K/m} \tag{2.6}$$

The resonance frequency is intrinsic to the dielectric material and corresponds to the frequency of strong absorption.

The polarization of a non-conducting medium constitutes the source in the general wave equation:

$$\nabla \times \left(\nabla \times E\right) + \frac{1}{c^2}\frac{\partial^2 E}{\partial t^2} = -\mu_o \frac{\partial^2 P}{\partial t^2} \tag{2.7}$$

Substituting Eq. **(2.5)** for the polarization, the right side of Eq. **(2.7)** becomes:

$$\frac{-\mu_o Ne^2}{m}\left(\frac{1}{\omega_o^2 - \omega^2 + -i\omega y}\right)\frac{\partial^2 E}{\partial t^2} \tag{2.8}$$

A general solution to Eq. **(2.7)** is a planar harmonic wave:

$$E = E_o e^{i(Kz-\omega t)} \tag{2.9}$$

with a wave number $\mathscr{K}$ expressed as:

$$K^2 = \frac{\omega^2}{c^2}\left(1+\frac{Ne^2}{m\varepsilon_o}\cdot\frac{1}{\omega_o^2-\omega^2-iy\omega}\right) \tag{2.10}$$

The real and complex parts of $\mathscr{K}$ can be represented as:

$$K = k+i\alpha \tag{2.11}$$

By substituting the right side of Eq. **(2.11)** into the plane wave expressed by Eq. **(2.9)**, the general solution can now be re-written as:

$$E = E_o e^{\alpha z} e^{i(kz-\omega t)} \tag{2.12}$$

The factor $e^{-\alpha z}$ indicates that the amplitude decreases exponentially with distance. Thus, as the wave moves through the medium, its energy is absorbed. Given that the energy is proportional to $|E|^2$, 2α is termed the coefficient of absorption of the medium. The phase factor $e^{i(kz-\omega t)}$ indicates that the phase velocity v is:

$$v = \frac{\omega}{k} = \frac{c}{n} \tag{2.13}$$

Eq. **(2.13)** represents the relation between the refractive index n, the wave vector k, and the speed of light c. The refractive index $\mathscr{N}$ is defined as the ratio of the speed of

light in vacuum to its speed in a medium ($n = c/v$), and it can be expressed in a similar fashion to the complex wave vector $\mathscr{K}$ where:

$$N = n + i\kappa \tag{2.14}$$

and that:

$$K = \frac{\omega}{c} N \tag{2.15}$$

Thus the imaginary portion of the complex index of refraction $\mathscr{N}$ is termed the extinction coefficient κ and is related to α. From Eq. **(2.10)** and Eq. **(2.15)**, we can obtain:

$$n = 1 + \frac{Ne^2}{2m\varepsilon_o}\left(\frac{\omega_o^2 - \omega^2}{(\omega_o^2 - \omega^2)^2 + y^2\omega^2}\right) \tag{2.16}$$

$$\kappa = \frac{Ne^2\omega}{2m\varepsilon_o}\left(\frac{y^2\omega^2}{(\omega_o^2 - \omega^2)^2 + y^2\omega^2}\right) \tag{2.17}$$

Finally, if the frictional damping constant is sufficiently small, the term $y^2\omega^2$ can be neglected and Eq. **(2.16)** simplifies to:

$$n = 1 + \frac{Ne^2}{8\pi^2 m\varepsilon_o}\left(\frac{1}{\nu_o^2 - \nu^2}\right) \tag{2.18}$$

where the denominator has been multiplied by $4\pi^2$ in changing from angular frequency to normal frequency.

2.2. Propagation of Light in an Anisotropic Medium

Many crystalline substances in nature are optically anisotropic. If a crystal's lattice is not completely symmetric then the binding forces on the electrons are not equal in all directions. A crystal which displays anisotropy in the electronic binding force is termed birefringent. Birefringent crystals belonging to the hexagonal, tetragonal, and trigonal groups are termed "uniaxial," having their atoms arranged in such a way that there is a single optical axis which corresponds to a direction about which the atoms are arranged symmetrically. There also exist biaxial crystals, having two optical axes and three refractive indices. Although interesting, the discussion of biaxial crystals will be avoided, as they have little relevance to the current study. Cubic crystals like sodium chloride display no birefringence, owing to their relatively simple and highly symmetric structure. Their lattice contains four 3-fold symmetry axes so light emanating from a point source within the structure will propagate uniformly in all directions. Such a material will have a single index of refraction and be optically isotropic.

An illustration of the anisotropic polarizability of a crystal is shown in **Figure 2.1**, where an electron is pictured as being attached to fictitious springs. The springs are of varying stiffness as they extend in different directions, representing the varying forces exerted on the electron as it is displaced from its equilibrium position.

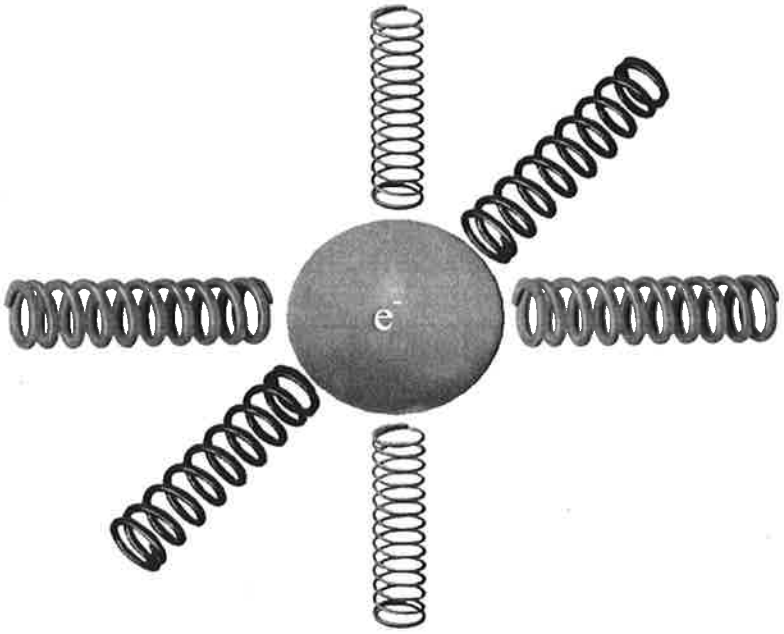

Figure 2.1: Model of the anisotropic binding of an electron in a crystal.

A consequence of the anisotropic binding is that the polarization produced in the crystal by a given field is not just along the direction of the field. Instead, it can vary in a manner that depends on the direction of the applied field with regard to the crystal lattice. Thus, the dependence of P on E is expressible as a tensor relation in the form:

$$\begin{bmatrix} P_x \\ P_y \\ P_z \end{bmatrix} = \varepsilon_o \begin{bmatrix} \chi_{11} & \chi_{12} & \chi_{13} \\ \chi_{21} & \chi_{22} & \chi_{23} \\ \chi_{31} & \chi_{32} & \chi_{33} \end{bmatrix} \begin{bmatrix} E_x \\ E_y \\ E_z \end{bmatrix} \tag{2.19}$$

This is typically abbreviated as:

$$P = \varepsilon_o \chi E \tag{2.20}$$

where χ is the susceptibility tensor:

$$\chi = \begin{bmatrix} \chi_{11} & \chi_{12} & \chi_{13} \\ \chi_{21} & \chi_{22} & \chi_{23} \\ \chi_{31} & \chi_{32} & \chi_{33} \end{bmatrix} \tag{2.21}$$

For ordinary nonabsorbing crystals the χ tensor is symmetric so there always exists a set of coordinate axes, called the principal axes, such that it assumes the diagonal form:

$$\begin{bmatrix} \chi_{11} & 0 & 0 \\ 0 & \chi_{22} & 0 \\ 0 & 0 & \chi_{33} \end{bmatrix} \tag{2.22}$$

The three χs are known as the principal susceptibilities. Given Eq. **(2.18)**, the general wave equation(Eq. **(2.7)**) can be written as follows:

$$\nabla \times (\nabla \times E) + \frac{1}{c^2}\frac{\partial^2 E}{\partial t^2} = -\frac{1}{c^2}\chi\frac{\partial^2 E}{\partial t^2} \tag{2.23}$$

It can then be shown that the crystal can sustain waves of the form $e^{i(k\cdot r - wt)}$ provided the propagation vector k satisfies the equation:

$$k \times (k \times E) + \frac{\omega^2}{c^2}E = -\frac{\omega^2}{c^2}\chi E \tag{2.24}$$

Eq. **(2.24)** can be written out in terms of components as follows:

$$\begin{aligned}
\left(-k_y^2-k_z^2+\frac{\omega^2}{c^2}\right)E_x+k_xk_yE_y+k_xk_zE_z&=-\frac{\omega^2}{c^2}\chi_{11}E_x\\
k_yk_xE_x+\left(-k_x^2-k_z^2+\frac{\omega^2}{c^2}\right)E_y+k_yk_zE_z&=-\frac{\omega^2}{c^2}\chi_{22}E_y\\
k_zk_xE_x+k_zk_yE_y+\left(-k_x^2-k_y^2+\frac{\omega^2}{c^2}\right)E_z&=-\frac{\omega^2}{c^2}\chi_{33}E_z
\end{aligned} \qquad \textbf{(2.25)}$$

In the case where a wave is propagating along the x axis, $k_x = k$, $k_y = k_z = 0$, and the three equations reduce to:

$$\begin{aligned}
\frac{\omega^2}{c^2}E_x&=-\frac{\omega^2}{c^2}\chi_{11}E_x\\
\left(-k^2+\frac{\omega^2}{c^2}\right)E_y&=-\frac{\omega^2}{c^2}\chi_{22}E_y\\
\left(-k^2+\frac{\omega^2}{c^2}\right)E_z&=-\frac{\omega^2}{c^2}\chi_{33}E_z
\end{aligned} \qquad \textbf{(2.26)}$$

The first equation suggests that $E_x = 0$, because neither ω or χ_{11} is zero. This means that the E field is parallel to the x axis. If then $E_y \neq 0$ and $E_z \neq 0$, the second and third equations become:

$$k=\frac{\omega}{c}\sqrt{1+\chi_{22}} \qquad \textbf{(2.27)}$$

and

$$k=\frac{\omega}{c}\sqrt{1+\chi_{33}} \qquad \textbf{(2.28)}$$

Thus, given that ω/k is the phase velocity, there are two possible phase velocities for a wave along the *x*-axis. Using the relation expressed in Eq. **(2.13)**, the refractive index along each propagation direction can then be written as:

$$\begin{aligned} n_1 &= \sqrt{1+\chi_{11}} \\ n_2 &= \sqrt{1+\chi_{22}} \\ n_3 &= \sqrt{1+\chi_{33}} \end{aligned} \qquad \textbf{(2.29)}$$

Thus the speed of propagation of a light wave in a crystal is a function of the direction of the wave's propagation and its polarization.

Birefringent crystals are classified according to the diagonal values of χ. An isotropic crystal has all three diagonal elements identical, and a biaxial crystal has all three elements different. A uniaxial crystal contains two identical diagonal elements (for example, $\chi_{11} = \chi_{22}$), and the corresponding index of refraction of these elements is called the ordinary index n_o and the other index, corresponding to χ_{33}, is called the extraordinary index n_e. If $n_o < n_e$, the crystal is said to be positively birefringent; otherwise the crystal is negatively birefringent. **Table 2.1** gives the parameters for an isotropic and uniaxial crystal.

To understand how the anisotropy of a crystal affects the propagation of optical waves, we can first consider a point light source emanating from the center of a uniaxial crystal. A light wave of arbitrary polarization can always be resolved into two orthogonally polarized waves. Thus, when a spherical wave moves out from a point source, it can be considered to consist of two independent spheres that are

polarized orthogonally and traveling at different phase velocities. Because the indices along two of the directions in the crystal are equal, the nature of the surface for each sphere is such that they touch at a certain point. This point defines the direction in which the velocities of the waves are equal and so defines an "optical" axis of the crystal.

Table 2.1: Susceptibility tensors for isotropic and uniaxial crystals.

Isotropic	$\chi = \begin{bmatrix} a & 0 & 0 \\ 0 & a & 0 \\ 0 & 0 & a \end{bmatrix}$	$\chi_{11} = \chi_{22} = \chi_{33} = a$
Uniaxial	$\chi = \begin{bmatrix} a & 0 & 0 \\ 0 & a & 0 \\ 0 & 0 & b \end{bmatrix}$	$\chi_{11} = \chi_{22} = a, \quad \chi_{33} = b$ $n_o = \sqrt{1+a}$ $n_e = \sqrt{1+b}$

The wave with its polarization perpendicular to the optical axis is termed the ordinary wave (o-wave) with a refractive index n_o. The ordinary wave will encounter equal indices in all directions as it expands, thus the wave front is a true sphere. The wave with its polarization parallel to the optical axis is termed the extraordinary wave (e-wave). The extraordinary wave encounters equal indices along two directions but also an unequal index n_e along the third direction. The resulting wave front forms an ellipse. **Figure 2.2** shows the e-wave's elliptical form and indicates the presence of different velocities along different directions in a negative crystal. The upper- and lower-limit velocities define the long and short axes of the ellipse. The long axis

corresponds to the direction in which the wavefront reaches its greatest velocity through the crystal and is termed the fast-axis. Correspondingly, the short axis is in the direction of the smallest velocity and is termed the slow-axis. The double headed arrows indicate the polarization of the o-wave and the circled x's indicate the polarization of the e-wave. The large arrow heads are pointed along the direction of the optical axis.

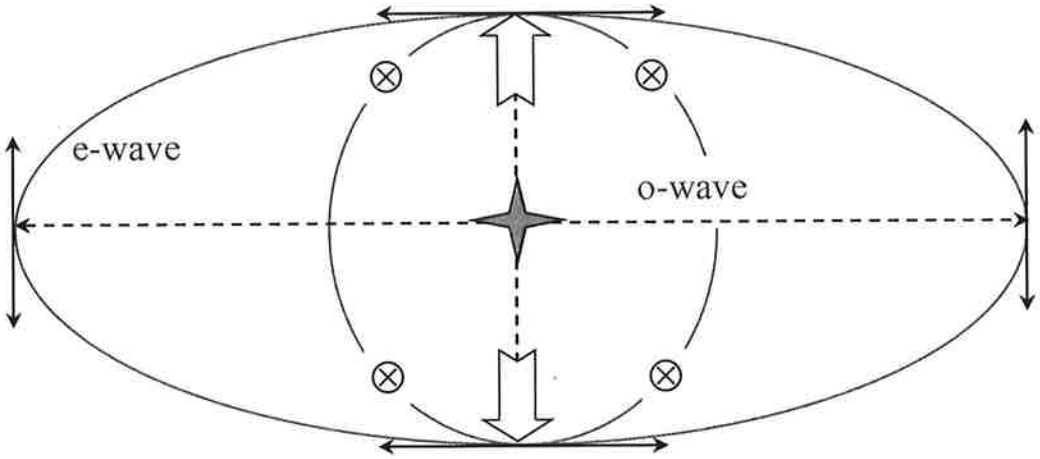

Figure 2.2: Waves expanding from a point source in a positive uniaxial crystal. In this case the o- and e-waves expand at equal velocity along the short axis of the ellipse. If the crystal was negatively birefringent, the spherical o-wave would be outside of the elliptical e-wave and the phase fronts would match along the long axis of the ellipse.

The propagation of a polarized light wave in a uniaxial crystal is thus determined by its two polarization component, the o-wave and the e-wave. They travel at different speeds and will have different phase shifts after traversing a certain distance. The magnitude of birefringence is defined by:

$$\Delta n = n_e - n_o \qquad \textbf{(2.30)}$$

Table 2.2 shows a list of indices of refraction and birefringences for some common substances.

Table 2.2: Refractive indices of some uniaxial birefringent crystals (λ = 589 nm).

Material	n_o	n_e	Δn
Calcite ($CaCO_3$)	1.685	1.486	-0.172
Ice (H_2O)	1.309	1.313	+0.004
Quartz (SiO_2)	1.544	1.554	+0.009
Ruby (Al_2O_2)	1.770	1.762	-0.008
Rutile (TiO_2)	2.616	2.903	+0.287
Sapphire (Al_2O_3)	1.768	1.760	-0.008

If the direction of the optical axis is arranged such that it is perpendicular to the parallel surfaces of a birefringent crystal and the E-field of an incident wave is oriented such that it has components parallel and perpendicular to the optical axis, then they will each propagate through at different speeds **(Figure 2.3)**. After traversing a crystal of thickness d, the resulting wave will have a phase difference δ, defined as:

$$\delta = \frac{2\pi}{\lambda} d(n_e - n_o) \qquad \textbf{(2.31)}$$

where λ is the wavelength of the incident wave. This is the underlying principle of wave plates. A wave plate is an optical component that is designed to induce a predetermined phase shift between the two polarization components of an incident light beam. Wave plates that induce a relative phase shift of $\delta = \pi/2$ are known as

quarter-wave plates; one such device is used in this research and will be addressed in detail later.

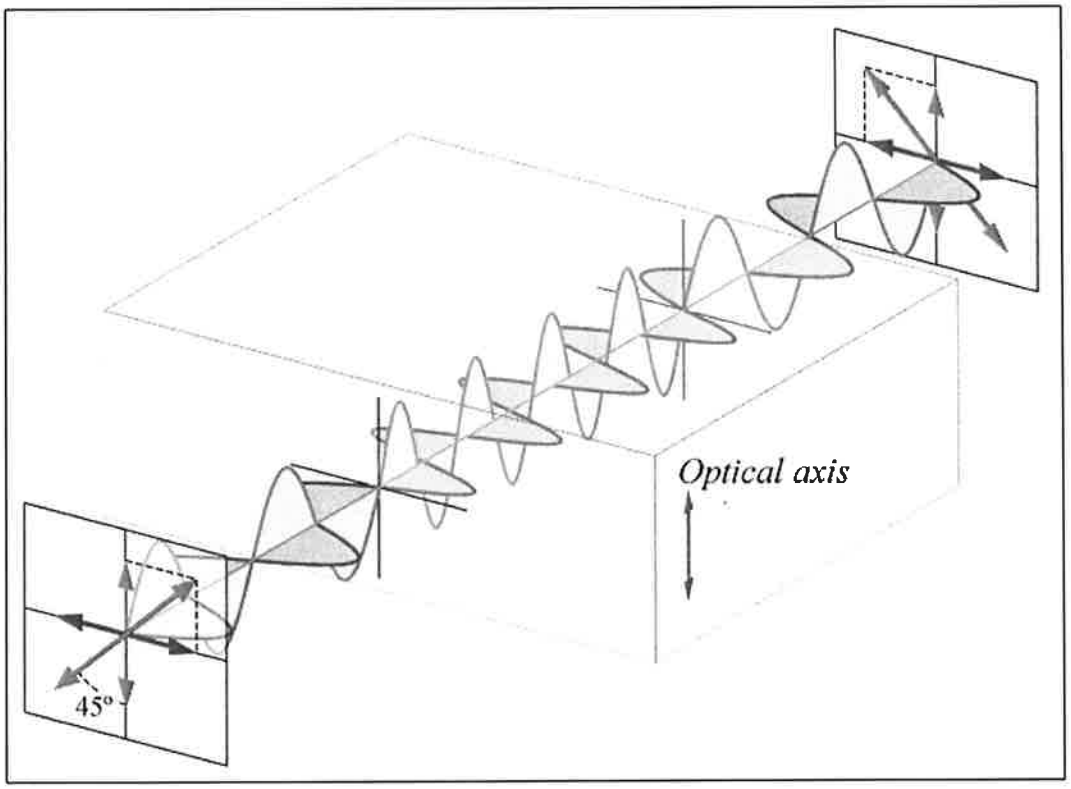

Figure 2.3: Linearly polarized light entering a birefringent crystal. The component of the wave parallel to the crystal's optical axis moves slower than the perpendicular one. The phase shift in the two components results in a new polarization state of the wave at the far side of the crystal.

2.3. Birefringence in Liquids

Birefringence is not limited to crystals and can be expressed in a countless number of pure liquids and solutions as well. John Kerr (1824-1907) was the first to report the electro-optic effect of liquids in 1875. He found that a transparent, isotropic substance would become birefringent when placed in an electric field. The liquid takes on the characteristics of a uniaxial crystal with its optical axis oriented in the direction of the

applied field. The refractive indices associated with the two orientations parallel and perpendicular to the field are represented by $n_{//}$ and $n_{\perp}$ respectively and their difference Δn is given by:

$$\Delta n = \lambda K E^2 \qquad \textbf{(2.32)}$$

where K is the Kerr constant. The field strength E has units of V/m and K has units of m/V^2, leaving Δn unitless. **Table 2.3** lists the Kerr constants for some common liquids.

Table 2.3: Kerr constants for some common liquids ($\lambda = 633$ nm).

Liquid	K (mV^{-2})
Water	3.00×10^{-14}
Nitrobenzene	2.25×10^{-12}
Toluene	8.00×10^{-15}

The electro-optic response of a liquid or solution in an external field is due to orientation or alignment of molecules in the field. Such behavior is the result of the permanent dipole and/or the induced dipole of the molecules. This interaction produces a torque which aligns the symmetry axis of the molecules either parallel or perpendicular to the field (**Figure 2.4**). Once aligned, the bulk solution interacts with polarized light in the same manner as a solid crystal. If the alignment is achieved through the application of an electric field the process is known as Transient Electric Birefringence (TEB). However, particle alignment is also achievable through the application of high intensity optical fields, in which case it's known as the Optical

Kerr Effect (OKE). Alignment through OKE is different from TEB because it relies solely on the particle's polarizability and is completely independent of any dipole moment.

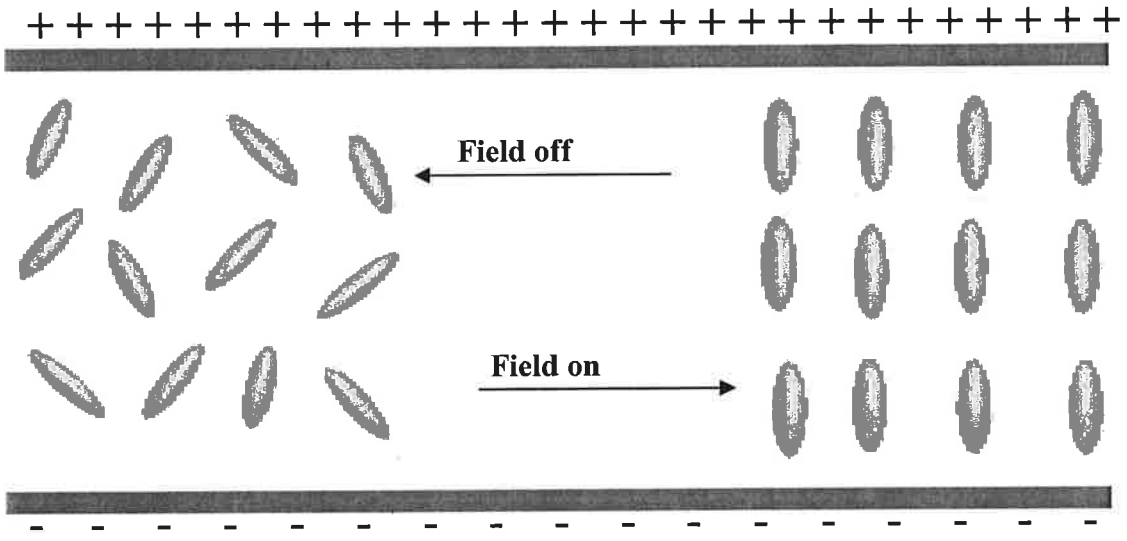

Figure 2.4: General orientation of anisotropic molecules in the absence and presence of an externally applied electric field.

2.4. References

1. Fowles, G.R., *Introduction to Modern Optics*. 2nd ed. 1989, Toronto: General Publishing Company. 328.

2. Propagation of Light

Propagation of an electromagnetic wave through a vacuum or a dielectric material is described using Maxwell's equations. The following section follows the discussion by Fowles and highlights the basic theory behind the interaction of light with anisotropic systems.[1]

2.1. Propagation of Light in an Isotropic Medium

In an isotropic, nonconducting medium, the electrons are bound to the atoms with no preferential direction or orientation. Thus, if the electrons are displaced some distance r from their equilibrium position by a static field E, the resulting polarization of the medium is given by:

$$P = \frac{Ne^2}{K} E \qquad \textbf{(2.1)}$$

where N is the number of electrons, and K is the force constant that equals $-eE/r$. If the field varies with time, the following differential equation of motion results:

$$m\frac{d^2r}{dt^2} + my\frac{dr}{dt} + Kr = -eE \qquad \textbf{(2.2)}$$

where my is a proportionality constant which accounts for the frictional damping force experienced by the electrons. Assuming that the field affecting the electrons varies harmonically as $e^{-i\omega t}$, Eq. **(2.2)** becomes:

$$\left(-m\omega^2 - i\omega my + K\right)r = -eE \tag{2.3}$$

and the polarization represented by **(2.1)** is given by:

$$P = \frac{Ne^2}{-m\omega^2 - i\omega my + K}E \tag{2.4}$$

When $\omega = 0$, Eq. **(2.4)** reduces to the static field scenario represented by Eq. **(2.1)**. A more physically important representation of Eq. **(2.4)** can be established by introducing the resonant frequency ω_o of the bound electrons:

$$P = \frac{Ne^2/m}{\omega_o^2 - \omega^2 + i\omega y}E \tag{2.5}$$

where $$\omega_o = \sqrt{K/m} \tag{2.6}$$

The resonance frequency is intrinsic to the dielectric material and corresponds to the frequency of strong absorption.

The polarization of a non-conducting medium constitutes the source in the general wave equation:

$$\nabla \times \left(\nabla \times E\right) + \frac{1}{c^2}\frac{\partial^2 E}{\partial t^2} = -\mu_o \frac{\partial^2 P}{\partial t^2} \tag{2.7}$$

Substituting Eq. **(2.5)** for the polarization, the right side of Eq. **(2.7)** becomes:

$$\frac{-\mu_o Ne^2}{m}\left(\frac{1}{\omega_o^2 - \omega^2 + -i\omega y}\right)\frac{\partial^2 E}{\partial t^2} \tag{2.8}$$

A general solution to Eq. **(2.7)** is a planar harmonic wave:

$$E = E_o e^{i(Kz-\omega t)} \tag{2.9}$$

with a wave number $\mathcal{K}$ expressed as:

$$K^2 = \frac{\omega^2}{c^2}\left(1+\frac{Ne^2}{m\varepsilon_o}\cdot\frac{1}{\omega_o^2-\omega^2-iy\omega}\right) \tag{2.10}$$

The real and complex parts of $\mathcal{K}$ can be represented as:

$$K = k + i\alpha \tag{2.11}$$

By substituting the right side of Eq. **(2.11)** into the plane wave expressed by Eq. **(2.9)**, the general solution can now be re-written as:

$$E = E_o e^{\alpha z} e^{i(kz-\omega t)} \tag{2.12}$$

The factor $e^{-\alpha z}$ indicates that the amplitude decreases exponentially with distance. Thus, as the wave moves through the medium, its energy is absorbed. Given that the energy is proportional to $|E|^2$, 2α is termed the coefficient of absorption of the medium. The phase factor $e^{i(kz-\omega t)}$ indicates that the phase velocity v is:

$$v = \frac{\omega}{k} = \frac{c}{n} \tag{2.13}$$

Eq. **(2.13)** represents the relation between the refractive index n, the wave vector k, and the speed of light c. The refractive index $\mathcal{N}$ is defined as the ratio of the speed of

light in vacuum to its speed in a medium ($n = c/v$), and it can be expressed in a similar fashion to the complex wave vector $\mathscr{K}$ where:

$$N = n + i\kappa \tag{2.14}$$

and that:

$$K = \frac{\omega}{c} N \tag{2.15}$$

Thus the imaginary portion of the complex index of refraction $\mathscr{N}$ is termed the extinction coefficient κ and is related to α. From Eq. **(2.10)** and Eq. **(2.15)**, we can obtain:

$$n = 1 + \frac{Ne^2}{2m\varepsilon_o}\left(\frac{\omega_o^2 - \omega^2}{(\omega_o^2 - \omega^2)^2 + y^2\omega^2}\right) \tag{2.16}$$

$$\kappa = \frac{Ne^2\omega}{2m\varepsilon_o}\left(\frac{y^2\omega^2}{(\omega_o^2 - \omega^2)^2 + y^2\omega^2}\right) \tag{2.17}$$

Finally, if the frictional damping constant is sufficiently small, the term $y^2\omega^2$ can be neglected and Eq. **(2.16)** simplifies to:

$$n = 1 + \frac{Ne^2}{8\pi^2 m\varepsilon_o}\left(\frac{1}{\nu_o^2 - \nu^2}\right) \tag{2.18}$$

where the denominator has been multiplied by $4\pi^2$ in changing from angular frequency to normal frequency.

2.2. Propagation of Light in an Anisotropic Medium

Many crystalline substances in nature are optically anisotropic. If a crystal's lattice is not completely symmetric then the binding forces on the electrons are not equal in all directions. A crystal which displays anisotropy in the electronic binding force is termed birefringent. Birefringent crystals belonging to the hexagonal, tetragonal, and trigonal groups are termed "uniaxial," having their atoms arranged in such a way that there is a single optical axis which corresponds to a direction about which the atoms are arranged symmetrically. There also exist biaxial crystals, having two optical axes and three refractive indices. Although interesting, the discussion of biaxial crystals will be avoided, as they have little relevance to the current study. Cubic crystals like sodium chloride display no birefringence, owing to their relatively simple and highly symmetric structure. Their lattice contains four 3-fold symmetry axes so light emanating from a point source within the structure will propagate uniformly in all directions. Such a material will have a single index of refraction and be optically isotropic.

An illustration of the anisotropic polarizability of a crystal is shown in **Figure 2.1**, where an electron is pictured as being attached to fictitious springs. The springs are of varying stiffness as they extend in different directions, representing the varying forces exerted on the electron as it is displaced from its equilibrium position.

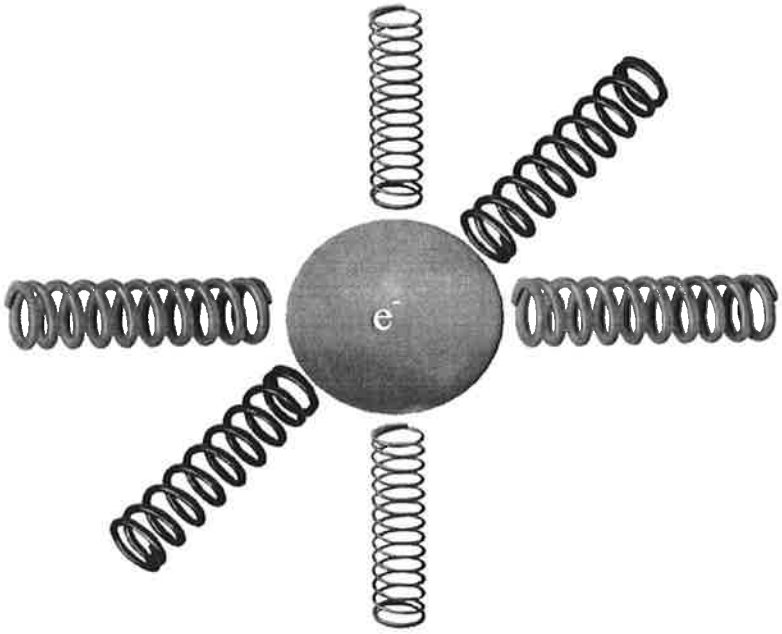

Figure 2.1: Model of the anisotropic binding of an electron in a crystal.

A consequence of the anisotropic binding is that the polarization produced in the crystal by a given field is not just along the direction of the field. Instead, it can vary in a manner that depends on the direction of the applied field with regard to the crystal lattice. Thus, the dependence of P on E is expressible as a tensor relation in the form:

$$\begin{bmatrix} P_x \\ P_y \\ P_z \end{bmatrix} = \varepsilon_o \begin{bmatrix} \chi_{11} & \chi_{12} & \chi_{13} \\ \chi_{21} & \chi_{22} & \chi_{23} \\ \chi_{31} & \chi_{32} & \chi_{33} \end{bmatrix} \begin{bmatrix} E_x \\ E_y \\ E_z \end{bmatrix} \tag{2.19}$$

This is typically abbreviated as:

$$P = \varepsilon_o \chi E \tag{2.20}$$

where χ is the susceptibility tensor:

$$\chi = \begin{bmatrix} \chi_{11} & \chi_{12} & \chi_{13} \\ \chi_{21} & \chi_{22} & \chi_{23} \\ \chi_{31} & \chi_{32} & \chi_{33} \end{bmatrix} \tag{2.21}$$

For ordinary nonabsorbing crystals the χ tensor is symmetric so there always exists a set of coordinate axes, called the principal axes, such that it assumes the diagonal form:

$$\begin{bmatrix} \chi_{11} & 0 & 0 \\ 0 & \chi_{22} & 0 \\ 0 & 0 & \chi_{33} \end{bmatrix} \tag{2.22}$$

The three χs are known as the principal susceptibilities. Given Eq. **(2.18)**, the general wave equation(Eq. **(2.7)**) can be written as follows:

$$\nabla \times (\nabla \times E) + \frac{1}{c^2}\frac{\partial^2 E}{\partial t^2} = -\frac{1}{c^2}\chi\frac{\partial^2 E}{\partial t^2} \tag{2.23}$$

It can then be shown that the crystal can sustain waves of the form $e^{i(k\cdot r - wt)}$ provided the propagation vector k satisfies the equation:

$$k \times (k \times E) + \frac{\omega^2}{c^2}E = -\frac{\omega^2}{c^2}\chi E \tag{2.24}$$

Eq. **(2.24)** can be written out in terms of components as follows:

$$\begin{aligned}
\left(-k_y^2-k_z^2+\frac{\omega^2}{c^2}\right)E_x+k_xk_yE_y+k_xk_zE_z&=-\frac{\omega^2}{c^2}\chi_{11}E_x\\
k_yk_xE_x+\left(-k_x^2-k_z^2+\frac{\omega^2}{c^2}\right)E_y+k_yk_zE_z&=-\frac{\omega^2}{c^2}\chi_{22}E_y\\
k_zk_xE_x+k_zk_yE_y+\left(-k_x^2-k_y^2+\frac{\omega^2}{c^2}\right)E_z&=-\frac{\omega^2}{c^2}\chi_{33}E_z
\end{aligned}\qquad \textbf{(2.25)}$$

In the case where a wave is propagating along the x axis, $k_x = k$, $k_y = k_z = 0$, and the three equations reduce to:

$$\begin{aligned}
\frac{\omega^2}{c^2}E_x&=-\frac{\omega^2}{c^2}\chi_{11}E_x\\
\left(-k^2+\frac{\omega^2}{c^2}\right)E_y&=-\frac{\omega^2}{c^2}\chi_{22}E_y\\
\left(-k^2+\frac{\omega^2}{c^2}\right)E_z&=-\frac{\omega^2}{c^2}\chi_{33}E_z
\end{aligned}\qquad \textbf{(2.26)}$$

The first equation suggests that $E_x = 0$, because neither ω or χ_{11} is zero. This means that the E field is parallel to the x axis. If then $E_y \neq 0$ and $E_z \neq 0$, the second and third equations become:

$$k=\frac{\omega}{c}\sqrt{1+\chi_{22}} \qquad \textbf{(2.27)}$$

and

$$k=\frac{\omega}{c}\sqrt{1+\chi_{33}} \qquad \textbf{(2.28)}$$

Thus, given that ω/k is the phase velocity, there are two possible phase velocities for a wave along the x-axis. Using the relation expressed in Eq. **(2.13)**, the refractive index along each propagation direction can then be written as:

$$\begin{aligned} n_1 &= \sqrt{1+\chi_{11}} \\ n_2 &= \sqrt{1+\chi_{22}} \\ n_3 &= \sqrt{1+\chi_{33}} \end{aligned} \qquad \textbf{(2.29)}$$

Thus the speed of propagation of a light wave in a crystal is a function of the direction of the wave's propagation and its polarization.

Birefringent crystals are classified according to the diagonal values of χ. An isotropic crystal has all three diagonal elements identical, and a biaxial crystal has all three elements different. A uniaxial crystal contains two identical diagonal elements (for example, $\chi_{11} = \chi_{22}$), and the corresponding index of refraction of these elements is called the ordinary index n_o and the other index, corresponding to χ_{33}, is called the extraordinary index n_e. If $n_o < n_e$, the crystal is said to be positively birefringent; otherwise the crystal is negatively birefringent. **Table 2.1** gives the parameters for an isotropic and uniaxial crystal.

To understand how the anisotropy of a crystal affects the propagation of optical waves, we can first consider a point light source emanating from the center of a uniaxial crystal. A light wave of arbitrary polarization can always be resolved into two orthogonally polarized waves. Thus, when a spherical wave moves out from a point source, it can be considered to consist of two independent spheres that are

polarized orthogonally and traveling at different phase velocities. Because the indices along two of the directions in the crystal are equal, the nature of the surface for each sphere is such that they touch at a certain point. This point defines the direction in which the velocities of the waves are equal and so defines an "optical" axis of the crystal.

Table 2.1: Susceptibility tensors for isotropic and uniaxial crystals.

Isotropic	$\chi = \begin{bmatrix} a & 0 & 0 \\ 0 & a & 0 \\ 0 & 0 & a \end{bmatrix}$	$\chi_{11} = \chi_{22} = \chi_{33} = a$
Uniaxial	$\chi = \begin{bmatrix} a & 0 & 0 \\ 0 & a & 0 \\ 0 & 0 & b \end{bmatrix}$	$\chi_{11} = \chi_{22} = a, \quad \chi_{33} = b$ $n_o = \sqrt{1+a}$ $n_e = \sqrt{1+b}$

The wave with its polarization perpendicular to the optical axis is termed the ordinary wave (o-wave) with a refractive index n_o. The ordinary wave will encounter equal indices in all directions as it expands, thus the wave front is a true sphere. The wave with its polarization parallel to the optical axis is termed the extraordinary wave (e-wave). The extraordinary wave encounters equal indices along two directions but also an unequal index n_e along the third direction. The resulting wave front forms an ellipse. **Figure 2.2** shows the e-wave's elliptical form and indicates the presence of different velocities along different directions in a negative crystal. The upper- and lower-limit velocities define the long and short axes of the ellipse. The long axis

corresponds to the direction in which the wavefront reaches its greatest velocity through the crystal and is termed the fast-axis. Correspondingly, the short axis is in the direction of the smallest velocity and is termed the slow-axis. The double headed arrows indicate the polarization of the o-wave and the circled x's indicate the polarization of the e-wave. The large arrow heads are pointed along the direction of the optical axis.

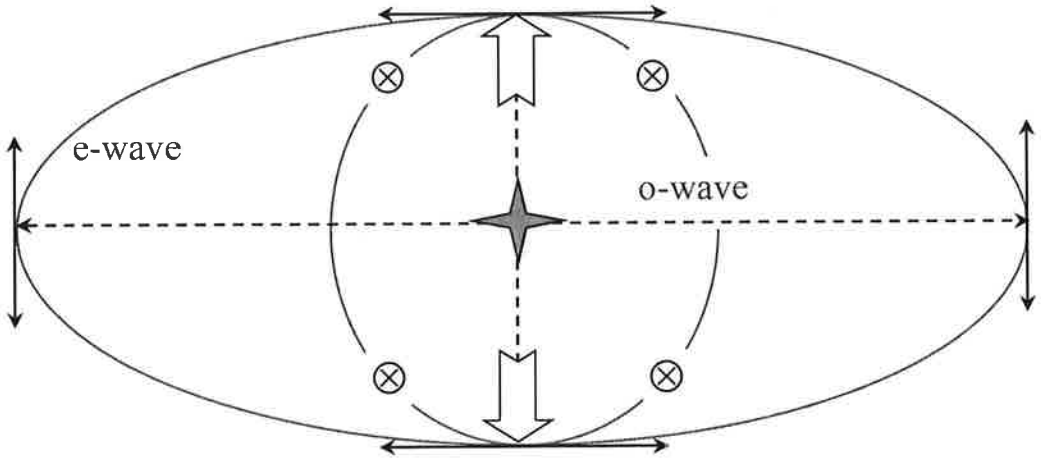

Figure 2.2: Waves expanding from a point source in a positive uniaxial crystal. In this case the o- and e-waves expand at equal velocity along the short axis of the ellipse. If the crystal was negatively birefringent, the spherical o-wave would be outside of the elliptical e-wave and the phase fronts would match along the long axis of the ellipse.

The propagation of a polarized light wave in a uniaxial crystal is thus determined by its two polarization component, the o-wave and the e-wave. They travel at different speeds and will have different phase shifts after traversing a certain distance. The magnitude of birefringence is defined by:

$$\Delta n = n_e - n_o \qquad \textbf{(2.30)}$$

Table 2.2 shows a list of indices of refraction and birefringences for some common substances.

Table 2.2: Refractive indices of some uniaxial birefringent crystals (λ = 589 nm).

Material	n_o	n_e	Δn
Calcite ($CaCO_3$)	1.685	1.486	-0.172
Ice (H_2O)	1.309	1.313	+0.004
Quartz (SiO_2)	1.544	1.554	+0.009
Ruby (Al_2O_2)	1.770	1.762	-0.008
Rutile (TiO_2)	2.616	2.903	+0.287
Sapphire (Al_2O_3)	1.768	1.760	-0.008

If the direction of the optical axis is arranged such that it is perpendicular to the parallel surfaces of a birefringent crystal and the E-field of an incident wave is oriented such that it has components parallel and perpendicular to the optical axis, then they will each propagate through at different speeds **(Figure 2.3)**. After traversing a crystal of thickness d, the resulting wave will have a phase difference δ, defined as:

$$\delta = \frac{2\pi}{\lambda} d(n_e - n_o) \qquad \textbf{(2.31)}$$

where λ is the wavelength of the incident wave. This is the underlying principle of wave plates. A wave plate is an optical component that is designed to induce a predetermined phase shift between the two polarization components of an incident light beam. Wave plates that induce a relative phase shift of $\delta = \pi/2$ are known as

quarter-wave plates; one such device is used in this research and will be addressed in detail later.

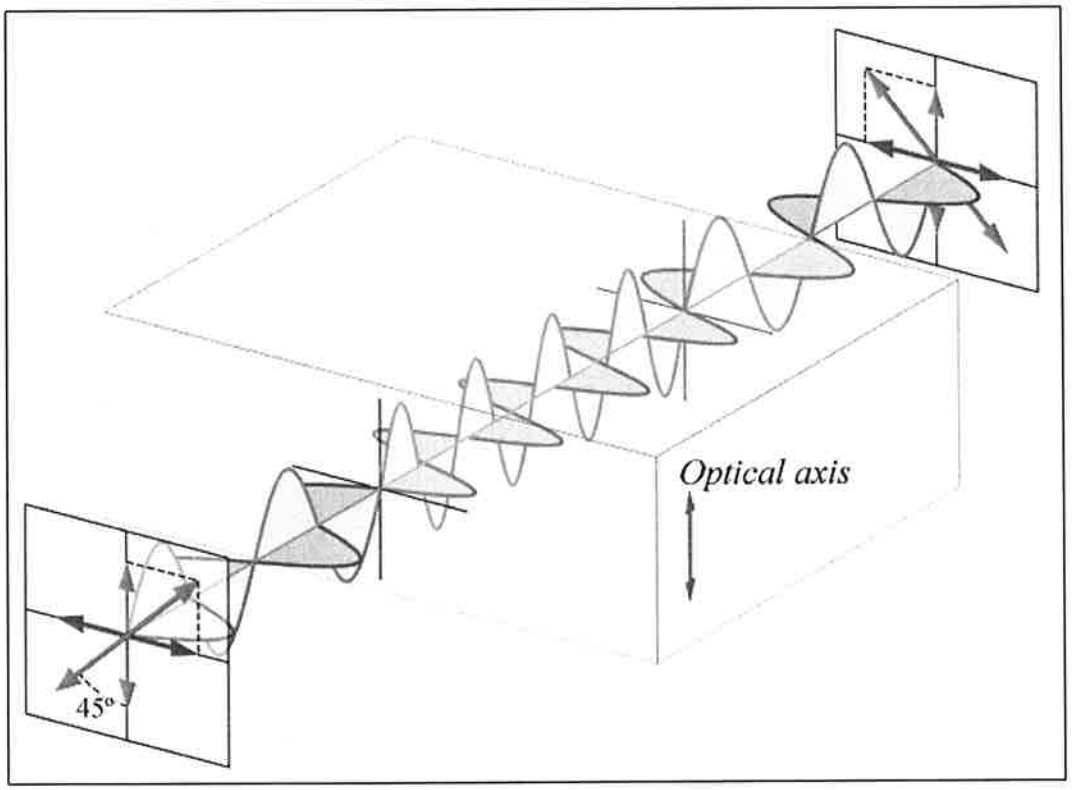

Figure 2.3: Linearly polarized light entering a birefringent crystal. The component of the wave parallel to the crystal's optical axis moves slower than the perpendicular one. The phase shift in the two components results in a new polarization state of the wave at the far side of the crystal.

2.3. Birefringence in Liquids

Birefringence is not limited to crystals and can be expressed in a countless number of pure liquids and solutions as well. John Kerr (1824-1907) was the first to report the electro-optic effect of liquids in 1875. He found that a transparent, isotropic substance would become birefringent when placed in an electric field. The liquid takes on the characteristics of a uniaxial crystal with its optical axis oriented in the direction of the

applied field. The refractive indices associated with the two orientations parallel and perpendicular to the field are represented by $n_{//}$ and $n_{\perp}$ respectively and their difference Δn is given by:

$$\Delta n = \lambda K E^2 \qquad \textbf{(2.32)}$$

where K is the Kerr constant. The field strength E has units of V/m and K has units of m/V^2, leaving Δn unitless. **Table 2.3** lists the Kerr constants for some common liquids.

Table 2.3: Kerr constants for some common liquids (λ = 633 nm).

Liquid	**K (mV^{-2})**
Water	3.00×10^{-14}
Nitrobenzene	2.25×10^{-12}
Toluene	8.00×10^{-15}

The electro-optic response of a liquid or solution in an external field is due to orientation or alignment of molecules in the field. Such behavior is the result of the permanent dipole and/or the induced dipole of the molecules. This interaction produces a torque which aligns the symmetry axis of the molecules either parallel or perpendicular to the field (**Figure 2.4**). Once aligned, the bulk solution interacts with polarized light in the same manner as a solid crystal. If the alignment is achieved through the application of an electric field the process is known as Transient Electric Birefringence (TEB). However, particle alignment is also achievable through the application of high intensity optical fields, in which case it's known as the Optical

Kerr Effect (OKE). Alignment through OKE is different from TEB because it relies solely on the particle's polarizability and is completely independent of any dipole moment.

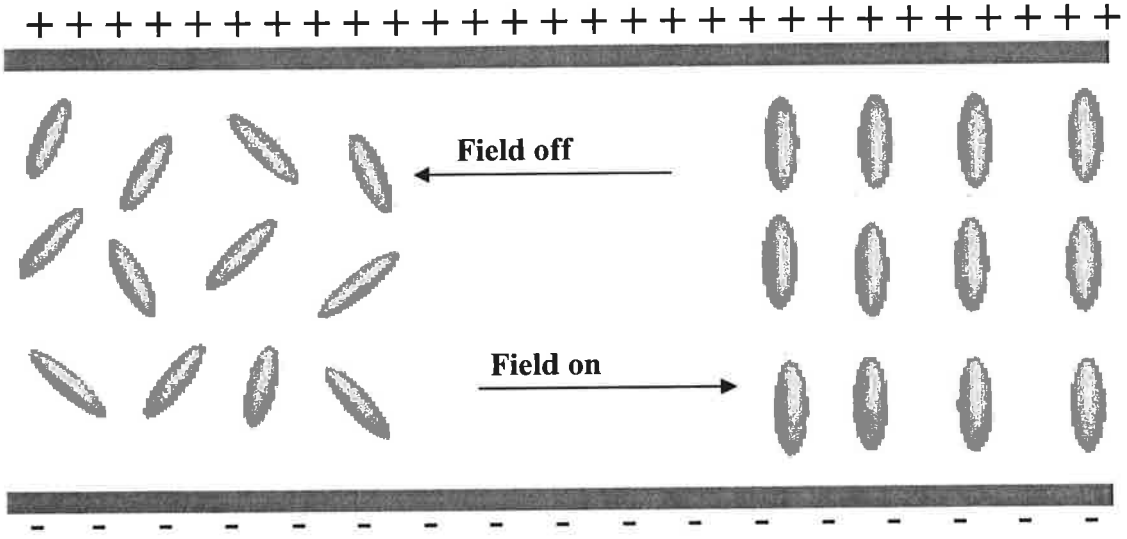

Figure 2.4: General orientation of anisotropic molecules in the absence and presence of an externally applied electric field.

2.4. References

1. Fowles, G.R., *Introduction to Modern Optics*. 2nd ed. 1989, Toronto: General Publishing Company. 328.

3. Transient Electric Birefringence (TEB)

3.1 Introduction

Transient electric-field induced birefringence is a method that has been used extensively to study the rotational diffusion, size, shape, and polarization properties of objects with anisotropic geometries.[1-10] In general, TEB measurements require a polarized probe beam and polarization analysis optics. The experimental setup **(Figure 3.1)** contains an initial polarizer ***P1*** which defines the probe beam's polarization axis. An electric field is applied in a sample cell by two electrodes at 45° to the polarization axis of the probe beam. An analyzing polarizer ***P2*** oriented 90° from the initial polarizer is placed downstream from the sample cell ***C*** and before the detector. A quarter-wave plate ***λ/4*** is sometimes inserted between the cell and the analyzer and is generally oriented with its fast-axis parallel to the initial polarizer. Typical experiments on dilute media use optical cells a few centimeters in length, visible laser light, and are capable of measuring birefringence Δn on the order of 10^{-9} to 10^{-10}, correlating to phase shifts δ in the range of 10^{-1} to 10^{-2} radians.

3.2. The Detection Scheme

Figure 3.2 shows the relevant axes in a standard TEB experiment. The polarization direction E_y of the HeNe beam is oriented 45° to that of the alignment direction of the external field. Hence the probe beam has two orthogonal components, one parallel to the alignment field $E_{//}$ and the other perpendicular to it $E_{\perp}$. As the beam passes through the sample cell its two components interact differently with the molecules

aligned in the field. The result is a phase shift between the HeNe beam's two components and its subsequent change from linear to elliptically polarized light.

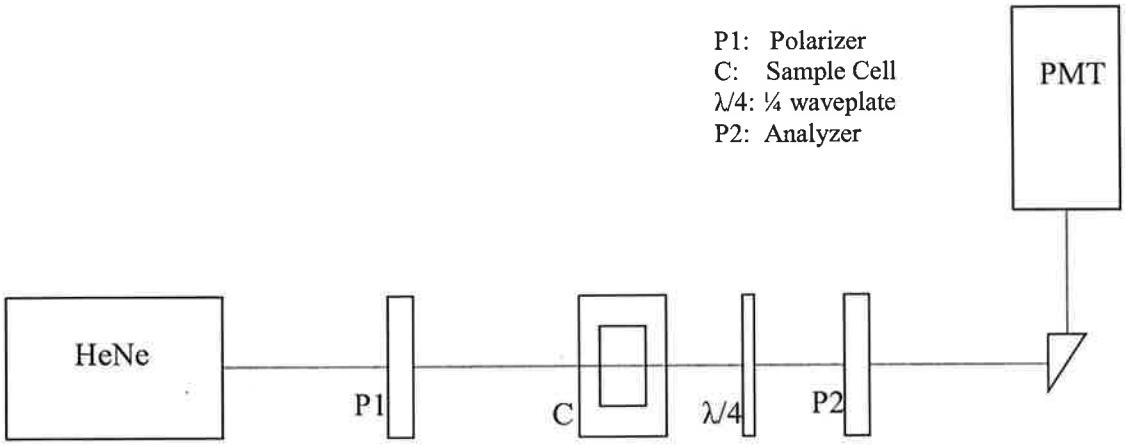

Figure 3.1: Standard TEB setup using the minimal number of optics. Addition of pinholes and filters is also common to aid in improving the signal to noise ratio.

An analyzer is placed downstream from the sample cell and oriented such that it measures the component of the probe beam perpendicular to its incident polarization direction. In the absence of any induced birefringence all of the probe beam's intensity is directed along its incident polarization direction E_y leaving the measured intensity along the E_x direction equal to zero. However, once an external field is applied and birefingence is introduced into the system, the result is a measureable intensity along E_x.

Adjustment of the optics is made as follows. With the probe beam, polarizer **P1,** and PMT positioned, the analyzing prism **P2** is introduced with its optical axis

perpendicular to that of the polarizer **P1** at 45° with respect to the alignment field. The angle of the analyzer **P2** is then adjusted to a truly "crossed" position by following a DC signal of the HeNe on an oscilloscope and rotating the analyzer until the signal is minimized. An optional quarter-wave plate **λ/4** can then be placed between the sample cell **C** and analyzer **P2**, with its fast-axis parallel to that of the polarizer direction **P1**. Its orientation is checked in the same manner as that of the analyzer **P2**; i.e., it is rotated until a DC signal of the HeNe on the oscilloscope is minimized.

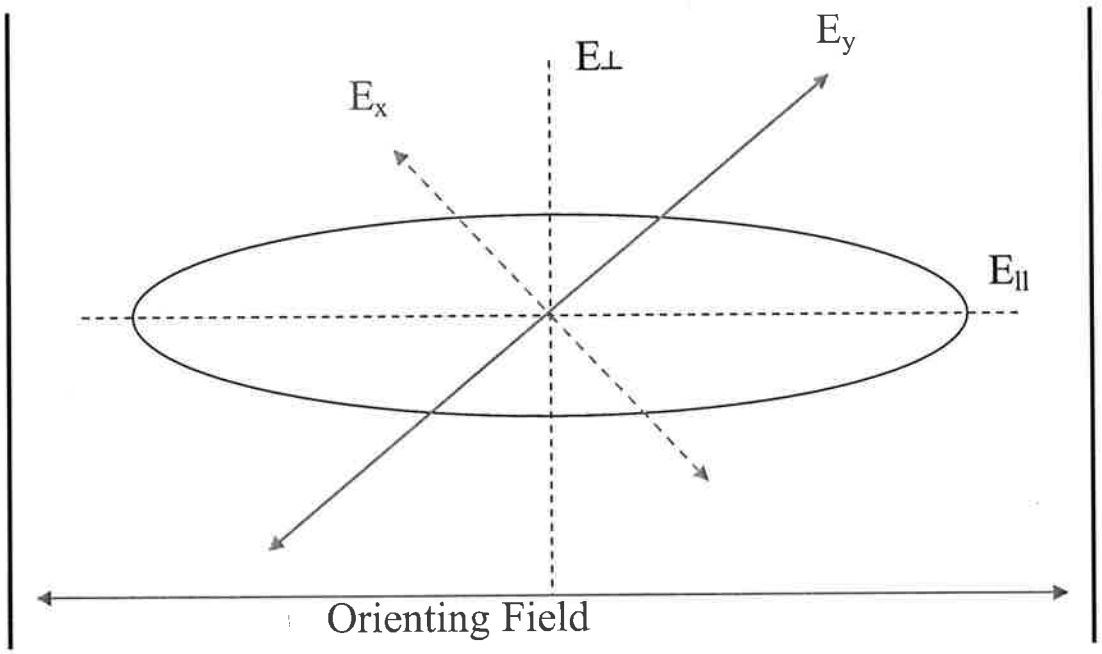

Figure 3.2: Field orientations in the sample cell. The linearly polarized probe beam has components parallel and perpendicular to the alignment field.

If one wishes to know the sign of the birefringence induced in a sample, an offset analyzer angle in combination with a quarter-wave plate can be introduced in the setup. In this case, the analyzer **P2** is rotated through an angle α from the crossed

position towards the direction of the alignment field. The light signal in the absence of an alignment field and its change in the presence of an alignment field can now be recorded. In the following, variations on the outlined scheme that aid in detection and optimization of the birefringent signal will be discussed.

3.3. Fundamental Equations

The following treatment derives the phase shift δ of a polarized probe beam after passing through a birefringent sample. It starts by separating the probe beam into two orthogonal components and showing how they are affected by the difference in refractive index Δn along each axis. The two components are then brought back together along the analyzer direction. With one component of the probe beam directed parallel to the alignment field and the other perpendicular to it, we get:

$$\vec{E}_{probe} = \vec{E}_{ll} + \vec{E}_{\perp} \tag{3.1}$$

where $$\vec{E}_{ll} = \vec{E}_{\perp} = \frac{1}{\sqrt{2}} \varepsilon_o e^{i(\vec{k}\hat{z} - \omega t)} \tag{3.2}$$

After passing through the sample, the orthogonal components of the HeNe undergo a phase shift, exiting as:

$$\vec{E}_{ll} = \frac{1}{\sqrt{2}} \varepsilon_o e^{ik_{ll}d} e^{i(k\hat{z} - \omega t)} \tag{3.3}$$

$$\vec{E}_{\perp} = \frac{1}{\sqrt{2}} \varepsilon_o e^{ik_{\perp}d} e^{i(k\hat{z} - \omega t)} \tag{3.4}$$

where d is the distance the beam travels in the sample cell, $k_{ll} = (2\pi/\lambda)n_{ll}$, and $k_{\perp} = (2\pi/\lambda)n_{\perp}$. Because the birefringent signal is a function of the difference between the two exiting waves, it is now convenient to disregard the common time dependent term. Rewriting with respect to $k_{\perp}$ gives:

$$\vec{E}_{ll} = \frac{1}{\sqrt{2}}\varepsilon_o e^{i\delta} e^{ik_{\perp}d} \tag{3.5}$$

$$\vec{E}_{\perp} = \frac{1}{\sqrt{2}}\varepsilon_o e^{ik_{\perp}d} \tag{3.6}$$

where $\delta = (k_{ll} - k_{\perp})d = (2\pi d/\lambda)\Delta n$ and $\Delta n = n_{ll} - n_{\perp}$. The projection of the probe beam along E_y and E_x can then be written:

$$\vec{E}_y = \frac{1}{\sqrt{2}}\vec{E}_{ll} + \frac{1}{\sqrt{2}}\vec{E}_{\perp} \tag{3.7}$$

$$\vec{E}_x = \frac{1}{\sqrt{2}}\vec{E}_{ll} - \frac{1}{\sqrt{2}}\vec{E}_{\perp} \tag{3.8}$$

Expanding the expressions with respect to Eq. **(3.5)** and Eq. **(3.6)** gives:

$$\vec{E}_y = \frac{1}{\sqrt{2}}\left[\frac{1}{\sqrt{2}}\varepsilon_o e^{i\delta} e^{ik_{\perp}d} + \frac{1}{\sqrt{2}}\varepsilon_o e^{ik_{\perp}d}\right] \tag{3.9}$$

$$\vec{E}_x = \frac{1}{\sqrt{2}}\left[\frac{1}{\sqrt{2}}\varepsilon_o e^{i\delta} e^{ik_{\perp}d} - \frac{1}{\sqrt{2}}\varepsilon_o e^{ik_{\perp}d}\right] \tag{3.10}$$

Rearrangement then yields:

$$\vec{E}_y = \frac{1}{2}\varepsilon_o e^{ik_\perp d}\left(e^{i\delta} + 1\right) \tag{3.11}$$

$$\vec{E}_x = \frac{1}{2}\varepsilon_o e^{ik_\perp d}\left(e^{i\delta} - 1\right) \tag{3.12}$$

Expanding E_y with respect to $e^{i\delta}$ and rewriting using its trigonometric identity gives:

$$\vec{E}_y = \frac{1}{2}\varepsilon_o e^{ik_\perp d} e^{i(\delta/2)}\left[e^{i(\delta/2)} + e^{-i(\delta/2)}\right] \tag{3.13}$$

$$= \varepsilon_o e^{i(\delta/2 + k_\perp d)}\cos\left(\delta/2\right) \tag{3.14}$$

Following the same reasoning for E_x:

$$\vec{E}_x = i\varepsilon_o e^{i(\delta/2 + k_\perp d)}\sin\left(\delta/2\right) \tag{3.15}$$

Finally, taking the square modulus of E, the expressions for the measured intensities of the probe beam I_o along each axis have the forms:

$$I_y = I_o \cos^2\left(\delta/2\right) \tag{3.16}$$

$$I_x = I_o \sin^2\left(\delta/2\right) \tag{3.17}$$

For small δ, the expression for I_x along the direction of the analyzer can be reduced as follows:

$$I = I_o\left[\frac{\delta^2}{4}\right] \quad or \quad \delta = 2\left[\frac{I}{I_o}\right]^{1/2} \tag{3.18}$$

Thus, a reasonable estimate of the phase difference δ can be determined by first measuring I_o and then I. The primary benefit to this quadratic approximation is amplification of the signal due to its dependence on the square of δ. However, because the signal response is quadratic, it fails to give the sign of the birefringence. Furthermore, the measurement of two hugely different intensities can be problematic because the dynamic range of any detection system is limited. To maintain the linear range of the PMT, multiple filters are typically used, which introduces new concerns as the reflective losses on the filters are tedious to keep track of. A better method would be one in which a single optical adjustment can be made and no additional optics are required in order to measure I_o.

3.3.1. Use of an Analyzer Offset Angle α

An improved method of measurement is to rotate the analyzer by a small angle and, in so doing, solving the problem of detector saturation when recording the incident beam. **Figure 3.3** shows the two waves expressed by Eq. **(3.14)** and Eq. **(3.15)** and their projections along E_x' and E_y' at angle α. By adding the waves and taking their square modulus as done previously we get:

$$\begin{aligned} I_{y'} &= E_y^2 \cos^2\alpha + E_x^2 \sin^2\alpha \\ &= I_o\left[\cos^2(\delta/2)\cos^2\alpha + \sin^2(\delta/2)\sin^2\alpha\right] \end{aligned} \tag{3.19}$$

$$\begin{aligned} I_{x'} &= E_y^2 \sin^2\alpha + E_x^2 \cos^2\alpha \\ &= I_o\left[\cos^2(\delta/2)\sin^2\alpha + \sin^2(\delta/2)\cos^2\alpha\right] \end{aligned} \tag{3.20}$$

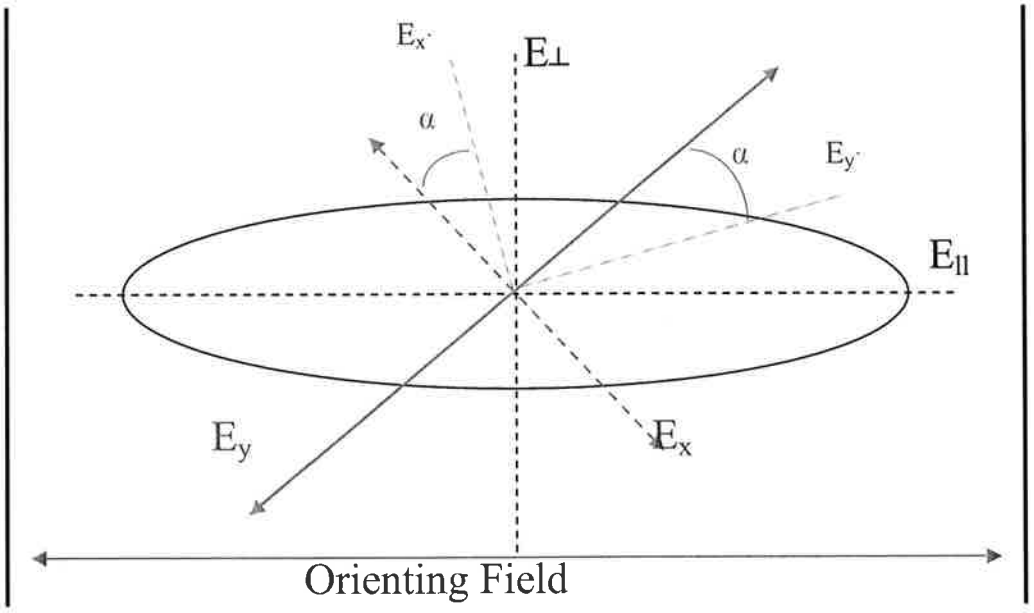

Figure 3.3: Field orientations with a non-zero offset analyzer angle α.

The reader is reminded that E_x is purely imaginary in Eq. **(3.15)**; thereby eliminating the interference term that would otherwise be present in Eq. **(3.19)** and Eq. **(3.20)**. Using the trigonometric relations $\sin^2\theta = \frac{1-\cos 2\theta}{2}$ and $\cos^2\theta = \frac{1+\cos 2\theta}{2}$, Eq. **(3.19)** and Eq. **(3.20)** become:

$$I_{y'} = \frac{I_o}{2}(1+\cos 2\alpha \cos\delta) \qquad \textbf{(3.21)}$$

$$I_{x'} = I_\delta = \frac{I_o}{2}(1-\cos 2\alpha \cos\delta) \qquad \textbf{(3.22)}$$

Where $I_{x'} = I_\delta$ represents the birefringent intensity when the analyzer is offset by an angle α. If there is no net sample alignment then Eq. **(3.22)** reduces to:

$$I_\alpha = \frac{I_o}{2}(1-\cos 2\alpha) = I_o \sin^2 \alpha \qquad \textbf{(3.23)}$$

where the symbol I_α is essentially the background at an analyzer angle α without any birefringence from the sample. The change of the light intensity due to sample birefringence is thus given by:

$$\Delta I_\delta = I_\delta - I_\alpha = \frac{I_o}{2}(1-\cos\delta)\cos 2\alpha \qquad \textbf{(3.24)}$$

$$= I_o \sin^2(\delta/2)\cos 2\alpha \qquad \textbf{(3.25)}$$

Eq. **(3.25)** indicates that the maximum signal is observed when α = 0, i. e., the background free condition without the offset angle α shown in Figure 3.3 is the most sensitive at low levels of birefringence. The introduction of an analyzer offset angle α knowingly introduces a background, and this background serves as a representation of the intensity of the incident beam. Two steps of measurements are typically required to take advantage of this approach. The first is to set the analyzer angle $\alpha = 0$ in order to obtain the birefringent signal I_δ and then, without the alignment field, rotate the analyzer to a known angle α for the measurement of I_α. The ratio of the two intensities is then:

$$\frac{I_\delta}{I_\alpha} = \frac{\sin^2(\delta/2)}{\sin^2\alpha} \qquad \textbf{(3.26)}$$

thus,
$$\delta = 2\alpha \sin^{-1}\left[\frac{I_\delta}{I_\alpha}\right]^{1/2} \qquad \textbf{(3.27)}$$

Of course it is also possible to take measurements of the background together with the birefringent signal, i.e., to obtain ΔI_δ and I_α. This approach eliminates the need of rotating the polarizer during the experiment. However, the mathematical relation of the resulting intensities is somewhat cumbersome, and the sensitivity suffers as well.

The greatest benefit of Eq. **(3.27)** is the replacement of I_o with I_α. This means that the measurement of the incident beam I_o is no longer necessary; rather one should measure the intensity transmitted by the analyzer I_α at a small angle α in the absence of any induced birefringence. This procedure does have two disadvantages however. The first is that the analyzer angle α must be known precisely, and the second is that the optics need to be rotated during the measurement. Both issues affect the precision and reproducibility of the experimental results.

3.3.2. Use of a Quarter-Wave Plate

The presence of a quarter-wave plate between the sample and analyzer will enable the distinction between positive and negative birefringence values, in addition to increasing the sensitivity of the measurement. With the fast-axis of the wave plate directed along E_y and the analyzer angle set to zero, the fields along each direction are represented by Eq. **(3.14)** and Eq. **(3.15)**. With the reintroduction of the complex term to account for the interaction of the waves with the different axes of the wave-plate we have:

$$E_y = \varepsilon_o \cos(\delta/2) e^{i(kz-\omega t)} \qquad \textbf{(3.28)}$$

$$\begin{aligned} E_x &= i\varepsilon_o \sin(\delta/2) e^{i(kz-\omega t)} e^{-i\pi/2} \\ &= \varepsilon_o \sin(\delta/2) e^{i(kz-\omega t)} \end{aligned} \tag{3.29}$$

Leaving the probe beam linearly polarized at an angle θ given by:

$$\tan\theta = \frac{\sin(\delta/2)}{\cos(\delta/2)} = \tan(\delta/2) \tag{3.30}$$

or $\theta = \delta/2$ **(3.31)**

If the analyzer is placed at an angle α from the crossed position then the transmitted field E_A is given by a superposition of equations Eq. **(3.28)** and Eq. **(3.29)** as:

$$\begin{aligned} E_A &= \varepsilon_o \left[\cos(\delta/2)\sin\alpha + \sin(\delta/2)\cos\alpha\right] e^{i(kz-\omega t)} \\ &= \varepsilon_o \sin(\alpha+\delta/2) e^{i(kt-\omega t)} \end{aligned} \tag{3.32}$$

The light intensity I_δ transmitted by the analyzer is then:

$$I_\delta = I_o \sin^2(\alpha+\delta/2) \tag{3.33}$$

and the relative change with respect to I_α is:

$$\frac{\Delta I_\delta}{I_\alpha} = \left(\frac{\sin^2(\alpha+\delta/2) - \sin^2\alpha}{\sin^2\alpha} \right) \tag{3.34}$$

thus, $$\delta = 2\sin^{-1}\left[\left(\frac{\Delta I_\delta}{I_\alpha} + 1 \right)^{1/2} \sin\alpha \right] - 2\alpha \tag{3.35}$$

The steps involved in taking a birefringence measurement and calculating δ for the optical arrangements with and without the quarter-wave plate are very similar. The primary difference between the two methods is in how the measurement of I_α is approached both experimentally and mathematically. For the arrangement involving the presence of the wave plate, the offset angle α is imposed on the system first and then measurements of I_δ and I_α are carried out at the same analyzer angle. Different from the previous section where the offset angle α introduces a background signal which decreases the detection sensitivity for I_δ, in this case, the gain in signal response outweighs the increase in background; assuming that α is kept relatively small.

A simpler experimental approach involving the use of the wave-plate is to DC couple the oscilloscope so that I_δ can be taken as the maximum achieved output voltage and I_α can be taken as the baseline voltage prior to the application of the alignment field. In a DC coupled mode the oscilloscope measures the constant background I_α as well as the additional transient birefringent signal. Careful attention must be paid to the output voltage of the PMT, as its linear response range can be easily exceeded if the DC bias imposed on the system due to the analyzer offset is too large. Thus, in most cases, it's necessary to use a neutral density filter for the probe beam. In contrast, experiments using an analyzer angle of zero are best conducted with the oscilloscope in an AC coupled mode. In this case the scope only measures the net change synchronized with the pulsed electric field. The observed intensity change is equal to I_δ - I_α from Eq. **(3.24)** and I_α is taken from a separate reading.

3.3.3. A Practical Example

In the following example the birefringence of an aqueous CNXL sample was calculated using its TEB signals (**Figure 3.4**) with and without a quarter-wave plate. The birefringent response obtained without the use of the quarter-wave plate has been amplified by a factor of ten for easy comparison.

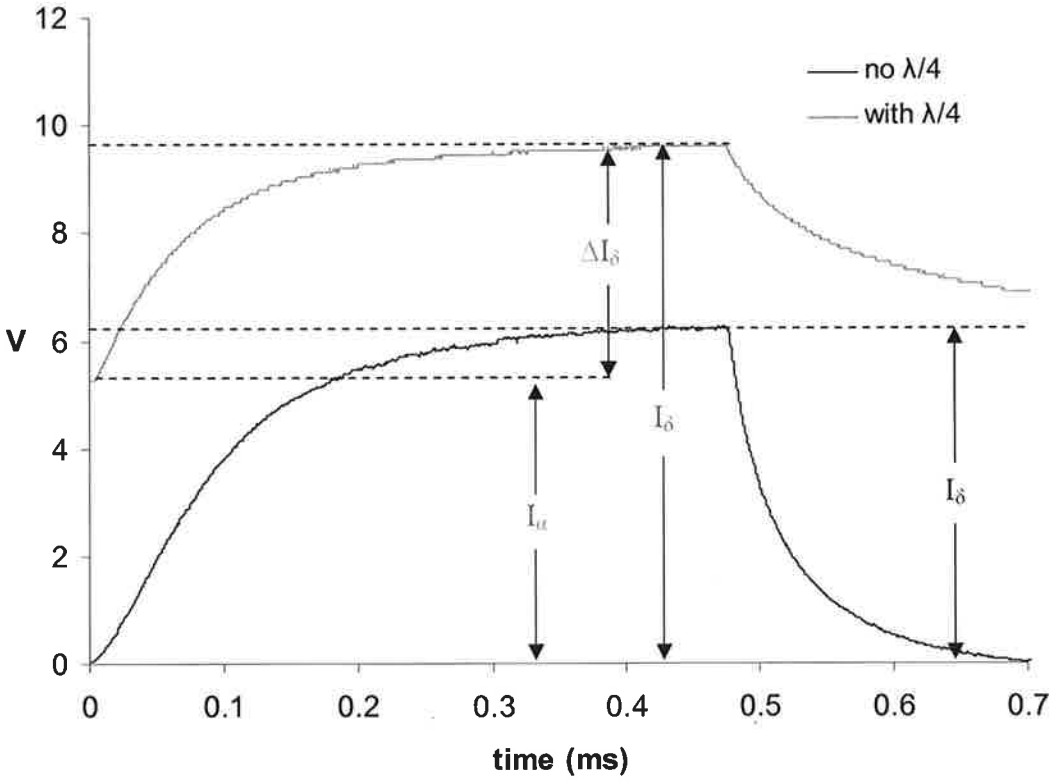

Figure 3.4: Two different TEB signals for a 5.0×10^{-3} wt% CNXL sample in water, taken with and without the use of a quarter-wave plate. The signal obtained without the wave plate has been magnified by 10x. Field = 1.7 kV/cm, applied for 500 μs at 2 Hz. The baseline of the "with $\lambda/4$" signal rests at 5.28V.

<table>
<tr><th>No quarter-wave plate</th><th>With quarter-wave plate</th></tr>
<tr><td colspan="2">With the sample cell absent, optical adjustments were made as stated previously so that the constant background was minimized; indicating that the polarizer and analyzer were crossed and $\alpha = 0$.</td></tr>
<tr><td>1. The sample cell was put into position and a 5.0 kV/cm pulse was applied for 500 μs at 2 Hz.

2. The AC coupled PMT signal was followed on an oscilloscope and its peak value I_δ = .62V was recorded once a sufficient number of averages was achieved (usually 64 to 128).

3. The sample was removed, the analyzer was rotated by eight degrees and the DC signal from the PMT was recorded as $I_\alpha = 5.44V$.

$$\delta = 2\alpha \sin^{-1}\left[\frac{I_\delta}{I_\alpha}\right]^{1/2}$$
$$= 16 \sin^{-1}\left[\frac{.62V}{5.4V}\right]^{1/2} = \pm 5.5^o$$

$$\Delta n = \frac{\delta\lambda}{360l} = \frac{(\pm 5.5)(633\times10^{-9})}{(360)(.01)}$$
$$\Delta n = \underline{\underline{\pm 9.7\times10^{-7}}}$$</td><td>1. The λ/4 plate was put into position and the constant background was minimized a second time.

2. The sample cell was put into position and a 5.0 kV/cm pulse was applied for 500 μs at 2 Hz.

3. The analyzer was rotated eight degrees toward the alignment direction without $V_{max} > 10V$ (PMT's linear range).

4. The DC coupled PMT signal was followed on an oscilloscope and the values ΔI_δ = 4.24V and $I_\alpha = 5.28V$ were recorded.

$$\delta = 2\sin^{-1}\left[\left(\frac{\Delta I_\delta}{I_\alpha}+1\right)^{1/2}\sin\alpha\right] - 2\alpha$$
$$= 2\sin^{-1}\left[\left(\frac{4.9V}{5.3V}+1\right)^{1/2}\sin 8\right] - 16 = 6.3^o$$

$$\Delta n = \frac{\delta\lambda}{360l} = \frac{(6.3)(633\times10^{-9})}{(360)(.01)}$$
$$\Delta n = \underline{\underline{1.1\times10^{-6}}}$$</td></tr>
</table>

An advantage of the optical setup with the quarter-wave plate is its superior sensitivity. As an example, the percent change of light intensity as a function of δ is plotted for an analyzer angle of $\alpha = 5$ in **Figure 3.5**. The $\pi/2$ phase shift imparted by the wave plate has moved the steepest portion of the response curve to the origin. A phase shift of $\delta = 2^{o}$ would yield a 4% change in ΔI without the wave plate and a 44% change with it; as emphasized by the dashed lines.

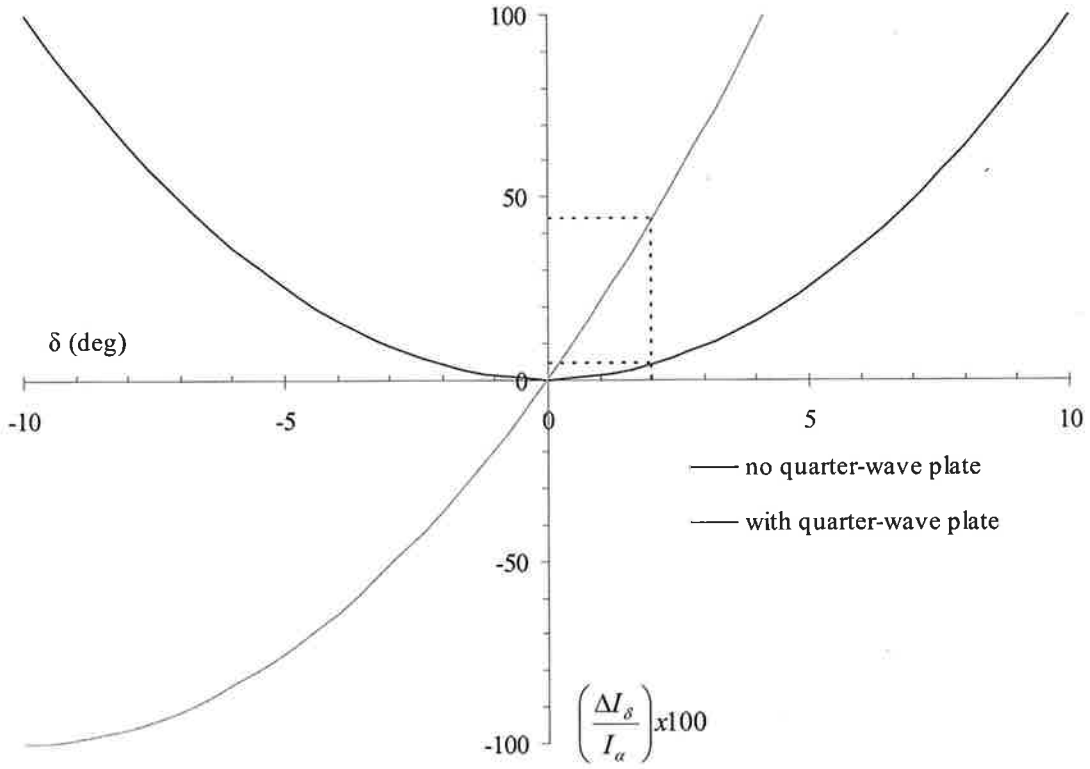

Figure 3.5: Relative change in light intensity as a function of δ ($\alpha = 5^{o}$). Both the increases sensitivity and the ability of the arrangement containing the quarter-wave plate to distinguish between positive and negative birefringence is observed.

In addition, Figure 3.5 also displays another benefit of the quarter-wave plate, i. e., the ability to determine the sign of δ. This is due to the pseudo-linear response with the addition of the wave plate. This point is clearly observable by doing a series expansion on Eq. **(3.25)** and Eq. **(3.33)** at $\delta = 0$. For the response of the birefringence without the quarter-wave plate, Eq. **(3.26)** gives:

$$I_\delta = \sin^2(\delta/2) = \frac{1}{4}\delta^2 - \frac{1}{48}\delta^4 \qquad \textbf{(3.36)}$$

It can be seen from the fist two terms of the series that an even order response with regard to the phase shift δ is observed. Thus, only absolute values can be determined for δ. For the response of the birefringence with the quarter-wave plate, Eq. **(3.33)** gives:

$$\Delta I_\delta = \sin^2(\alpha + \delta/2) - \sin^2\alpha$$

$$= \cos\alpha\delta + \frac{1}{4}(\cos^2\alpha - \sin^2\alpha)\delta^2 - \frac{1}{6}\cos\alpha\delta^3 + \frac{1}{48}(\cos^2\alpha - \sin^2\alpha)\delta^4 \qquad \textbf{(3.37)}$$

However, now both even and odd order terms contribute, and the determination of the sign of δ is possible. Looking at the first term in the series, it is also clear why the arrangement with the quarter-wave plate is more sensitive and displays a linear response. It should be noted that a first order dependence on *cosα* also leaves the intensity change sensitive to the direction in which the analyzer is turned with respect to the alignment field, a situation that will be discussed in detail later.

Each arrangement has its own combination of advantages and limitations. Therefore, careful thought should always be given as to whether the addition of a quarter-wave plate is appropriate. For this reason it is always wise to run preliminary trials on a sample so that parameters such as field strength and solution concentration can be appropriately adjusted. The operator also needs to have a clear understanding of the sources of error involved with each arrangement and how inaccurate settings can affect the outcome of results.

3.3.4. Corrections for Stray Light and Residual Birefringence

Up to this point all discussions have assumed that the light fields are absent of any residual light or residual birefringence. However, in every optical setup some residual light is always present. There are two principle sources of residual light in a TEB setup. The first is from imperfections in the optics which degrade the purity of the polarized HeNe beam. The second is from strain on the optical components and, in particular, the cell windows. Fortunately, the use of an AC coupled setting on the oscilloscope simplifies the problem by cutting out the time independent residual light. This does not, however, resolve the issue for measurements of I_α taken in a DC coupled mode. Therefore, in birefringence calculations, any residual light has to be subtracted from the total light intensity.

The presence of a stray phase is usually an issue only when unknowingly introduced by an inaccurate setting of the analyzer or quarter-wave plate angles. If, on the other hand, it's due to optical strain (most commonly present in the cell window) it

can be easily dealt with as the effect results in an additional phase shift δ_R, which is added to the final expressions. The reader can refer to the complete treatment for the residual light in **Appendix A**; the results of which give the following modification to Eq. **(3.26)**, for the arrangement without a quarter-wave plate:

$$\frac{\Delta I_\delta}{I_\alpha} = \frac{2\sin(\delta/2)\sin(\delta_R + \delta/2)}{1 - \cos 2\alpha \cos\delta_R} \qquad \textbf{(3.38)}$$

If the arrangement includes a quarter-wave plate then the same treatment results in a modification to Eq. **(3.34)** giving:

$$\frac{\Delta I_\delta}{I_\alpha} = \frac{\sin^2(\alpha + \delta/2 + \delta_R/2)}{\sin^2(\alpha + \delta_R/2)} \qquad \textbf{(3.39)}$$

It's clear from Eq. **(3.38)** and Eq. **(3.39)** that if several substances become birefringent in the sample, then the effect is cumulative. One such example is when the solvent contributes to the total signal. In this work, water has been used as the solvent in all cases. Fortunately, water has a very weak birefringent response, owing to its small Kerr constant of 3.1×10^{-14} m^2V^{-2}, determined using the current setup and verified with the literature value.[11] Thus, its effect on the results should be negligible.

Stray phases can also influence the calculation of decay times, particle dimensions, and polarizability anisotropies. Detailed discussions on these properties will be addressed in the relevant sections.

3.4. Experimental Considerations

The system described has the advantage of providing accurate, quantitative measurements of birefringence, rise times, and relaxation times of very dilute solutions in any non-conducting solvent. It is also very versatile since it allows studies at field strengths ranging from .02 to 5.0 kV/cm. However, as is the case with any sensitive device, the system is ultimately constrained by the physical properties and limitations of its components. Because of the straight forward nature of the TEB setup, it is rare for inaccurate instrument settings or component limitations to render the system inoperable. Instead they often result in false data which can be very difficult to decipher from true values. The following section breaks down the system piecewise, and addresses concerns surrounding each component. The section will be concluded with a control study on nitrobenzene, for which the Kerr constant is calculated and compared to the accepted value, as a test to the system's reliability.

3.4.1. Light Source

The HeNe laser used in this experiment was purchased from Thorlabs and produces a constant 5.0 mW beam with a >500:1 polarization ratio at a wavelength of 632.8 nm. The beam has a Gaussian mode structure >99%, with an initial $1/e^2$ diameter of .88 mm and a divergence of 1.00 mrad.

3.4.2. Detection System

The use of a photomultiplier tube (PMT) is advantageous because of its high sensitivity to light intensity changes. However, careful attention must be paid to the voltage output of the PMT to make sure it does not exceed its linear range. **Figure 3.6** shows the response of the detection circuit by plotting the output voltage read on the oscilloscope against the relative laser intensity of the probe beam. This was accomplished by by crossing two polarizers and measuring the intensity change using Malus' law ($I = I_o \cos^2\theta$). It can be seen that output voltages between 0 and 10 volts exhibit the desired response.

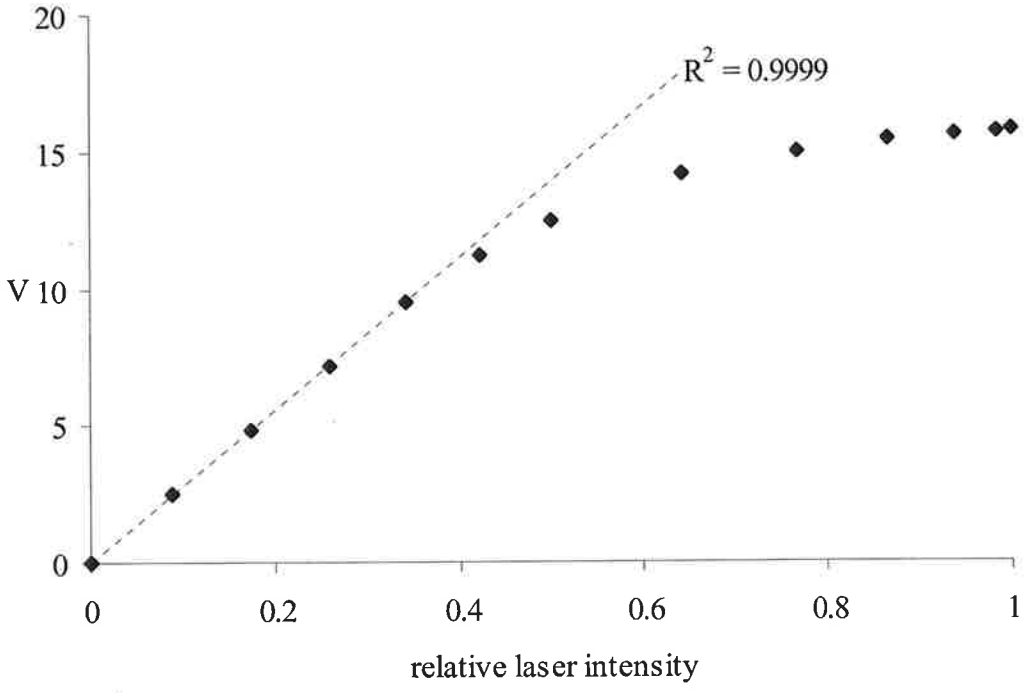

Figure 3.6: PMT response as a function of laser intensity. Output voltages between 0 and 10 V display the desired linearity.

3.4.3. Kerr Cell

The Kerr cell used in **Figure 3.7** is similar to that described by O'Konski and Haltner.[2] As discussed in an earlier section, it is of high importance that a Kerr cell with a minimal birefringence is used in order to avoid the introduction of stray phases to the system. The 1 cm path length quartz cuvette was chosen because its own optical retardation δ_o is small ($\delta << 1^o$); calculated as follows:

$$I_{\delta o} = 28 \text{ mV} \quad I_\alpha = (3.88/.024) \text{ V} \quad \alpha = 2^o$$

$$\delta = 2\sin^{-1}\left[\left(\frac{.028}{162}+1\right)^{1/2}\sin 2\right] - 2(2) = 3.5x10^{-4^o}$$

$$\Delta n = \frac{\delta\lambda}{360l} = \frac{(3.5x10^{-4})(633\times10^{-9})}{(360)(.01)}$$

$$\Delta n = \underline{\underline{6.1\times10^{-11}}}$$

For this particular measurement, the presence of dust on both the outside and inside of the sample cell is a concern. Therefore, the cuvette was washed and allowed to air dry before the measurement was made. The value of $I_{\delta o}$ was taken as the difference between the baseline voltage on the oscilloscope, with and without the sample cell in place. The same 2.4% neutral density filter used for testing the linearity of the PMT was also used in the measurement of I_α in order maintain the proper PMT response. The subsequent voltage reading was then scaled up to its appropriate value. This

technique was used multiple times in the course of this research and will be seen again in following sections.

Teflon inserts of varying width (1 – 3mm) are used to space the stainless steel electrodes based on the field strength desired for a particular trial. The cell holder is also made of Teflon and is machined so that the cell fits snuggly but with minimal strain applied to its sides. The filling of the cell must be made carefully so that the electrodes are completely immersed and no air bubbles are present. The reader may have noted earlier that the sensitivity of the birefringence measurements could be enhanced by increasing the path-length of the Kerr cell per Eq. **(2.31)**. However, it's appropriate to mention here that the limitations due to conductivity would be correspondingly higher.

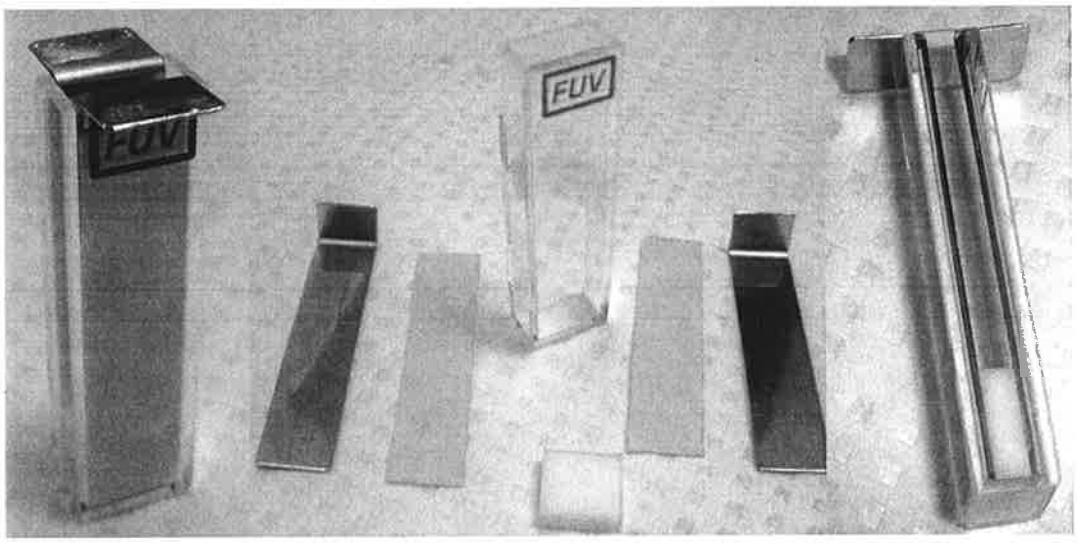

Figure 3.7: Varying angles showing the 1 cm path length Kerr cell and its parts.

3.4.4. Electronics

When applying pulsed fields and monitoring time dependent signals, it's important to confirm that the frequency responses of the electronic devices exceed that of the system being studied. In this case, the primary concern is that the rise and decay times of the power supplies are fast enough to produce adequately shaped square waves for the application.

The fastest signals studied in the context of this research are the rise times of quantum dot samples which are on the order of ~10 μs. Thus, a frequency response greater than 100 kHz is required for each of the electrical components. The specifications outlined in **Table 3.1** show that the required frequency response is mostly exceeded, although the bandpass of the amplifier is not ideal

Table 3.1: Performance specifications of electrical components.

Component	**Vertical Bandwidth**	**Rise/Fall Time**	**Horizontal Sample Rate**
Tektronix TDS2024B Oscilloscope	200 MHz	< 2.1 ns	2 GHz
	Frequency	**Rise/Fall Time**	**Minimum Pulse Width**
Tektronix AFG3021B Function Generator	25 MHz	≤ 18 ns	30 ns
Princeton Applied Research High Voltage Pulse Generator Model 1211	1 MHz	≤ 500 ns	2.5 μs
Krohn-Hite DC Amplifier Model 7500	1 MHz	< 500 ns	5 μs

The field strengths used in this study were achieved by combining the function generator, pulsed voltage generator, and amplifier in one of the two configurations. **Figure 3.8** gives the first of the two, which was used to apply square waves and pulsed AC fields ranging from 0.02 to 0.20 kV/cm. The function generator is used to produce a 2 V square wave which is then run through the amplifier, allowing amplification from 2 to 200 V. A separate TTL pulse is also sent out from the function generator and used as a trigger for the oscilloscope. The form of the field after amplification is then followed on the scope by connecting a scope probe directly to the electrodes in the sample cell.

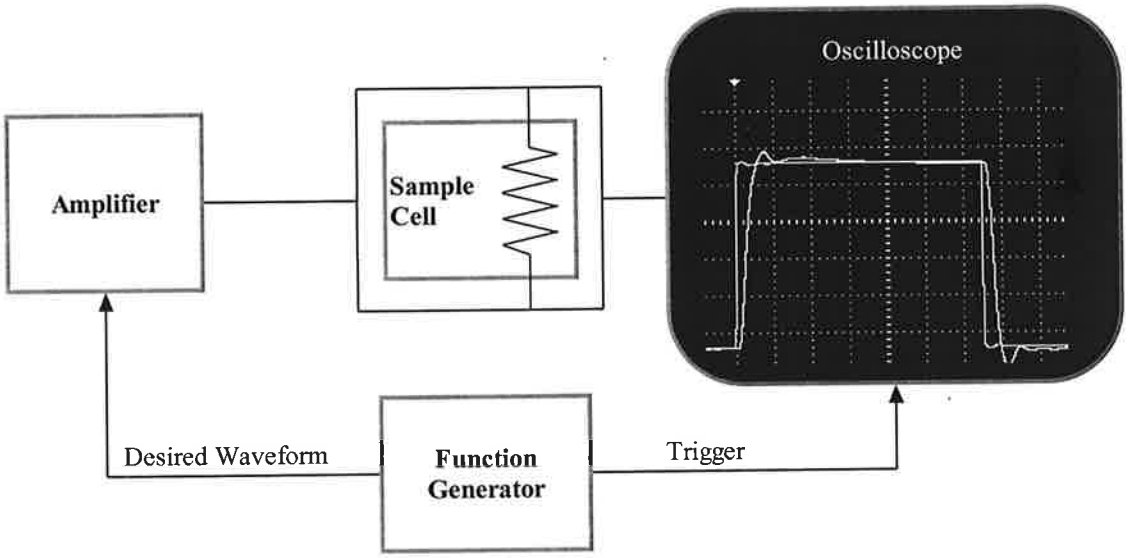

Figure 3.8: Electronics configuration used to apply low voltage, pulsed square and AC fields. The green square wave is the pulse monitored from the function which is also used to trigger the scope. The blue square wave is the pulse measured directly at the sample cell.

Although functional, this configuration is somewhat problematic because the signal is small and interference from the amplifier can occasionally cause problems; owing to its close proximity to the other electrical components. There is also an overshoot of approximately 5% after the amplifier due to impedance mismatch. However, for this study, an overshoot of such a small magnitude does not pose a significant problem.

The arrangement used to apply square waves from 0.5 to 5.0 kV/cm is shown in **Figure 3.9**. In this case the function generator's only purpose is to trigger the high voltage pulse generator (HVPG) which then applies the alignment field across the sample cell. The voltage across the cell is monitored internally by the HVPG and used as a trigger for the oscilloscope.

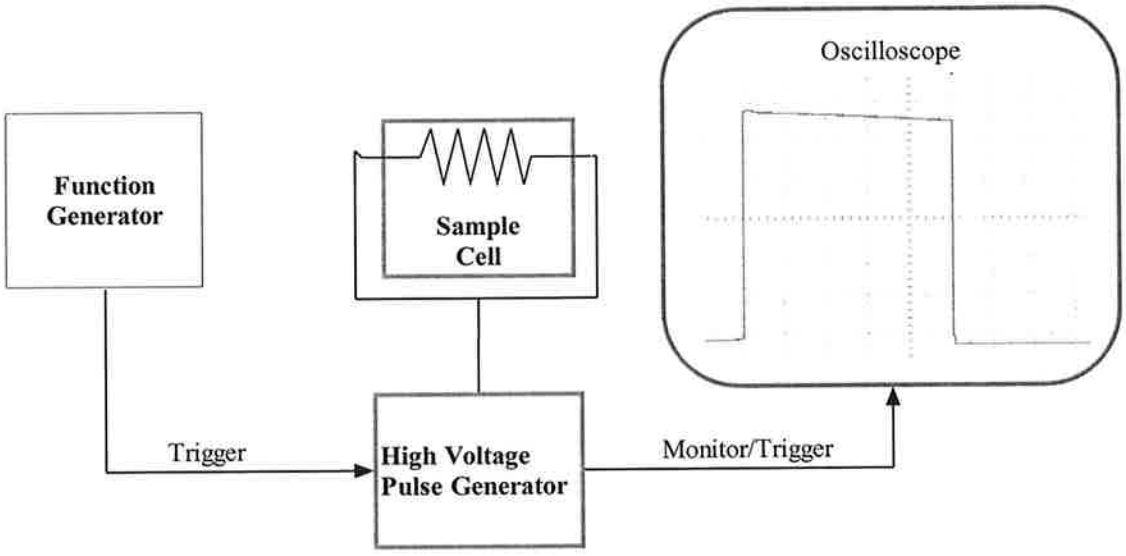

Figure 3.9: Electronics configuration used to apply high voltage, pulsed square waves. The function generator triggers the HVPG which then applies the alignment field across the sample cell, while monitoring the voltage and sending it as a trigger to the scope.

There have been many reports of TEB studies with high voltage pulsers achieving 6 kV/cm but limitations in current at high fields become important. Higher fields generate higher currents in a fixed sample cell, easily overloading the power supply. Thermal effects due to conductivity are also a concern as many of the physical properties being studied are functions of temperature. For the current study, we have limited the field strength to 5.0 kV/cm and repetition rates to 2 Hz. Under these conditions, the temperature within the sample was maintained as was evident by the stability of the signal over several minutes.

3.4.5. Control Experiment – Kerr Constant of Nitrobenzene

In order to test the functionality and accuracy of the system, the birefringent response of nitrobenzene was measured and its Kerr constant was calculated for comparison with its literature value. By plotting $\Delta n/\lambda$ as a function of E^2, it is possible to determine the Kerr constant K by simply fitting the data to a straight line based on the following rearrangement of the Kerr Law:

$$\Delta n / \lambda = KE^2 + b \qquad \textbf{(3.40)}$$

where b is the y-intercept and should be very close to zero. A total of ten measurements were taken at field strengths ranging from 1.7 – 5.8 kV/cm. **Figures 3.10 & 3.11** show the results of the birefringent measurements and calculation of K respectively. The result for the linear fit of the data gives a Kerr

constant for nitrobenzene of $K = 2.25 \times 10^{-12}$ m/V^2, which is within 0.9% of its accepted value of 2.23×10^{-12} m/V^2.[8]

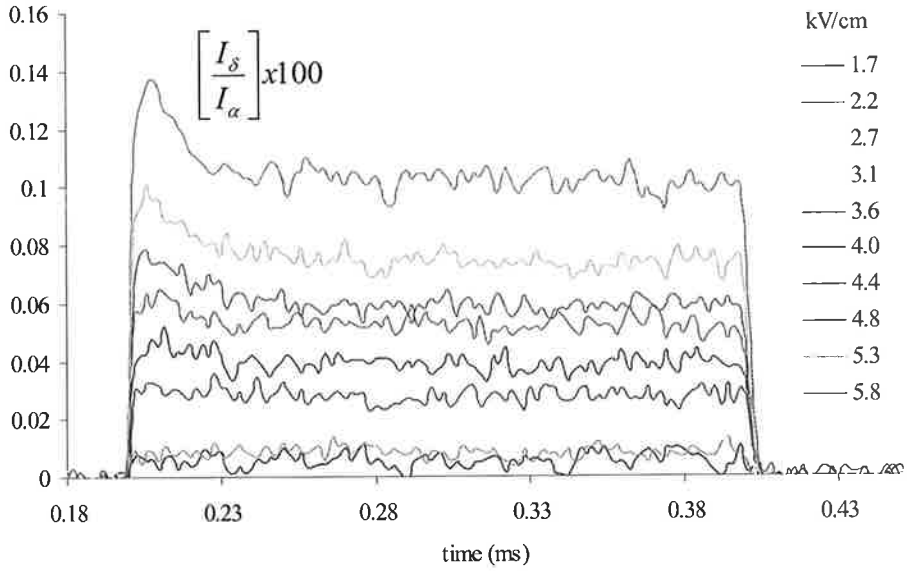

Figure 3.10: Birefringent response of nitrobenzene upon application of alignment fields of varying strength.

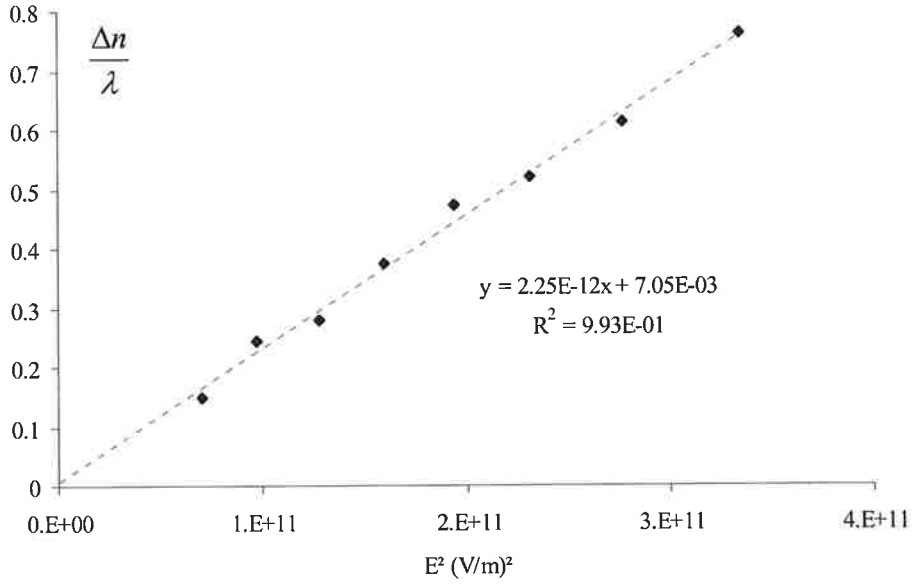

Figure 3.11: Plot of the birefringence of nitrobenzene as a function of the square of the field strength.

3.5. References

1. Prasse, T., J.-Y. Cavaille, and W. Bauhofer, *Electric anisotropy of carbon nanofibre/epoxy resin composites due to electric field induced alignment.* Composites Science and Technology, 2003. **63**(13): p. 1835-1841.

2. O'Konski, C.T. and S. Krause, *Electric birefringence and relaxation in solutions of rigid macromolecules.* Electro-Optics Series, 1976. **1**(Mol. Electro-Opt., Pt. 1): p. 63-120.

3. Shah, M.J., *ELECTRIC BIREFRINGENCE OF BENTONITE. II. AN EXTENSION OF SATURATION BIREFRINGENCE THEORY.* Journal of Physical Chemistry, 1963. **67**(10): p. 2215-2219.

4. Benoit, H., *Electric birefringence of thymonucleic acid.* Journal de Chimie Physique et de Physico-Chimie Biologique, 1951. **48**: p. 612-14.

5. Rogers, S.S., et al., *Electric birefringence study of an amyloid fibril system: The short end of the length distribution.* European Physical Journal E: Soft Matter, 2005. **18**(2): p. 207-217.

6. Holcomb, D.N. and I. Tinoco, *Electrical Birefringence at High Fields.* Journal of Physical Chemistry, 1963. **67**(12): p. 2691-2698.

7. Khoshsima, H., et al., *Electro-Optical Kerr Effect of Two High Birefringence Nematic Liquid Crystals.* J. Phys. D: Appl. Phys., 2006. **39**: p. 1495-1499.

8. Hisakado, Y., et al., *Large Electro-Optic Kerr Effect in Polymer-Stabilized Liquid-Crystalline Blue Phases.* Adv. Mater., 2005. **17**(1): p. 96-98.

9. Ridgeway, D., *Transient Electric Birefringence of Suspensions of Asymmetric Ellipsoids.* Journal of the American Chemical Society, 1966. **88**(6): p. 1104-1112.

10. Elias, J.G. and D. Eden, *Transient electric birefringence study of the length and stiffness of short DNA restriction fragments.* Biopolymers, 1981. **20**(11): p. 2369-80.

11. Beevers, M. and G. Khanarian, *Measurement of Kerr Constants of Conducting Liquids.* Australian Journal of Chemistry, 1979. **32**(2): p. 263-269.

4. Birefringence and the particle alignment parameter

4.1. Birefringence and polarizability anisotropy

The optical polarizability α^o is frequently used in relationships involving the refractive index of a material and will be introduced here. Its relation to the refractive index of a pure material is given by the Lorentz-Loren equation as:[1]

$$\frac{n^2-1}{n^2+2}=\frac{N\alpha^o}{3\varepsilon_o} \tag{4.1}$$

which, when applied to a solution of anisotropic particles, takes on the value:

$$\Delta n_s=\frac{N}{2n\varepsilon_o}\Delta\alpha^o \tag{4.2}$$

where Δn_s is the saturation birefringence, n is the refractive index of the solution and $\Delta\alpha^o$ is the difference in the polarizability between two axis in the particles. The above expression for the saturation birefringence Δn_s relates the birefringence of a solution to the total number of solute particles. Another common approach is to relate Δn_s to the volume fraction C_v of the particles, in which case we consider the intrinsic anisotropy factor g_i along direction i.[2] For a solution of particles which are large compared to the solvent molecules, the induced dipole is related to the light field E_i through:

$$\mu_i^o=\alpha_i^o E_i=4\pi\varepsilon_o' v g_i E_i \tag{4.3}$$

where v is the volume of a single particle. By combining Eqs. **(4.2)** and **(4.3)** we get:

$$\Delta n_s=\frac{2\pi N v\Delta g}{n} \tag{4.4}$$

where $\Delta g = \alpha_{ll}^{o} - \alpha_{\perp}^{o}$. In dilute solutions Nv is very small compared to $N_w v_w$, where N_w and v_w are the number of solvent molecules per cm^3 and the volume of each solvent molecule respectively. The volume fraction of the solute can then be expressed as:

$$C_v = \frac{Nv}{Nv + N_w v_w} \cong \frac{Nv}{N_w v_w} \cong Nv \qquad \textbf{(4.5)}$$

and Eq. **(4.4)** becomes:

$$\Delta n_s = \frac{2\pi C_v \Delta g}{n} \qquad \textbf{(4.6)}$$

The expression for Δn_s in Eq. **(4.6)** corresponds to the maximum achievable birefringence when all the particles in the solution are aligned. In a more general scenario when a particle has an orientation angle θ with respect to the field direction, the resulting birefringence is also affected by the angular distribution of the birefringent material.

4.2. Birefringence and particle alignment

When an electric field is applied onto a material, it generates a polarization vector P, such that:

$$P = \frac{N}{3\varepsilon_o'}\left[\alpha_e + \alpha_i + \frac{\mu^2}{3kT}\right]E \qquad \textbf{(4.7)}$$

where α_e and α_i are the electronic and interfacial polarizabilities respectively, and μ is the permanent dipole moment of individual particles. In an optical field, the electronic polarizability is the only component in P because the frequency is too high for the other two terms to contribute; hence, α_e is identical to the optical polarizability α^o discussed earlier. In insulating media, the interfacial polarizability term is nonexistent and so the effective polarizability is equal to α_e at optical frequencies and $\alpha_e + \mu^2/3kT$ at lower frequencies. In electrolytic solutions, however, the interfacial term α_i may dominate; arising from the movement of counterions along the surface of the particle under the influence of an external field.[3] The permanent dipole is unaffected by the ionic nature of the solution, constrained only by the frequency range of the applied field.

Regardless of the contributing factors in the polarization vector, the interaction of the electric field with the polarizability vector is to minimize the electrostatic energy of the system, by aligning the polarizability anisotropy and/or the permanent dipole of the system with the field. More specifically, the application of an electric field can produce orientation through two main parameters:

1. The induced dipole, characterized by a nine element polarizability tensor, with each element having possible contributions from the electronic and interfacial polarizabilities $\alpha_e + \alpha_i$.
2. The permanent dipole of the particle, which has a fixed direction in the molecular frame.

In the following discussion, we will use the molecular frame that corresponds to the diagonalized polarizability tensor to simplify the picture. In addition, we assume cylindrical symmetry for the particle, with one component lying along the symmetry axis and the other two equal and perpendicular to it, as shown in **Figure 4.1**. The permanent dipole is also parallel to the symmetry axis of the particle. We will consider the electrostatic energy due to the interaction of the field with the induced-dipole $E \cdot \alpha \cdot E$, directed along the lab fixed Z direction. The energy due to the permanent dipole $\mu \cdot E$ will be added in the following section.

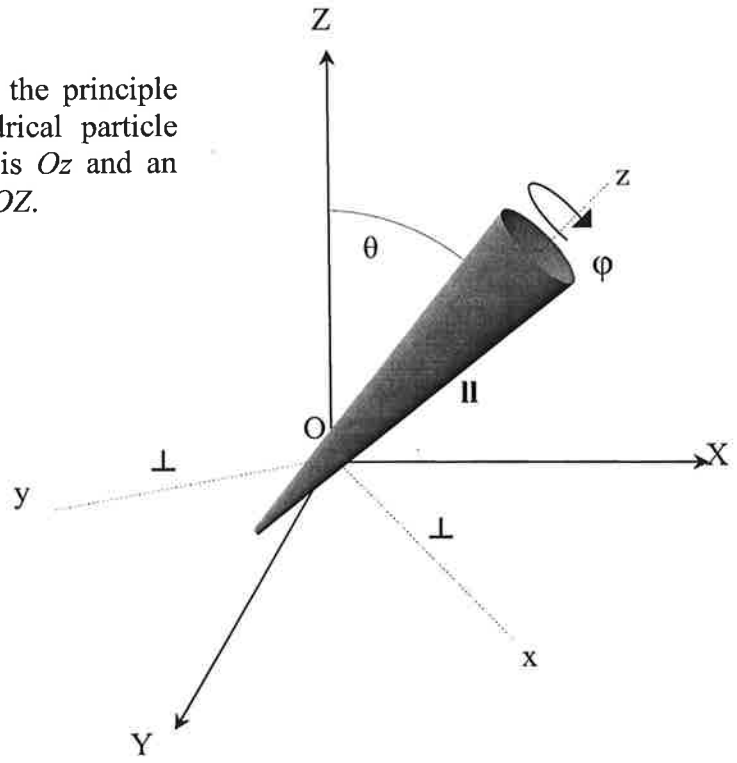

Figure 4.1: Orientation of the principle polarizabilities of a cylindrical particle with respect to its long axis *Oz* and an applied electric field along *OZ*.

We begin by assuming that the particles are oriented with their long axes z at an angle θ with respect to the direction of an applied electric field Z. In addition, the particles are free to rotate around Z so that they are uniformly distributed around the angle φ. Thus, because the electric field is applied along the Z direction only, the alignment of the particle can be followed as a function of the single angle θ.

To calculate the potential energy of the particle in an electric field, the polarizability and the electric field need to be expressed in the same reference frame. The polarizability in the laboratory frame can be calculated using the rotation matrix and its transpose:

$$\overline{\overline{R}}^{T} \cdot \overline{\overline{\alpha}} \cdot \overline{\overline{R}} = \begin{bmatrix} C\theta & 0 & S\theta \\ 0 & 1 & 0 \\ -S\theta & 0 & C\theta \end{bmatrix} \begin{bmatrix} \alpha_{\perp} & 0 & 0 \\ 0 & \alpha_{\perp} & 0 \\ 0 & 0 & \alpha_{II} \end{bmatrix} \begin{bmatrix} C\theta & 0 & -S\theta \\ 0 & 1 & 0 \\ S\theta & 0 & C\theta \end{bmatrix} \qquad \textbf{(4.8)}$$

where $C = cos$ and $S = sin$. For a cylindrical particle along the lab fixed Z axis we get:

$$\alpha_Z = \alpha_{II} \cos^2\theta + \alpha_{\perp} \sin^2\theta \qquad \textbf{(4.9)}$$

Then, after some algebra, the energy of the particle in the field can be expressed as:

$$U_{\alpha} = \frac{(2\alpha_{II} + \alpha_{\perp})}{3} E^2 + \frac{2(\alpha_{II} - \alpha_{\perp})}{3} \left[\frac{3\cos^2\theta - 1}{2} \right] E^2 \qquad \textbf{(4.10)}$$

where $U_{\alpha} = E \cdot \alpha_z \cdot E$. The term in the square brackets is the second order Legendre polynomial, or alignment parameter $P_2(\theta)$. Eq. **(4.6)** represents the effective optical

anisotropy for a system with all particles oriented at an angle θ, and it can be combined with Eq. **(4.10)** to give the resulting birefringence as a function of θ:

$$\Delta n_\theta = \Delta n_s \left[\frac{3\cos^2\theta - 1}{2} \right] \qquad \textbf{(4.11)}$$

In a more general case, when an angular distribution function $f(\theta)$ is used to express the probability of finding the molecular axis at an angle between θ and $\theta + d\theta$, the birefringence should be:

$$\Delta n = \Delta n_s \int_0^\pi f(\theta) \frac{3\cos^2\theta - 1}{2} 2\pi \sin\theta d\theta \qquad \textbf{(4.12)}$$

Eq. **(4.12)** shows that if all the particles are oriented parallel to the alignment field with $\theta = 0$, then $\Delta n = \Delta n_s$. In contrast, if all the particles are perpendicular to the alignment field with $\theta = 90^\circ$, then $\Delta n = -\frac{1}{2}\Delta n_s$. The factor of ½ is a consequence of the fact that there are two directions in the plane perpendicular to the field. Finally, the integrand of Eq. **(4.12)** is the average value of the alignment parameter $\langle P_2(\theta) \rangle$, thus Eq. **(4.11)** can be rewritten as:

$$\Delta n = \Delta n_s \langle P_2(\theta) \rangle \qquad \textbf{(4.13)}$$

4.3. Calculation of the alignment parameter $P_2(\theta)$

To calculate $P_2(\theta)$ we need to consider the overall interaction of a particle with an external field. To make the discussion general, we assume that the orientation field can be either DC or AC. Thus, in addition to the electrostatic energy between the field and the induced dipole U_α, the overall static energy also includes a term due to the permanent dipole U_μ, when the orientation field is DC or low frequency AC, given as:

$$U_\mu = -\mu E \cos\theta \tag{4.14}$$

The angular distribution function $f(\theta)$ follows the Boltzmann distribution formula:

$$f(\theta) = \frac{\exp(-U/kT)}{2\pi \int_0^\pi \exp(-U/kT)\sin\theta d\theta} \tag{4.15}$$

Using Eq. **(4.12)** for $f(\theta)$, the total alignment parameter $\langle P_2(\theta)\rangle$ has been solved and designated $\langle P_2(\beta,\gamma)\rangle$, with the two terms β and γ corresponding to the following:[4]

$$\beta = \frac{\mu E}{kT} \tag{4.16}$$

$$\gamma = \frac{(\alpha_{II} - \alpha_\perp)E^2}{2kT} \tag{4.17}$$

where the β and γ terms result from the interactions of the permanent and induced-dipole moments with the applied field, respectively; each representing the ratio of the

given moment with the thermal energy. The complete $\langle P_2(\beta,\gamma)\rangle$ function is very complicated, having the form:

$$\langle P_2(\beta,\gamma)\rangle = \frac{3}{4\gamma}\times \left[\frac{e^{(\beta^2/4\gamma)}+\gamma\left\{\sqrt{\gamma}\left(e^{\beta}+e^{-\beta}\right)-\left(\beta/2\sqrt{\gamma}\right)\left(e^{\beta}-e^{-\beta}\right)\right\}}{E\left(\beta/2\sqrt{\gamma}+\sqrt{\gamma}\right)-E\left(\beta/2\sqrt{\gamma}-\sqrt{\gamma}\right)}+\frac{\beta^2}{2\gamma}-1\right]^{-\frac{1}{2}} \qquad \textbf{(4.18)}$$

However, there are four specific cases when simplifications occur:

1) For a pure permanent moment orientation where $\beta >> \gamma$, the integral yields:

$$\langle P_2(\beta)\rangle = 1-\frac{3\left(\coth\beta-\frac{1}{\beta}\right)}{\beta} \qquad \textbf{(4.19)}$$

2) For a pure induced moment orientation where $\gamma >> \beta$ the integral does not have an analytical solution giving:

$$\langle P_2(\gamma)\rangle = \frac{3}{4}\left[\left(e^{\gamma}/\gamma^{1/2}\int_0^{\gamma^{1/2}}e^{x^2}dx\right)-1/\gamma\right]-\frac{1}{2} \qquad \textbf{(4.20)}$$

3) When the field strength approaches zero, β and $\gamma << 1$ and $\langle P_2(\beta,\gamma)\rangle$ can be expanded in the series:

$$\langle P_2(\beta,\gamma)\rangle = \frac{2}{15}\gamma+\frac{1}{15}\beta^2+\frac{4}{315}\gamma^2+\frac{4}{315}\beta^2\gamma-\frac{2}{315}\beta^4\ldots \qquad \textbf{(4.21)}$$

where the limit is given by:

$$\lim_{E\to 0}\frac{\langle P_2(\beta,\gamma)\rangle}{(\beta^2+2\gamma)}=\frac{1}{15} \qquad \textbf{(4.22)}$$

4) At high field strengths where E → ∞, the orientation tends to be complete, and the function $\langle P_2(\beta,\gamma)\rangle \to 1$. Then the birefringence attains its saturation value, which allows for the calculation of the anisotropy factor Δg from Eq. **(4.16).**

4.4. Permanent vs. induced dipoles – intermediate field strength

If we divide both side of Eq. **(4.13)** by the square of the field E^2, the result is:

$$\frac{\Delta n}{E^2}=\frac{\Delta n_s}{E^2}\langle P_2(\beta,\gamma)\rangle \qquad \textbf{(4.23)}$$

The combination of Eq. **(4.22)** with Eq. **(4.23)** then yields:

$$\left[\frac{\Delta n}{E^2}\right]_{E\to 0}=\frac{\Delta n_s}{15E^2}(\beta^2+2\gamma) \qquad \textbf{(4.24)}$$

so that

$$\frac{(\Delta n/E^2)}{(\Delta n/E^2)_{E\to 0}}=\frac{15\langle P_2(\beta,\gamma)\rangle}{(\beta^2+2\gamma)} \qquad \textbf{(4.25)}$$

The relationship expressed in Eq. **(4.24)** is significant because it shows the relative contributions of the permanent and the induced-dipoles in an electric field to the alignment mechanism. An example of this analysis can be seen in **Figure 4.2** where

the right side of Eq. **(4.25)** is plotted as a function of $\log(\beta^2 + 2\gamma)$. In the case of a pure permanent dipole, the value of $\langle P_2(\beta)\rangle / \beta^2$ was determined using Eq. **(4.19)**. The expression for $\langle P_2(\gamma)\rangle / 2\gamma$ is not analytical, so the value was obtained using a table supplied by O'Konski, Yoshioka, and Orttung.[4]

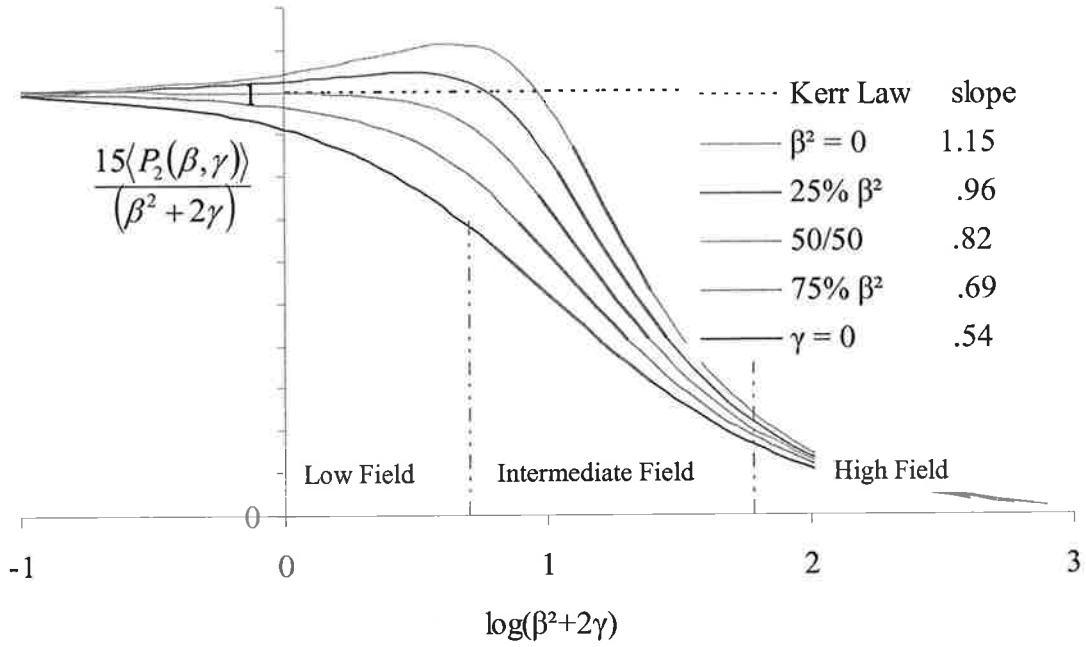

Figure 4.2: Variation of $15\langle P_2(\beta,\gamma)\rangle/(\beta^2+2\gamma)$ vs $\log(\beta^2+2\gamma)$ for orientations ranging from a pure induced dipole ($\beta = 0$) to a pure permanent dipole ($\gamma = 0$).

In low fields where $E^2 \rightarrow 0$, the birefringence follows the Kerr law and the function retains a value close to unity. As the field strength increases the birefringence will begin to deviate from unity in a manner that is influenced by the relative contributions of the permanent and the induced-dipole. A purely permanent-dipole mechanism results in a curve that starts at unity and immediately begins to decrease with

increasing field strength. In contrast, a purely induced-dipole mechanism results in a curve that rises above unity first, and then begins to decrease after attaining a maximum value of 1.11. At intermediate fields, the alignment due to the two mechanisms decreases linearly as a function of log E^2. Thus, by measuring the dependence of $\langle P_2(\beta,\gamma)\rangle$ as a function of E^2, one can obtain a quantitative description of the alignment mechanism, which gives the relative contributions of permanent and induced dipoles to the birefringence of a sample. We can further extend this idea by relating the fractional contribution of the permanent and induced dipole to the slopes in the linear region, as shown in **Figure 4.3**. The change in slope, as the fraction of β^2 and 2γ changes, is also linear. Thus, plotting the change relative to the fractional contribution of each component, yields:

$$y = 1.67x + 1.88 \qquad \textbf{(4.26a)}$$

and

$$y = -1.67x - .88 \qquad \textbf{(4.26b)}$$

where x is the range of the slope from -.53 to -1.13, and y is the fractional contribution from β^2 or 2γ, respectively. At low fields the observed birefringence from the permanent dipole contribution is linear to the field and the induced dipole contribution is square to the field. However, we can still consider the relative contributions from each at intermediate field because the alignment is saturated and so the ratio of each to the squared field strength decreases linearly as a function of log E^2. In addition, the range of the slope is limited and so any value outside of the rage (-.54 to -1.15) would be due to stray fields, as will be discussed in **Section 4.7**.

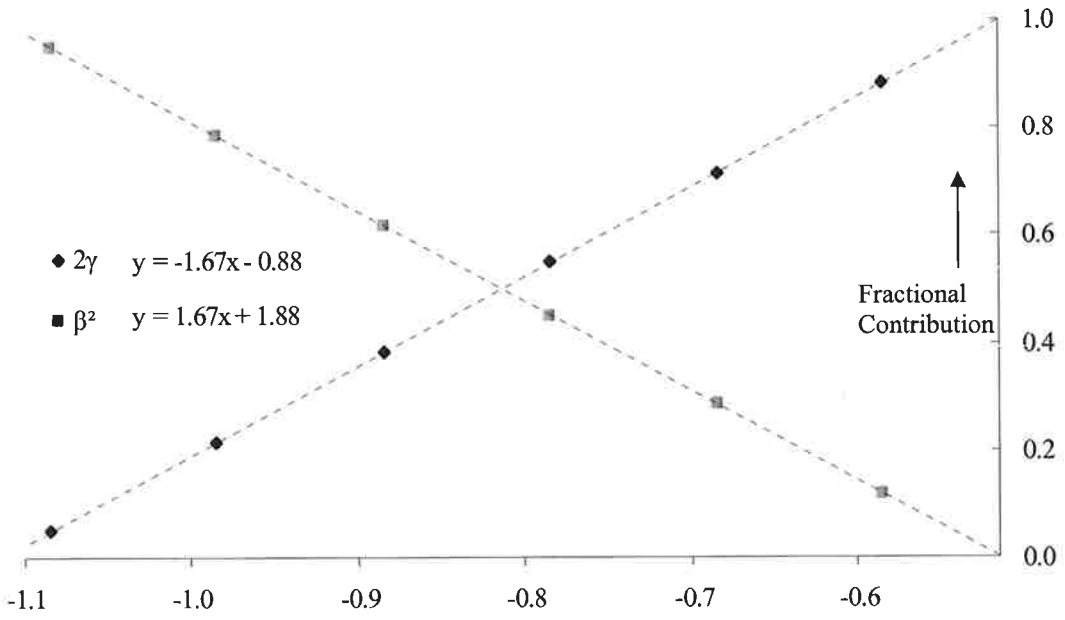

Figure 4.3: The fractional contributions from the two moments as a function of the slope of $15\langle P_2(\beta,\gamma)\rangle/(\beta^2+2\gamma)$ vs $\log(\beta^2+2\gamma)$.

4.5. Permanent vs. Induced Dipoles – Low Field Strength

The determination of the specific Kerr constant K_{sp} requires extrapolation to zero fields so the measurements need to be conducted down to the region of low fields. In this case the Kerr constant is obtained by inserting Eq. **(4.6)** into Eq. **(4.24)**. The resulting expression relates the birefringence in the low field limit to the optical anisotropy:

$$\lim_{E\to 0}\left[\frac{\Delta n}{E^2}\right] = \Delta g \frac{2\pi C_v}{15n}(P+Q) \qquad \textbf{(4.27)}$$

where P, the permanent dipole term, is $P = \beta^2/E^2 = \mu^2/k^2T^2$ and Q, the induced dipole term is $Q = 2\gamma/E^2 = \Delta\alpha/kT$. Eq. **(4.27)** can then be rewritten as:

$$\lim_{E\to 0}\left[\frac{\Delta n}{E^2}\right] = K_{sp}C_v n \qquad \textbf{(4.28)}$$

where K_{sp} is the specific Kerr constant defined as:

$$K_{sp} = \frac{2\pi\Delta g}{15n^2}(P+Q) \qquad \textbf{(4.29)}$$

Thus, the values of μ and $\Delta\alpha$ can be calculated for a pure permanent moment ($Q = 0$) or for a pure induced moment ($P = 0$) directly, once K_{sp} and Δg are known. However, as will be seen for CdSe quantum dots, situations will arise where the contribution from each moment is significant. In these cases additional information is needed if the values of P and Q are to be determined.

4.6. Separation of the Permanent and Induced Dipoles

To determine the values of the permanent dipole and polarizability anisotropy from the saturation values of the refractive index, we need to rely on information from both **Section 4.4** and **4.5**. In Section 4.4, it was shown that the linear region of the response curve at intermediate fields could be used to determine the ratio of permanent μ to induced-dipole $\Delta\alpha$. Then, in Section 4.5, the sum of $P = \beta^2/E^2$ and $Q = 2\gamma/E^2$ were introduced with Eq. **(4.37)**. Thus, in determining the ratio of β^2 to 2γ, the ratio of P to Q was determined as well. To further determine the values of P and Q, we can take

advantage of the relation in Eq. **(4.34)**, Where the lateral displacement of the experimental curve, to overlap with the theoretical result can be used:

$$\log\left(\beta^2 + 2\gamma\right) = \log\left(P + Q\right) + \log E^2 \qquad \textbf{(4.30)}$$

An example of the process can be seen in **Figure 4.4** where an experimental curve is shown to require a shift of $log(P + Q) = 0.5$ in order to overlap with the theoretical curve. The unit of $P + Q$ will be the same as that of $\Delta n/E^2$, and for this example, a value of $P + Q = 3.16\ m^2/V^2$ is obtained from the horizontal shift. This value can then be combined with their ratio (Eq. **(4.26)**) to solve for each unknown.

The steps necessary to determine the values of μ and $\Delta\alpha$ from the birefringence measurements can be summarized as follows:

1) The birefringence values at varying field strengths are normalized by taking $\left(\Delta n / E^2\right)/\left(\Delta n / E^2\right)_{E\to 0}$ and plotting it as a function of $log\ E^2$.

2) The slope of the plot in its linear region, at intermediate field strengths is determined and Eq. **(4.26)** is used to calculate the relative contributions from β^2 and 2γ and hence the ratio P/Q.

3) The experimental and theoretical curves are plotted together and the experimental curve is shifted horizontally until the two overlap.

4) The sum $P + Q$ determined from Eq. **(4.30)** is combined with the ratio P/Q determined from Eq. **(4.26)** and the two can be determined.

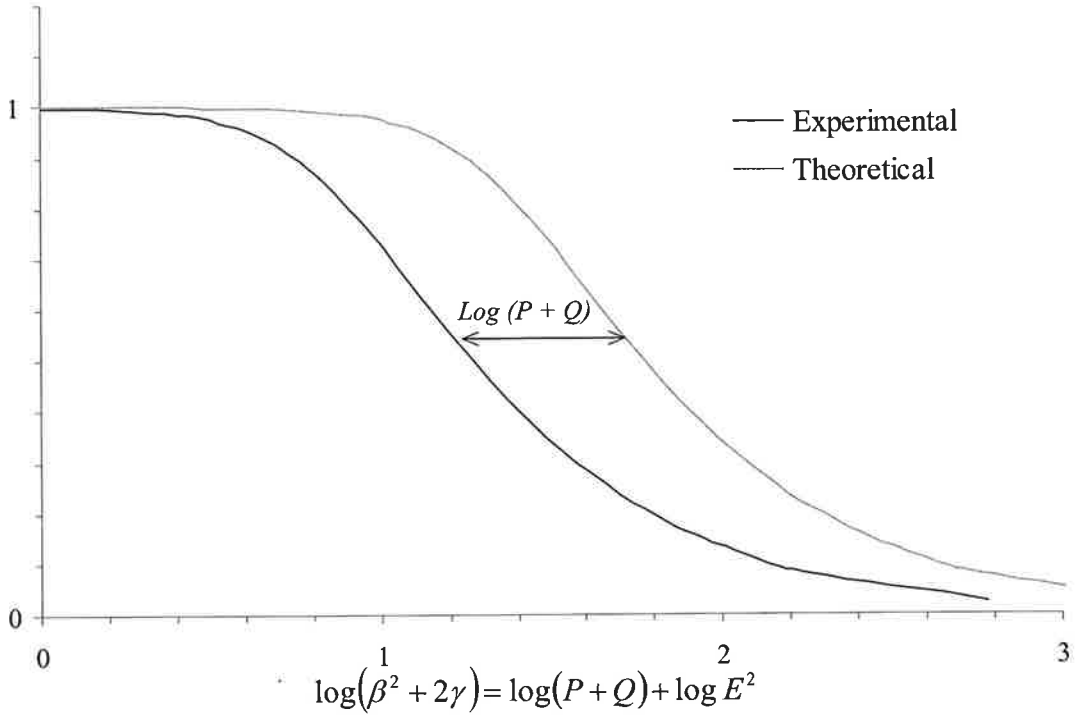

Figure 4.4: The horizontal shift imposed on an experimental curve so that it matches its theoretical representation. In this case a shift of log (0.5) is needed so that the two plots match; translating into a value of $P + Q = 3.16$.

4.7. Effects of Stray Phases on Signal Amplitudes

Stray phases in the experimental setup have a marked impact on the signal amplitude Δn and hence on the values of the specific Kerr constant K_{sp}, dipole moment μ, and polarizability anisotropy $\Delta\alpha$. As an example, **Figure 4.5** shows the field dependent birefringence data for a Na-montmorillonite sample, plotted against the same data with a stray phase added that results in a change in birefringence of $\Delta n = \pm 2.95 \times 10^{-11}$ (this value is less than half of the intrinsic birefringence of the sample cell). The stray phases contribute to a constant birefringence value in Eq. **(4.25)**, hence the plots were

generated by adding the stray phase to each of the interference free data points (green) highlighted in the figure. At intermediate to high field strength this relatively small stray phase has little effect on the curve, as it diminishes at the rate of E^2. However, in the low field limit where $E \rightarrow 0$, the contribution of the stray phase is no longer negligible.

The impact of stray phases on the analysis of the experimental results is the most severe when plots of **Figure 4.2** are generated, as shown in the inset of **Figure 4.5**. This is because the experimental birefringence is normalized to the field free extrapolate; which is essentially the stray phase! Thus, the addition of a positive birefringence (blue curve) to the low field response will effectively push the curve down once it is normalized to an artificially high value. The opposite is then true for the addition of a negative residual phase, which can be seen to create a larger peak in the pink curve. In this case, the discussion of **Section 4.3** becomes erroneous, and the rise of the blue plot above unity is no longer representative of an alignment process driven primarily by an induced-dipole moment. Similarly, an erroneous conclusion of a permanent-dipole moment driven process will be obtained when the stray phase is positive and the curve is pushed below unity.

At intermediate fields, the effect of the stray field is more quantitative than qualitative; i. e., it only affects the slope of the linear portion. Since the range of slopes is limited to -.53 and -1.13, any slope outside this range would be a good indicator of experimental artifacts.

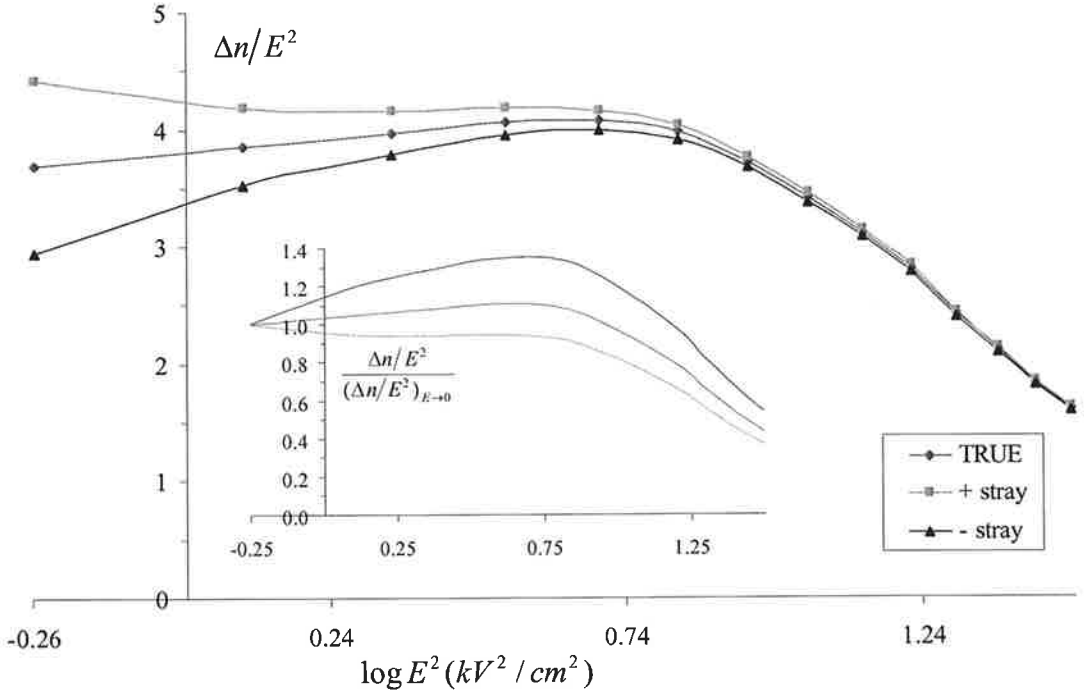

Figure 4.5: Influence of residual phases on a normalized plot of $\Delta n/E^2$ as a function of *log* E^2.

4.8. Field Dependence of the Rise Time

When an electric field is applied to a solution containing anisotropic particles, the permanent and induced-dipole will align in the direction of the field. In this section the field dependence of the rise time for the alignment will be calculated. The following treatment was derived by Dr. Evans using vector notations. The single particle potential energy is given as follows:

$$U = -\mu \cdot E - \frac{1}{2} E \cdot \alpha \cdot E \qquad \textbf{(4.31)}$$

$$\mu = \mathbf{e}d_{II} + \mathbf{e}_{\theta}d_{\perp} \tag{4.32}$$

$$E \cdot \alpha \cdot E = \frac{(2\alpha_{II} + \alpha_{\perp})}{3} E^2 + \frac{2(\alpha_{II} - \alpha_{\perp})}{3} E^2 P_2(\mathbf{e} \cdot \mathbf{z}) \tag{4.33}$$

$$P_2(\mathbf{e} \cdot \mathbf{z}) = \frac{3\cos^2 - 1}{2} \tag{4.34}$$

The unit vector ***e*** in the molecular frame points along the unique axis of the particle (rod or plate), with the unit vector e_θ being perpendicular to ***e***. The electric field is directed along the lab-fixed *z* axis and the angular distribution function *f(e,t)* is the probability distribution function *f(θ)* discussed earlier, expressed now in vector form with the following property:

$$\int f(\mathbf{e},t)d\mathbf{e} = 1 \tag{4.35}$$

where $d\mathbf{e} = \frac{1}{4\pi} \sin\theta d\theta d\phi$

and $\langle P_2(t) \rangle = \int P_2(\mathbf{e} \cdot \mathbf{z}) f(\mathbf{e},t) d\mathbf{e}$ **(4.36)**

If the particle exists with a dipole along its principal **e** axis, the inversion symmetry is broken and both odd and even rank harmonics will contribute to *f(**e**,t)*. This case will be avoided and so only particles with a dipole orthogonal to **e** will be considered; the consequence of which increases the alignment produced by the polarizability alone. The perpendicular component of μ has the property that $\mathbf{e}_\theta d_\perp$ is independent of the transformation $\theta \rightarrow \pi - \theta$, as does the P_2 function. Thus, only alignment is treated and

there is no dependence on particle orientation so that both $\mathbf{e}_0 d_\perp$ and P_2 are even in $x = cos\ (\theta)$, which allows $f(\mathbf{e},t)$ to be expressed as an even order Legendre expansion:

$$f(\mathbf{e},t) = 1 + \sum_{\ell} (4\ell + 1)\langle P_{2\ell}(t)\rangle P_{2\ell}(\mathbf{e}\cdot\mathbf{z}) \qquad \textbf{(4.37)}$$

Because the particle's radius is much larger than that of the solvent, it also undergoes Brownian motion which can be described by a diffusion/Smoluchowski approximation as follows:

$$d_t f(\mathbf{e},t) = iJ \cdot D_R \cdot [iJ - \beta\mathsf{T}] f(\mathbf{e}\cdot t) \qquad \textbf{(4.38)}$$

Where T is the torque experienced by the particle, D_R is the rotational diffusion coefficient discussed earlier and, in the context of this discussion, is defined as:

$$D_R = D_{//}\mathbf{ee} + D_\perp(1 - \mathbf{ee}) = D_\perp 1 + (D_{//} - D_\perp)\mathbf{ee} \qquad \textbf{(4.39)}$$

$iJ = \mathbf{e}\times\nabla_{\mathbf{e}}$ and is the classical rotation operator in the molecule-fixed frame (a projection of the gradient operator in the spherical coordinate perpendicular to **e**), and $\beta = 1/(k_B T)$. Once the particle is subjected to an externally applied field, it experiences a torque which is represented by:

$$\beta\mathsf{T} = -iJ\beta U \qquad \textbf{(4.40)}$$

where $$\beta U \cong -j_\perp \mathbf{e}_0 \cdot \mathbf{z} - \sigma P_2(\mathbf{e}\cdot\mathbf{z}) \qquad \textbf{(4.41)}$$

and $$j_\perp = \beta d_\perp E,\ \sigma = \frac{1}{3}\beta(\alpha_{//} - \alpha_\perp)E^2 \qquad \textbf{(4.42)}$$

Multiplying the rotational diffusion equation by $P_n(\mathbf{e}\cdot\mathbf{z})$ and integrating by parts over **e** several times then gives:

$$d_t\langle P_n(t)\rangle = -n(n+1)D_\perp\langle P_n(t)\rangle + D_\perp S_n(t) \tag{4.43}$$

Where $$S_n(t) = \frac{1}{D_\perp}\int iJP_n(\mathbf{e}\cdot\mathbf{z})\cdot D_R\cdot\beta Tf(\mathbf{e},t)d\mathbf{e} \tag{4.44}$$

The reader may notice the replacement of D_R with $D_\perp$, which results from the rotation around **e** not changing the orientation of the particle, thus the component of D_R along **e** does not contribute to the streaming or source term. Using recurrence relations of the Legendre polynomials:

$$S_n(t) = 3\sigma\left(a_n\langle P_n(\mathbf{e},t)\rangle - b_n\langle P_{n+2}(\mathbf{e},t)\rangle + \lambda_n\langle P_n(\mathbf{e},t)\rangle\right) \tag{4.45}$$

$$-j_\perp\sum_m\left(a_nI(n-2,m) - b_nI(n+2,m) + c_nI(n,m)\right)\langle P_m\mathrm{w},t)\rangle$$

where $$I(n,m) = (1/2)\int_{-1}^{1}P_m(z')P_n(z')/\sqrt{1-z'^2}\,dz' \tag{4.46}$$

and $$a_n = \frac{n(n+1)(n-1)}{4n^2-1} \tag{4.47}$$

$$b_n = \frac{n(n+1)(n+2)}{(2n+1)(2n+3)} \tag{4.48}$$

$$\lambda_n = n(n+1)\left(1 - \frac{3\sigma}{(2n-1)(2n+3)}\right) \tag{4.49}$$

The growth of $\langle P_n \rangle$ is described by Eq. **(4.44)** and its coupling to a set of even order Legendre moments is described by Eq. **(4.45)**. The leading source term (n = 2) looks as follows:

$$S_2(t) = 3\sigma\left(\frac{2}{5} + \frac{2}{7}\langle P_2\rangle - \frac{24}{35}\langle P_4\rangle\right)$$
$$-\frac{3\pi j_\perp}{16}\left(1 + \frac{1}{4}\langle P_2\rangle - \frac{17}{128}\langle P_4\rangle - \frac{13}{512}\langle P_6\rangle - \frac{16}{16384}\langle P_8\rangle + \ldots\right) \quad \textbf{(4.50)}$$

and in the low field limit:

$$d_t\langle P_2(t)\rangle = -6D_\perp\left(1 - \frac{3\sigma}{21} + \frac{\pi}{128}j_\perp\right)\langle P_2(t)\rangle + D_\perp\left(\frac{2(3\sigma)}{5} - \frac{3\pi j_\perp}{16}\right) \quad \textbf{(4.51)}$$

The ultimate goal is to be able to derive $\langle P_2(t)\rangle$ for arbitrary fields and times. In order to simply the system of equations needed to accomplish this, a reduced time $\tau = D_\perp t$ is introduced, so that:

$$d_\tau\langle P_n(\tau)\rangle = -\lambda_n\langle P_n(\tau)\rangle + a_n\langle P_{n-2}(\tau)\rangle - b_n\langle P_{n+2}(\tau)\rangle \quad \textbf{(4.52)}$$

The differential equation represented by Eq. **(4.52)** can be solved using the Laplace time transform. This mathematical technique is commonly used to produce an easily solvable algebraic equation from a differential equation using, in this case

$$\langle P_n(s)\rangle = L\left(P_n(\tau)\right) = \int_0^\infty e^{-s\tau}P_n(\tau)d\tau \quad \textbf{(4.53)}$$

Thus, solving for n = 2, subject to an isotropic initial condition, gives:

$$\langle P_2(s)\rangle = \frac{a_2}{s+\lambda_2 + b_2\left(P_4(s)/P_2(s)\right)} \tag{4.54}$$

Then

$$\langle P_4(s)/P_2(s)\rangle = \frac{a_4}{s+\lambda_4 + b_4\left(P_6(s)/P_4(s)\right)} \tag{4.55}$$

$$\langle P_6(s)/P_4(s)\rangle = \frac{a_6}{s+\lambda_6 + b_6\left(P_8(s)/P_6(s)\right)} \tag{4.56}$$

so that

$$\langle P_2(s)\rangle = \cfrac{a_2}{s+\lambda_2 + b_2 \cfrac{a_4}{s+\lambda_4 + b_4 \cfrac{a_6}{s+\lambda_6 + b_6 \cfrac{P_8(s)}{P_6(s)}}}} \tag{4.57}$$

Eventually, the difference between the ratios of order parameters in the non-terminating, continued fraction expressed by Eq. **(4.57)** will become small enough that the equation can be solved self consistently as such:

$$\langle P_{n+2}(s)/P_n(s)\rangle \cong \frac{a_n}{s+\lambda_n + b_n\left(P_{n+2}(s)/P_n(s)\right)} \tag{4.58}$$

and in doing so:

$$P_{n+2}(s)/P_n(s) \cong \frac{\sqrt{(s+\lambda_n)^2 + 4a_n b_n} - (s+\lambda_n)}{2b_n} \tag{4.59}$$

Thus, the continued fraction can represent the infinite time limit attained by a system which is initially isotropic. The following section will address the solution for $\langle P_2(t)\rangle$

in the low field cases where $E \rightarrow 0$. An overview of how the theory can be used to analyze the rise curves and calculate the anisotropy in the polarizability will be given.

4.8.1. Alignment at Low Fields where E → 0

In this case, the differential equation represented by Eq. **(4.43)** will be solved by neglecting the coupling of $\langle P_2 \rangle$ to higher harmonics. Thus:

$$d_r \langle P_2(\mathbf{e},t) \rangle = -\lambda_2 \langle P_2(\mathbf{e},t) \rangle + a_2 \qquad \textbf{(4.60)}$$

Given an initial alignment of $\langle P_2(\mathbf{e},t=0) \rangle$, the solution is:

$$\langle P_2(\mathbf{e},\tau) \rangle = \frac{a_2}{\lambda_2}\left(1 - e^{-\lambda_2 \tau}\right) + e^{-\lambda_2 \tau} \langle P_2(\mathbf{e},t=0) \rangle \qquad \textbf{(4.61)}$$

Where $$\lambda_2 = 6\left(1 - \frac{\sigma}{7}\right), \text{ and } a_2 = \frac{6}{5}\sigma \qquad \textbf{(4.62)}$$

In weak fields, for a fluid with no alignment:

$$\langle P_2(t) \rangle \cong a_2 D_\perp t \qquad \textbf{(4.63)}$$

Thus, by determining the slope of $\langle P_2(t) \rangle$ in its low field limit where $E \rightarrow 0$, the anisotropy in the polarizability $\Delta\alpha$ can be found (by way of a_2), if the rotational diffusion coefficient D_R is known. An example of how this is done graphically and mathematically is given in **Figure 4.6**.

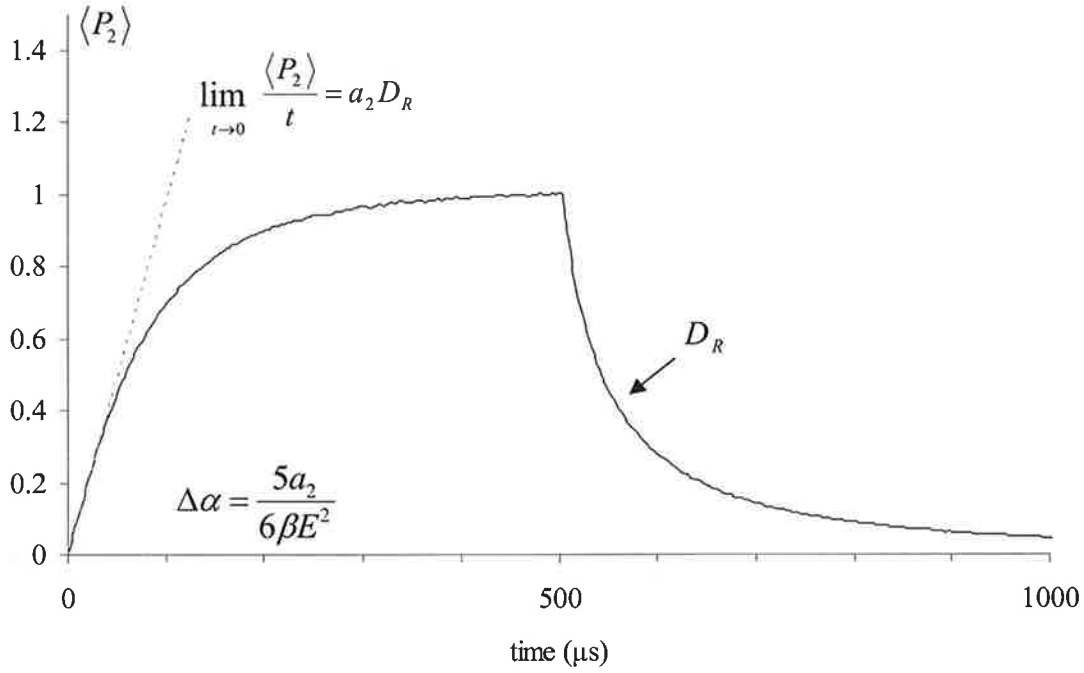

Figure 4.6: The various physical parameters which can be derived from the rise and decay of the birefringence curve.

In this particular case, the $\langle P_2(t) \rangle$ curve is created by dividing the acquired alignment curve by the saturation value of the birefringence at infinite field as follows:

$$\langle P_2(t) \rangle = \frac{V(t)}{V_{E\to\infty}} \qquad \textbf{(4.64)}$$

where V is the voltage reading from the oscilloscope. However, this method only works if the value of $V_{E\to\infty}$ is known. In the event that it is not, another fitting method can be used which determines $\langle P_2(t) \rangle$ based on the saturation value of the birefringence curve. In this case, the ratio is taken as:

$$\langle P_2(t) \rangle = \frac{V(t)}{V_{t\to\infty}} \qquad \textbf{(4.65)}$$

where the denominator is now based on the asymptotic behavior of the curve at infinite time instead of infinite field. The subsequent curve is subject to the same fitting procedure outlined in Figure 4.6; the difference being that the value a_2 is replaced with λ_2 from Eq. **(4.62)**.

,4.9. Field Free Relaxation

The birefringence of a solution will increase to a steady-state value upon application of an external field due to particle alignment in the field. Here we consider the response of the particles when the field is suddenly removed and the aligned particles return to random orientation, causing the birefringence to fall asymptotically to zero. **Figure 4.7** shows the typical change of the birefringence upon application and removal of an alignment field.

In this study, we will limit our discussion to rigid bodies that are much larger than individual solvent molecules. Under this assumption, the theory of Brownian motion applies. The three elements of theory needed to describe the variation in birefringence of a suspension following removal of an orienting field are:

1. A theory which relates the observed birefringence to the orientational distribution of the particle in a suspension.

2. A theory of Brownian motion applicable to the shape class of the particle, which relates the orientational relaxation to the macroscopic diffusion constant.
3. An expression for the diffusion constant which relates to the shape and size parameters of the particle.

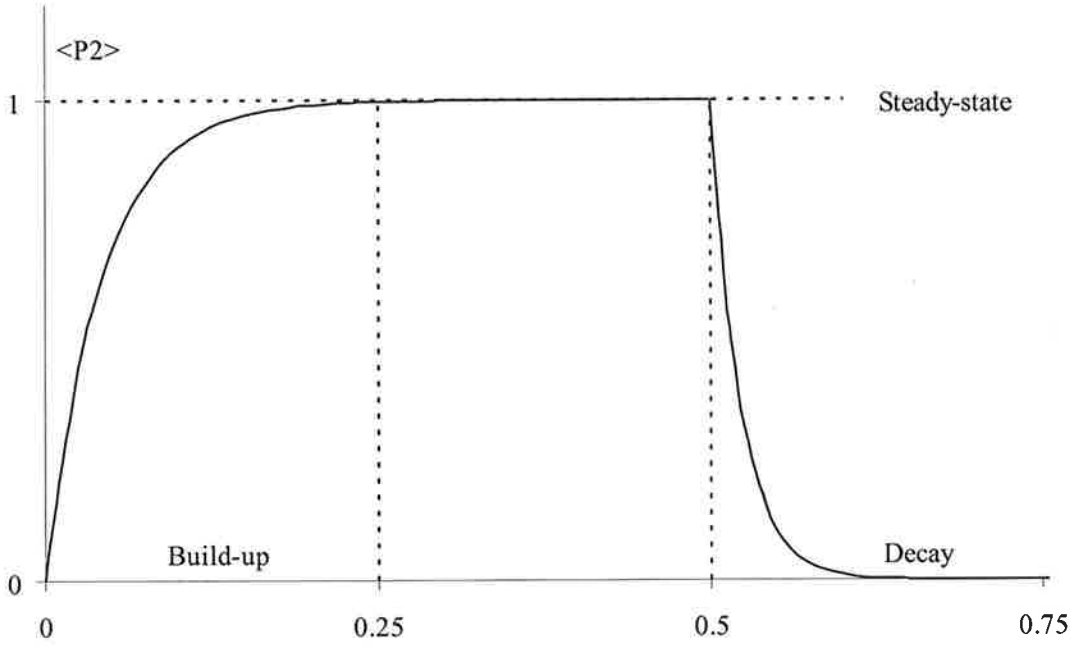

Figure 4.7: Typical birefringent response curve observed from a TEB experiment. Three distinct parts are observed; build-up, steady-state, and decay. Molecular dimension can be determined directly from the decay.

The relaxation process is representative of the particle's geometric parameters via the rotational diffusion coefficient D_R. In the following discussion we will again use $f(\theta)d\theta$ to represent the number of particles per unit volume having their orientation angle between θ and $\theta + d\theta$, where θ is defined as the polar angle between the

orientation field and the symmetry axis of the particle. During the decay process, the number of particles with orientation angles passing between θ and $\theta + d\theta$ is given by $J(\theta)$:

$$J(\theta) = -D_R\left[\frac{\partial f(\theta)}{\partial \theta}\right] \tag{4.66}$$

where the rotational diffusion coefficient is related to the molecular parameters, the viscosity of the solvent η, and the thermal energy k_BT.

For revolution ellipsoids,[5]

$$D_R = \frac{3k_BT}{16\pi\eta L^3}\left[2\ln\left(\frac{2L}{a}\right) - 1\right] \tag{4.67}$$

where a is the short axis, and L is the long axis of the molecule. For a long rod,[6]

$$D_R = \frac{3k_BT}{8\pi\eta L^3}\left[\ln\left(\frac{2L}{a}\right) - .8\right] \tag{4.68}$$

where L is the length and a is the diameter. For a prolate ellipsoid (disk) with two radii of a and one radius of c,[7]

$$D_R \cong \frac{k_BT}{8\pi\eta a^3}, \text{ as c/a} \rightarrow 0 \tag{4.69}$$

The diffusion equation for the field free relaxation process has been established and solved by Benoit.[8-10] The change in birefringence is represented as a single exponential decay function:

$$\Delta n_t = \Delta n_o e^{-6D_R t} \tag{4.70}$$

where Δn_t is the birefringence at time t after removal of the field, and Δn_o is the birefringence of the initial state. Knowing the temperature and viscosity, the curve represented by Eq. **(4.70)** can be used to determine the size and shape of the particles.

Almost all studies on the transient birefringence of solutions have employed the carefully elaborated treatment of Benoit for the rotational diffusion of a spheroid possessing optical, electric, and geometric symmetry about a primary axis. Yet, in many of the reports, the decay fittings were best accomplished using the following biexponential function:

$$\frac{\Delta n_t}{\Delta n_o} = \left(B_1 e^{-6D_R^+ t} + B_2 e^{-6D_R^- t}\right) \tag{4.71}$$

where the coefficients B_1 and B_2 are unitless quantities. In each case, the observed result was attributed to polydispersity in the sample. However, by definition, polydispersity implies a "broad" range of sizes, shapes and mass characteristics. Therefore, it would seem to be an oversimplification to attribute the fitting of two distinct decay constants to polydispersity.

One possible explanation of the deviation from Benoit's model might be related to its assumption of symmetric spheroids. Thus asymmetric ellipsoids are excluded, including those with three unique axes, those with permanent dipole moments of non-axial orientation, and those with intrinsic biaxial birefringence. The rotational symmetry about one of the axies of a spheroid particle dictates that no

orientation mechanism can produce a distribution with a dependence on more than one single angle θ.

Ridgeway expanded on Benoit's theory and treated the case of particles containing three unique axes.[11, 12] In his treatment, Ridgeway defines a symmetric diffusion tensor that may be diagonalized to define three orthogonal particle axes corresponding to three principal diffusion constants. In the case of ellipsoids, these axes coincide with the geometric axes. The resulting expression for the decrease in birefringence of asymmetric ellipsoids becomes a biexponential function involving two rotational diffusion coefficients D_R(fast) and D_R(slow), and the pre-exponential coefficients are determined by the shape of the ellipsoid. Moreover, Ridgeway also showed that one of the pre-exponential coefficients of the biexponential model vanishes in the case of a spheroid or axi-symmetric particle.

Interestingly, even though Ridgeway's treatment for the decay of particle alignment is more general, it has seen very limited use. This will be evident later when comparisons are made between the particle dimensions determined in the current research and those from other groups. It should be mentioned that the oversight of Ridgeway's model does not appear to be intentional, nor does it stem from an apparent problem with the theory. Instead, its limited application seems to arise from an oversimplification on certain systems, which are assumed to be axisymmetric, in which case Ridgeway's model does not apply. However, outside the scope of rigid, seemingly axisymmetric particles, the model has been used in the characterization of protein hydrodynamics.[13-15] The present investigation will approach the analysis of

birefringence decay using the model of the asymmetric ellipsoid, and it will be seen that the model explains the results better than that of Benoit.

4.10. Frequency Dependence of the Birefringence

The response of birefringence to an oscillatory electric pulse offers another method for the determination of relaxation time τ and provides insight into the electric birefringence. Moreover, it gives information concerning the induced and permanent dipole contributions. For this treatment, the field can be written as:

$$E = E_o \sin \omega t \tag{4.72}$$

where E_o is the maximum amplitude and ω is the circular frequency of the field. We will start by looking at the response of the induced dipole and assume that the birefringence follows the Kerr law. In addition, we will also assume that the period of the alternating field is large compared with the relaxation time of induced birefringence. In the case of a pure induced dipole moment, the birefringence takes the value:[16]

$$\Delta n = \Delta n_{ave}\left[1 \pm \frac{\cos(2\omega t - \varphi)}{(1+4\omega^2\tau^2)^{1/2}}\right] \tag{4.73}$$

where Δn_{ave} is the average value of Δn. Eq. **(4.73)** shows that the birefringence consists of two components, one which is constant with time (Δn_{ave}) and another

which alternates with twice the frequency of the applied field and differs in phase with the latter by the angle φ. The extreme values of Δn are then given by:

$$\Delta n_o = \Delta n_{ave}\left[1 \pm \frac{1}{(1+4\omega^2\tau^2)^{1/2}}\right] \qquad \textbf{(4.74)}$$

Eq. **(4.74)** shows that at sufficiently high frequencies a steady birefringence is obtained and the average value is equal to the birefringence which would be observed if the sample was subjected to a DC field Δn_o.

In the general case, with the presence of both the induced and permanent dipoles, the variation of the birefringence with frequency involves the ratio of *P/Q*. The relationship has been given by Thurston and Bowling,[17] where the steady-state component of the birefringence Δn_{ave} is written as:

$$\Delta n_{ave} = \frac{\Delta n_M}{1+P/Q}\left[1+\frac{P/Q}{1+(\omega/2D_R)^2}\right] \qquad \textbf{(4.75)}$$

From which we get:

$$\lim_{\omega\to\infty} \Delta n_{ave} = \frac{\Delta n_M}{1+P/Q} \qquad \textbf{(4.75)}$$

In this case, the value of Δn_M is representative of the birefringence observed upon application of a DC field or low frequency AC field, if saturation is able to be achieved in the later case. Eq. **(4.75)** shows that as the ratio *P/Q* approaches infinity, the steady state value of Δn_{ave} at high frequency approaches zero. In contrast, as the

ratio approaches zero, Eq. **(4.75)** reduces to Eq. **(4.74)** and the steady states at low and high frequency are equal.

The above relations give a convenient, quantitative method for checking the presence of the permanent dipole and polarizability anisotropy for a particle, provided that a steady state in the birefringence can be reached. Unfortunately, the application of constant AC resulted in current effects that heated the samples. This limited the trials to pulsed AC fields with durations of no more than 500 μs. A consequence of the limited pulse durations was the inability to reach a steady state in the birefringence for all for all but the quantum dot samples. However, a qualitative assessment can and will be applied to the clay and cellulose crystals, where we will look at the general response of the samples as the frequency of the field is increased from 2 to 200 kHz.

4.11. References

1. Born, M. and E. Wolf, *Principles of Optics: Electromagnetic Theory of Propagation, Interference and Diffraction of Light*. 7th ed. 1999, Cambridge: Cambridge University Press.

2. Shah, M.J., *ELECTRIC BIREFRINGENCE OF BENTONITE. II. AN EXTENSION OF SATURATION BIREFRINGENCE THEORY.* Journal of Physical Chemistry, 1963. **67**(10): p. 2215-2219.

3. Eigen, M. and G. Schwarz, *An orientation field effect of the electric conductivity in polyelectrolyte solutions.* Zeitschrift fuer Physikalische Chemie (Muenchen, Germany), 1955. **4**: p. 380-5.

4. O'Konski, C.T., K. Yoshioka, and W. Orttung, *Electric Properties of Macromolecules. IV. Determination of Electric and Optical Parameters from Saturation of Electric Birefringence in Solutions.* Electric Properties of Macromolecules, 1959. **63**: p. 1558-1565.

5. Fredericq, E. and C. Houssier, *Electric Dichroism and Electric Birefringence*. 1973, Clarendon: Oxford.

6. Elias, J.G. and D. Eden, *Transient electric birefringence study of the length and stiffness of short DNA restriction fragments.* Biopolymers, 1981. **20**(11): p. 2369-80.

7. Evans, G., *Alignment of Axially Symmetric Molecules Induced by Electric Fields*. 2008, Oregon State University: Corvallis. p. 8.

8. Benoit, H., *Electric birefringence of thymonucleic acid.* Journal de Chimie Physique et de Physico-Chimie Biologique, 1951. **48**: p. 612-14.

9. Benoit, H., *The Kerr effect demonstrated by dilute solutions of rigid macromolecules.* Ann. phys., 1951. **6**: p. 561-609.

10. Horn, P., H. Benoit, and G. Oster, *Light scattered by very dilute solutions of optically anisotropic rods.* Journal de Chimie Physique et de Physico-Chimie Biologique, 1951. **48**: p. 530-5.

11. Ridgeway, D., *Transient Electric Birefringence of Suspensions of Asymmetric Ellipsoids.* Journal of the American Chemical Society, 1966. **88**(6): p. 1104-1112.

12. Ridgeway, D., *Estimation of particle dimensions from the relaxation of transient electric birefringence of suspensions.* Journal of the American Chemical Society, 1968. **90**(1): p. 18-22.

13. Umazano, J.P. and J.A. Bertolotto, *Optical Properties of DNA in Aqueous Solution.* J. Biol. Phys. FIELD Full Journal Title:Journal of Biological Physics, 2008. **34**(1-2): p. 163-177.

14. Harding, S.E., *Protein hydrodynamics.* Protein (Stamford, Conn.) FIELD Full Journal Title:Protein (Stamford, Connecticut), 1999. **2**: p. 271-305.

15. Khlebtsov, N.G., A.G. Melnikov, and V.A. Bogatyrev, *Relaxation optic phenomena in polydisperse suspensions and determination of particle sizes using transmitted light parameters.* Colloids Surf., A FIELD Full Journal Title:Colloids and Surfaces, A: Physicochemical and Engineering Aspects, 1999. **148**(1-2): p. 17-28.

16. O'Konski, C.T. and A.J. Haltner, *Characterization of the monomer and dimer of tobacco-mosaic virus by transient electric birefringence.* J. Am. Chem. Soc. FIELD Full Journal Title:Journal of the American Chemical Society, 1956. **78**: p. 3604-10.

17. Thurston, G.B. and D.I. Bowling, *The Frequency Dependence of the Kerr Effect for Suspensions of Rigid Particles.* Journal of Colloid and Interface Science, 1969. **30**(1): p. 34-45.

5. Na-Montmorillonite

5.1. Introduction

Clay particles have basic structural units consisting of silica tetrahedrons and alumina octahedrons. The basic units then combine, forming different shapes including bars, plates, and sheets. **Figure 5.1** shows the basic units and a sheet structure:

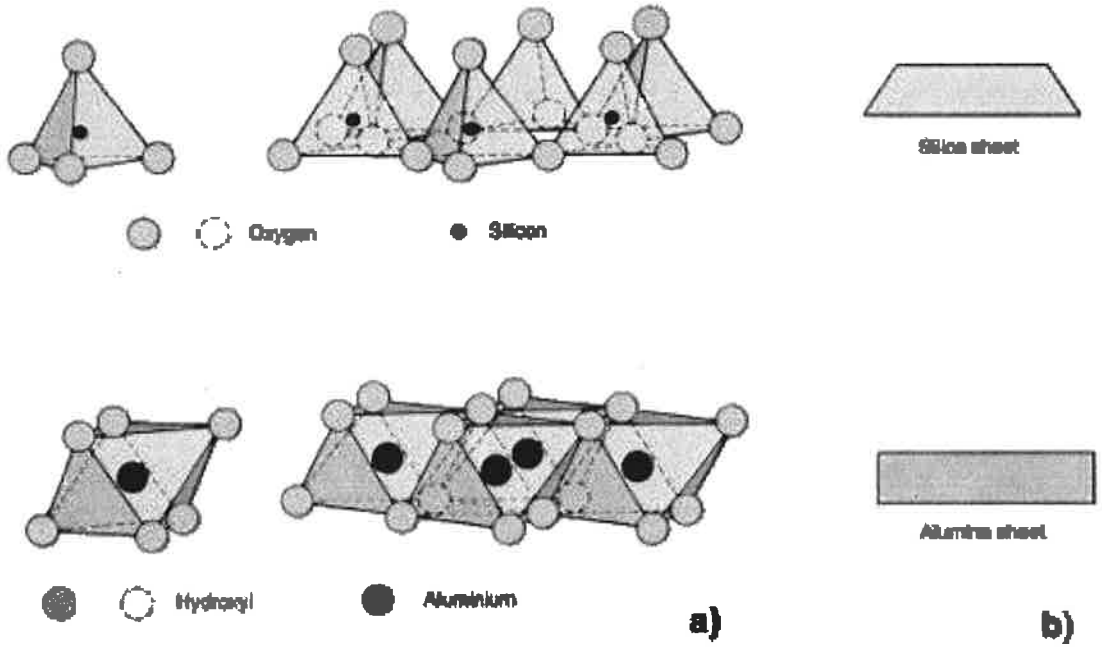

Figure 5.1: Basic units of clay minerals and the silica and alumina sheets which they form.

A large number of electric charges remain unbalanced in these sheets alone, thus, cations and water molecules are necessary to satisfy the unbalanced electric charges; creating bonds and joining the sheets together. For this reason, clay minerals are formed by the stacking of basic sheet structures with different forms of bonding between the combined sheets. Such structures of the clay minerals are represented in

Figure 5.2.[1] In solutions, the negative unbalanced electric charges on the outer edges around the clay particles are solvated by water molecules and cations. The mobility of the cations along the surface of the clay platelet contributes to the interfacial polarizability α_i discussed previously.

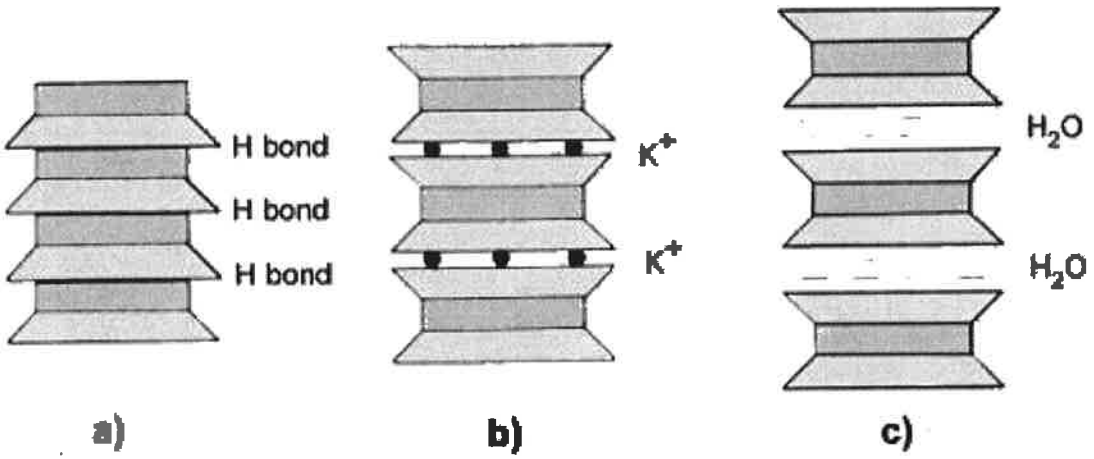

Figure 5.2: Structure of the main clay minerals: (a) kaolinite, (b) illite and (c) montmorillonite, based on combined sheets.

5.2. Analysis Overview

A great deal of effort has been devoted to the study of clay solutions to elucidate the ion-water atmosphere, i. e., the "double layer." However, at the present time, the properties of the double layer and its influences on the aggregation of clay particles are only partially understood. In this work, we will investigate the electrical properties of clay solutions and its alignment mechanism in an electric field. The analysis of the clay samples will be separated into four parts. The following section outlines each

analytical technique, the physical property it depends on, and how that property will be used to characterize the sample:

1) **Concentration dependence of the decay mechanism** will be followed in order to determine the sample's percolation threshold. The definition of percolation is the concentration at which finite connectivity between particles begins. In this current context, however, we loosely define it to be the concentration that exhibits observable interparticle interactions. It has been generally accepted that inter-particle interactions at concentrations above the percolation threshold can lead to unusual birefringence behaviors. In the case of aqueous clay samples, inter-particle interactions can lead to aggregation of the platelets, which can then lead to large changes in the permanent and induced-dipole of the sample. Thus, for the purpose of this research, results were obtained only for dilute solutions so to minimize the inter-particle interactions. Once a suitable concentration range has been established, the rotational diffusion coefficient D_R will be calculated from the decay constants and used to determine particle dimensions.
2) **Saturation of the birefringent response** Δn will be studied by plotting its value against varying functions of E^2 and using features such as the slope, local maximum, and y-intercept to determine the following:
   - Optical anisotropy Δg
   - Specific Kerr constant K_{sp}

- Orientation mechanism i.e. the ratio of permanent to induced-dipole moment
- Single particle polarizability anisotropy $\Delta\alpha$

3) **Field dependence of the rise time** will be followed to elucidate the orientation mechanism (induced-dipole and/or permanent-dipole). The rise times in the low field limit will also be used (along with the rotational diffusion coefficient from section 1) to calculate single particle polarizability anisotropies. The results will then be compared with the values obtained from the analysis of section 2.
4) **Pulsed AC trials** will be conducted as a supplemental study to further confirm the alignment mechanism.

5.3. Experimental

Sodium salt modified natural montmorillonite (Cloisite® NA^+ Nanoclay) was used as supplied by Southern Clay Products; the specifics of which are outlined in **Table 5.1**. Approximately 100.0 mg of Cloisite® NA^+ Nanoclay was added to 500.0 ml of deionized water and ultrasonicated for ten minutes in order to adequately separate the platelets. The suspension was left to stand for 24 hours and then filtered through a 2 μm ceramic filter. The concentration of the subsequent stock solution was determined to be 41 μg/ml by evaporation of a known volume of solution to dry weight. Sample solutions were prepared from the stock solution by the direct addition of Millipore deionized water.

Table 5.1: Specific physical properties of the Na-Montmorillonite sample supplied by Southern Clay Products.

Specific gravity	Bulk density (g/cm^3)	Particle size (μm)
1.77	.199 loose	≤ 2.00 μm 10%
	.335 packed	≤ 6.00 μm 50%
		≤ 13.00 μm 90%

5.4. Concentration Dependence of D_R

As was stated previously, the purpose of the concentration trials is to determine the percolation threshold. With increasing concentration, the inter-particle distance will get smaller and interactions will occur due to the limited space. With increasing field strength the packing or arrangement order within the system will also increase. Thus, its response upon removal of the applied field becomes sensitive to the local fields of the particles as surface-to-surface interactions are maximized.

A simple method for determining a threshold concentration is to follow the diffusion as a function of the alignment field and concentration. If inter-particle interactions are present, both factors will have an observable effect on D_R. The measurements taken in this research were restricted to field strengths between .02 and 3.7 kV/cm due to equipment limitations and thermal effects of the sample. Field strength trials were run on clay samples ranging from 20 μg/ml down to 1.25 μg/ml. In each case the decay curves were fit using the double exponential expression represented by Eq. **(4.71)**. The results for a fast and slow rotational diffusion

coefficient D_R as a function of field strength can be seen in **Figures 5.3 & 5.4** respectively.

The two values for the rotational diffusion coefficient are separated by one order of magnitude with unitless amplitudes of .65 and .35 for D_R(fast) and D_R(slow), respectively. The observation of two coefficients is consistent with literature reports of bi-exponential decay,[2-5] which has been attributed to polydispersity by previous groups. In this study, the existence of two distinct rotational diffusion coefficients is considered to be a result of the particles having three unique axies; best modeled as asymmetric ellipsoids. As such, their decays are best fit to a biexponential function, which accounts for the two unique axies orthogonal to the symmetry axis of the particles. This approach was covered in detail in **Section 4.9** on field free decay of the birefringence.

The variations in Figures 5.3 & 5.4 for both the fast and slow rotational diffusion coefficients are similar. In both cases a steady increase in the value of D_R occurs for the concentration of 10 μg/ml and above; whereas at lower concentrations, it is essentially constant. This suggests that any concentration at or below 5 ug/ml should be free of inter-particle interactions.

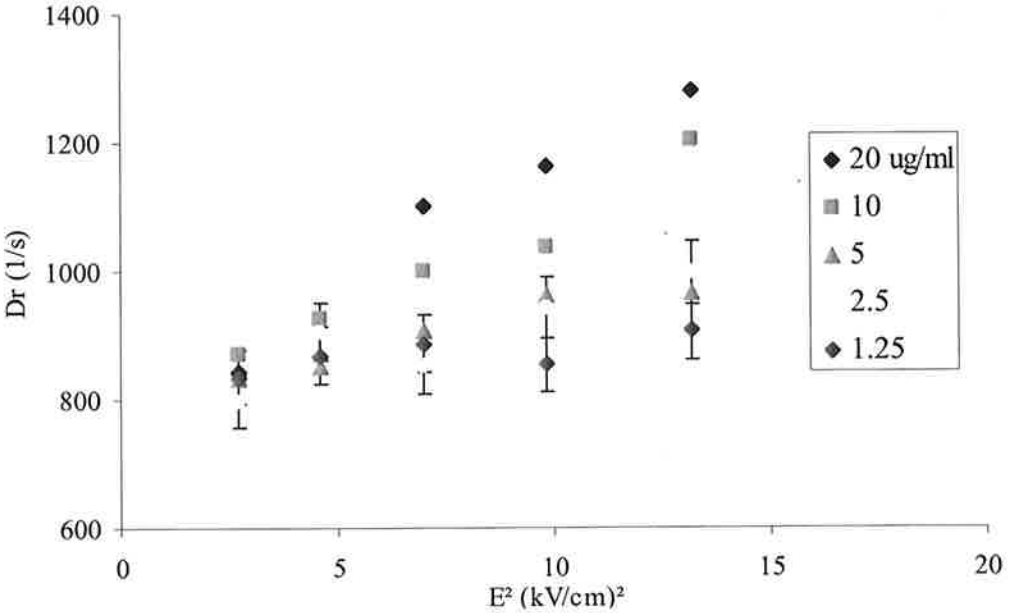

Figure 5.3: "Fast" rotational diffusion coefficients D_R for Cloisite ® NA^+ at vary concentrations as a function of the squared field strength.

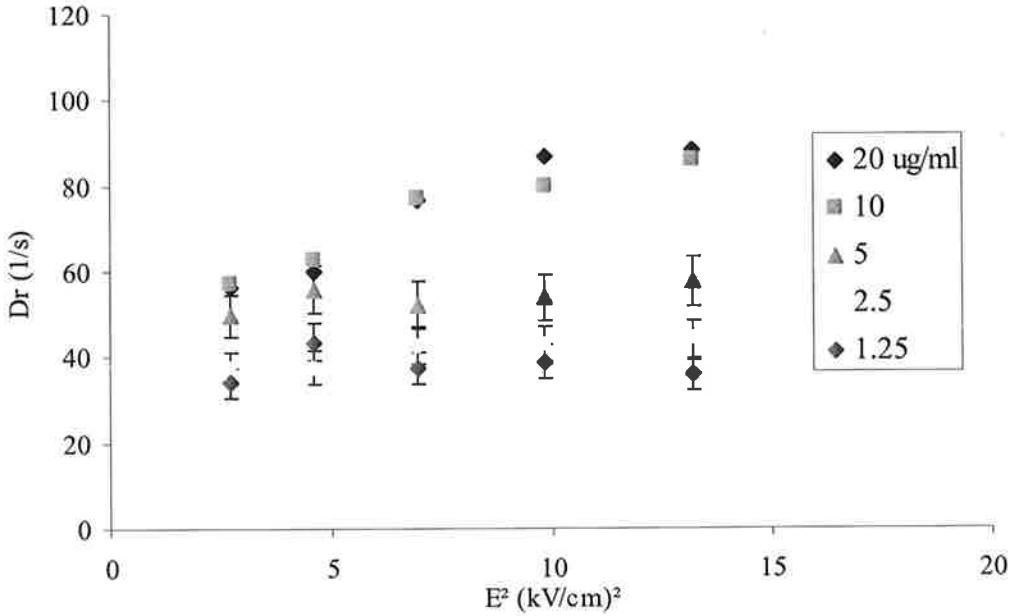

Figure 5.4: "Slow" rotational diffusion coefficients D_R for Cloisite® NA^+ at vary concentrations as a function the squared field strength.

With a percolation threshold determined, the rotational diffusion coefficient and shape parameters can now be calculated. At present, there is no theoretical formula to treat a rectangular sheet while the formulas for ellipsoids, rods and disks are given by Eqs. **(4.67)**, **(4.68)** and **(4.69)** respectively. **Table 5.2** gives the results for the disk and rod models, assuming a thickness of 1 nm for disks and a length to diameter ratio of $L/a = 10^3$ for rods. These assumptions are generally accepted for montmorillonite platelets based on conversations with Dr. Lerner, the resident expert on nanoclays at OSU.

Table 5.2: Values for the rotational diffusion D_R coefficient and diameter for Cloisite 20A® platelets at varying fields and concentrations below the percolation

Concentration (μg/mL)	D_R (s^{-1})		disk diameter (nm)		rod length (nm)	
	fast	slow	fast	slow	fast	slow
5.00	904 ± 61	54 ± 3	95 ± 2	242 ± 5	310 ± 7	794 ± 15
2.50	899 ± 78	41 ± 3	95 ± 3	266 ± 7	311 ± 9	871 ± 23
1.25	870 ± 28	38 ± 4	96 ± 1	272 ± 8	314 ± 3	893 ± 27
	891 ± 57	**44 ± 8**	**95 ± 2**	**260 ± 15**	**312 ± 7**	**852 ± 49**

Although the two models seem to be unrelated to each other at first glance, it is not too difficult to imagine that, as the length to width ratio of the sheet changes, the model which best represents the shape of the platelet rests somewhere between a disk and a rod. This would suggest that a more appropriate modeling of the system would result

from a combination of the two theories; one which accounts for the polydispersity in both size and shape. **Figure 5.5** shows just how polydisperse the clay sample really is, with both particle shapes observable in each of the three TEM images. The larger image on the left is comprised mostly of sheets and disks, while the two images on the right show particles which closely resemble rods. The significance of the two models, and how they are represented by the birefringent response of the sample, will be addressed in **Section 5.6**.

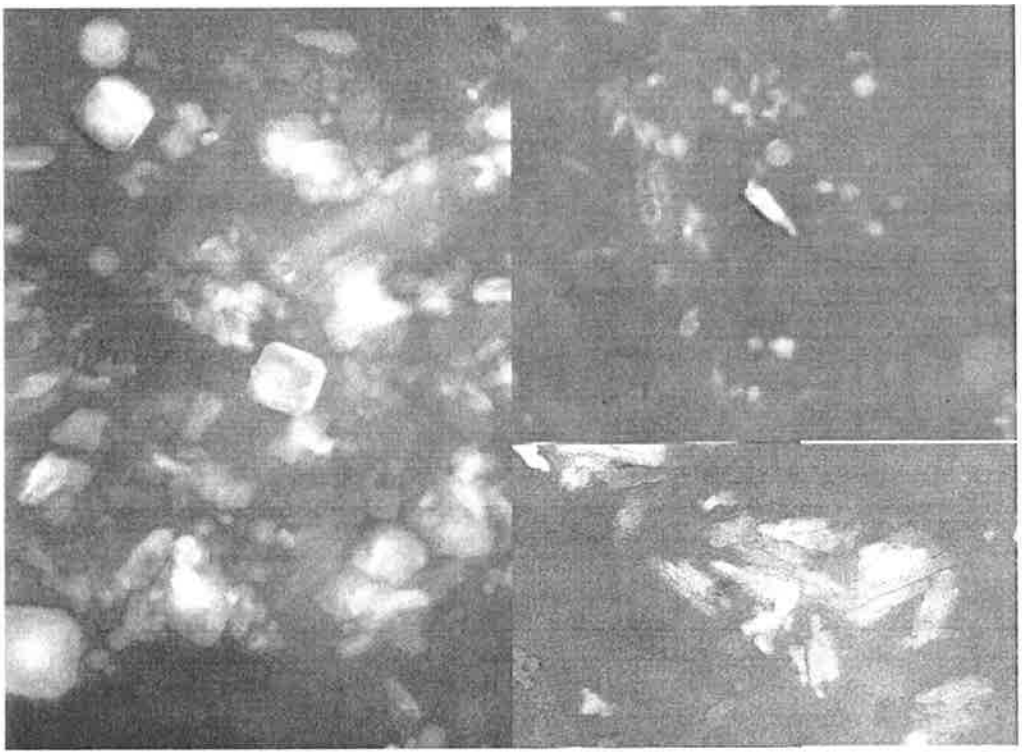

Figure 5.5: TEM images from the 41 μg/ml stock solution of Na-montmorillonite. All three images show the polydisperse nature of the sample and the existence of particles which resemble sheets, plates, and rods.

Another factor that influences the particle size is the ionic atmosphere of the solution. For example, Yariv et al reported large size variations for aqueous Na-Montmorillonite where diameters ranged from 0.8 to 10.5 μm. More importantly, the particle sizes were shown to increase as particle concentration decreased.[6] The presence of large Na-montmorillonite particles was attributed to the extensive swelling in aqueous suspensions by osmotic water adsorption. In contrast, Furukawa et al reported a wide range of particle sizes but attributed it to counter ion concentration.[7] **Figure 5.6** shows their results for the average hydrodynamic diameters (*dH*) of montmorillonite suspensions (8 μg/ml) in constantly stirred solutions containing varying concentrations of artificial seawater (ASW). The results show a particle size of $dH \approx 200$ nm in the zero salinity suspension. On the other hand, at elevated salinity values (.18 – .72%), the particles were believed to aggregate during the initial ~15 minutes following ASW mixing, reaching diameters between $dH \approx 600$ and 1100 nm.

The above two mechanisms imply that a larger particle size can be expected in solutions where clay platelet concentrations are low and/or counter ion concentrations are high, due to water adsorption and/or aggregation. Consequently, smaller particle sizes should be obtained from solutions of higher clay concentrations and/or low counter ion concentrations. Thus, the particle length range of 260 to 852 nm from the current work, which is in agreement with the results obtained by Furukawa (100 to 1300 nm), is reasonable. Here we need to take into consideration that the ionic atmosphere in our experiment was minimized by the use of Millipore water. In so doing, we have limited the electrical conductivity of the solution; and in the meantime,

we have limited the likelihood of aggregation. Furthermore, the solution was filtered down to 2 μm, effectively removing any particles that may have swelled to larger sizes due to water adsorption.

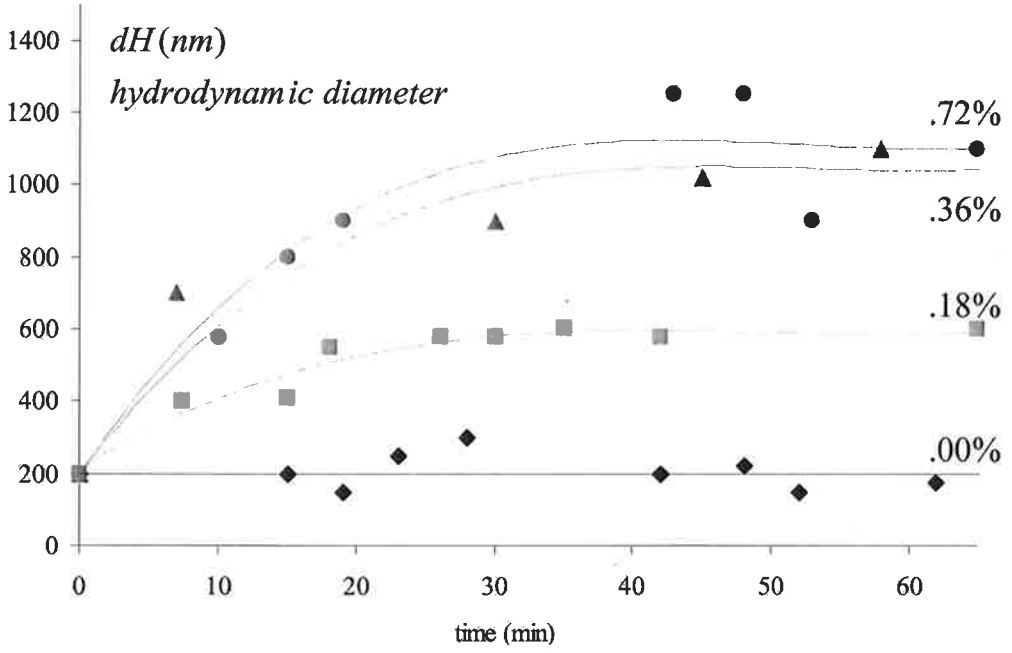

Figure 5.6: Average hydrodynamic diameters (*dH*) of montmorillonite-only suspensions (8 μg/ml), measured as a function of time after mixing with artificial seawater using dynamic light spectroscopy.

5.5. Saturation of the Birefringent Response at High Fields

The birefringent response of a 5 μg/ml clay sample at varying field strengths can be seen in **Figure 5.7**. The oscilloscope traces were recorded after averaging over 128 pulses at 2 Hz, with a pulse width of 500 μs. The change in birefringence Δn at each field strength can be calculated according to Eq. **(3.35)** for an optical arrangement with a quarter-wave plate. An example of one such calculation, for a trial run at 1.4 kV/cm, goes as follows:

$$I_\delta\,(\alpha = 0) = 1.62\ \text{V} \qquad I_\alpha\,(\alpha = 2^\circ) = 155\ \text{V}$$

$$\delta = 2\sin^{-1}\left[\left(\frac{1.62}{155}+1\right)^{1/2}\sin 2\right] - 2(2) = .021^\circ$$

$$\Delta n = \frac{\delta\lambda}{360l} = \frac{(.021)(633\times10^{-9})}{(360)(.01)}$$

$$\Delta n = \underline{\underline{3.62\times10^{-9}}}$$

In order to analyze the saturation data, it is necessary to plot the birefringence Δn as a function of the squared field strength E^2 in varying manners. For review, **Appendix B** gives a list of parameters and their descriptions. The analysis will start with a look at the intermediate to high field region and the direct calculation of the optical anisotropy factor Δg. Plots of the birefringent data will then be used to determine the ratio of permanent to induced-dipole. We will then move to the low field region with the calculation of the specific Kerr constant K_{sp}. The final step will be to bring the analysis from the two regions together with the calculation of the anisotropy in the polarizability.

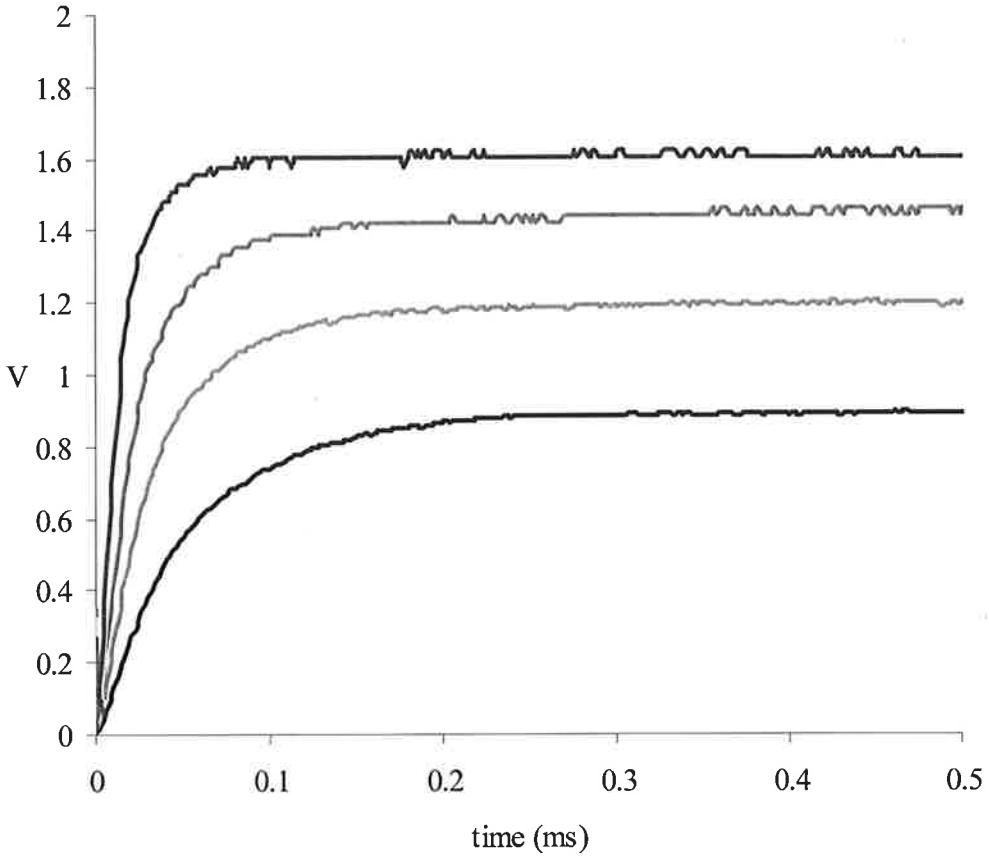

Figure 5.7: Birefringent response of a 5 μg/ml clay sample at varying field strengths along with the calculation for Δn for a trial run at 1.4 kV/cm.

The first step in calculating the optical anisotropy is the determination of the saturation value of the birefringence Δn_s. This is best achieved by the extrapolation of Δn to infinite field strength as seen in **Figure 5.8**. The resulting value of $\Delta n_s = 3.71\text{x}10^{-9}$ can then be inserted into equation Eq. **(4.6)**, along with the calculated value of $C_v = 2.3\text{x}10^{-5}$ for the volume fraction, yielding:

$$\Delta g = \frac{\Delta n_s n}{2\pi C_v} = \frac{(3.71x10^{-9})(1.33)}{2\pi(2.30x10^{-5})} = 5.27x10^{-5}$$

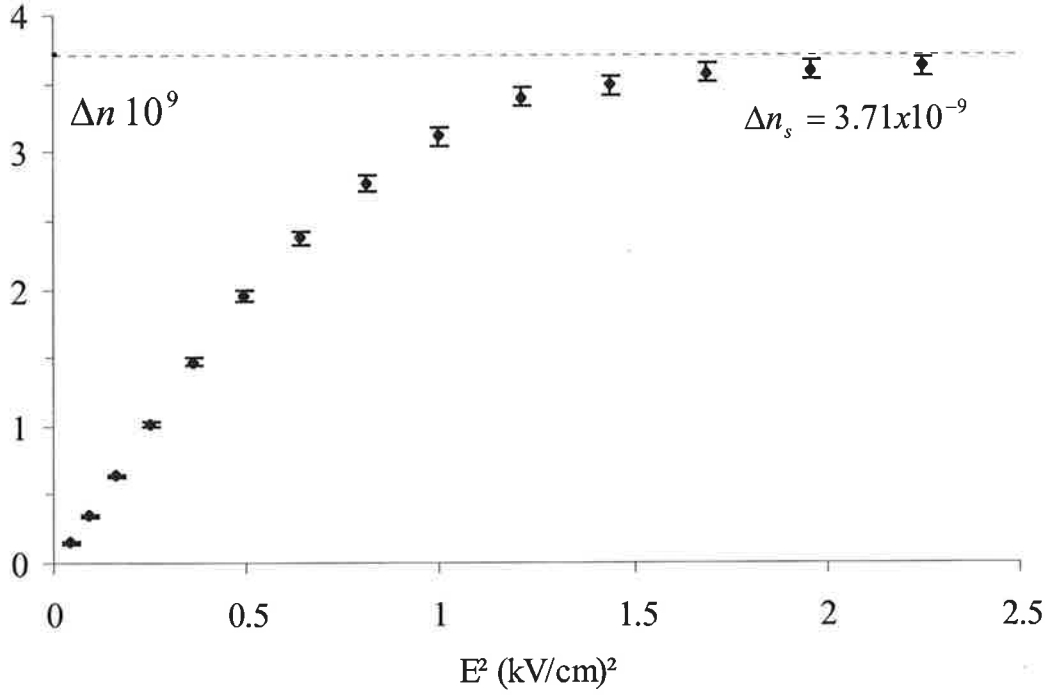

Figure 5.8: Determination of the saturation birefringence for a 5 μg/ml clay samples by extrapolation to infinite field strength

The next step is to determine the alignment mechanism, i. e., the ratio of permanent to induced dipoles at medium to high field strengths. For this purpose, a linear plot of $\Delta n/E^2$ vs. $logE^2$, normalized to its low field limit $\left(\Delta n / E^2_{\to 0}\right)$, is obtained at intermediate field strengths, as represented in **Figure 5.9**. The slope of such a plot should fall in the range of -.53 and -1.15, depending on the ratio of the permanent and induced-dipole contributing to the alignment mechanism. The current clay sample yielded a slope of -1.14, thus based on Eq. **(4.26)**, the relative contributions are $[.01\beta^2 + .99(2\gamma)]$, i.e., the permanent dipole amounts to 1% while the induced dipole contributes to 99% in achieving the overall alignment of the clay platelets. For

comparison, a theoretical curve was constructed and plotted against the experimental result. The peak value of 1.11 for the clay's response matches that obtained from theory; lending further support to the ratio of $[.01\beta^2 + .99(2\gamma)]$ for the clay platelets.

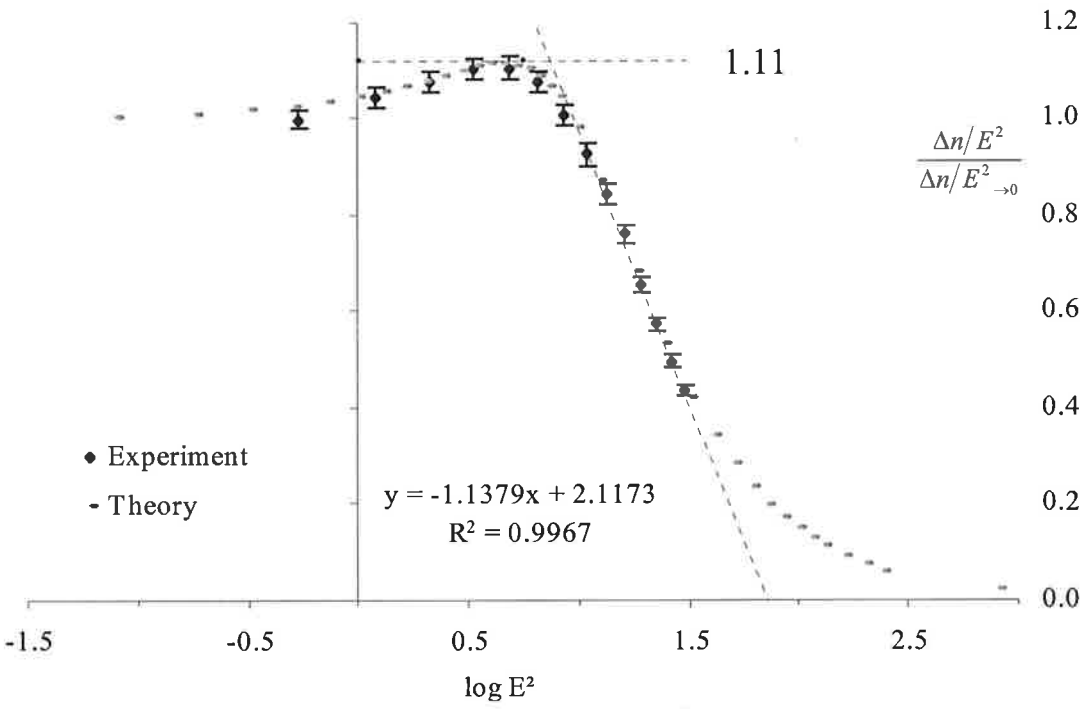

Figure 5.9: Normalized plot of $\Delta n/E^2$ vs. $logE^2$ for a clay sample laid over the theoretical curve for an alignment mechanism represented by the ratio $[.11\beta^2 + .89(2\gamma)]$.

5.6. Saturation of the Birefringent Response at Low Fields

In the low field region, a plot of the field dependent data can be used to determine the specific Kerr constant K_{sp}. **Figure 5.10** shows the results of plotting $\Delta n/E^2$ vs. E^2 for the same data set. Because the plot is a function of E^2 and not $logE^2$, the linear region at intermediate field strengths is lost. However, the new plot can now be extrapolated to field free conditions for an intercept of $\Delta n/E^2$.

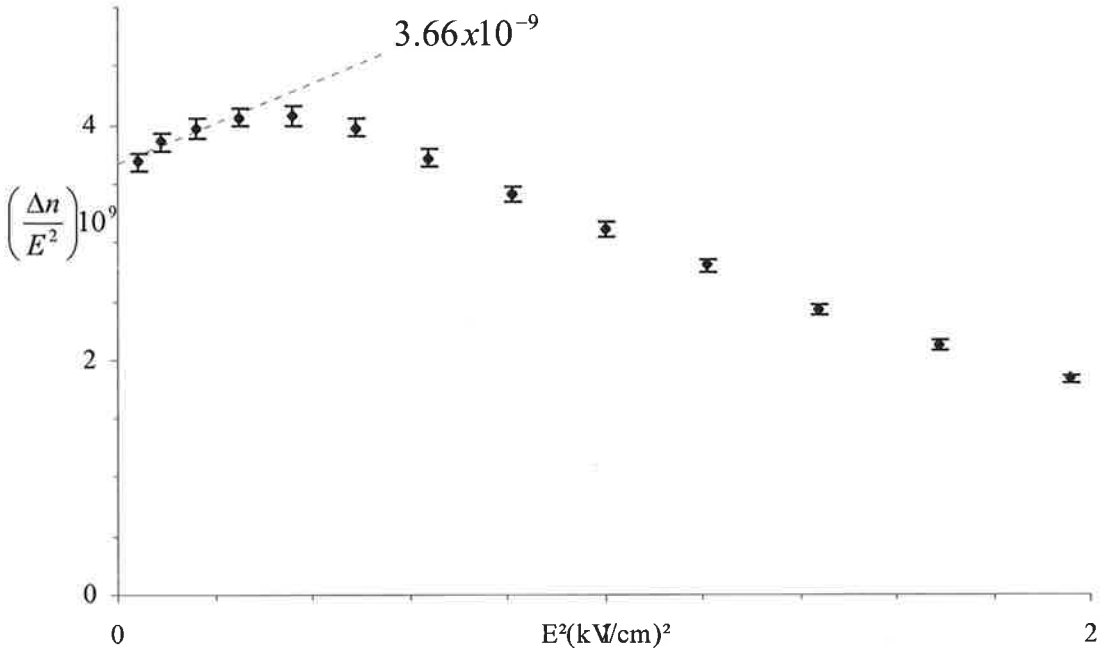

Figure 5.10: Plot of $\Delta n/E^2$ vs. E^2 for a 5 μg/ml clay sample. A linear fit on the low field data yields an estimated value of $\Delta n/E^2 = 3.66\text{x}10^{-9}$ $\text{cm}^2\text{kV}^{-2}$ at $E^2 = 0$.

In this case $(\Delta n/E^2)_{E\to 0} = 3.66\text{x}10^{-9}$ $\text{cm}^2\text{kV}^{-2}$ and, when combined with Eq. **(4.28)**, a value for the specific Kerr constant K_{sp} can be calculated as follows:

$$K_{sp} = \frac{3.66x10^{-9} cm^2 kV^{-2}}{(2.30x10^{-5})(1.33)} = 1.68x10^{-5} cm^2 kV^{-2}$$
$$= \underline{\underline{1.68x10^{-15} m^2 V^{-2}}} (SI\ units)$$

The polarizability of the clay platelet may now be obtained from the value of $(\Delta n/E^2)_{E\to 0}$ and the specific Kerr constant using Eq. **(4.29)**:

$$\Delta\alpha = 15\frac{n^2 K_{sp}}{2\pi\Delta g} kT = 15\frac{(1.33)^2(1.68x10^{-15})}{(2\pi)(3.41x10^{-5})} 4.14x10^{-21} = 5.56x10^{-31} Fm^2$$
$$= \frac{10^6}{4\pi\varepsilon_o} 5.56x10^{-31} Fm^2 = \underline{\underline{4.98x10^{-15} cm^3}}$$

For comparison, **Table 5.3** gives the values of $\Delta\alpha$ as reported in the literature by different groups. The common practice is to report $\Delta\alpha$ in units of Fm^2. However, in order to get a better feel for how the value relates to particle size, the polarizability volume $\Delta\alpha'$ has also been reported in units of cm^3. Surprisingly, the rod model correlates with the values reported by other groups better than the disk model. This is evidenced by looking at how the value for $\Delta\alpha'$ determined here scales with the value determined by the other groups and then comparing it to how the particle volume for a rod and a disk (also determined here) scales with the disk volumes reported by the same groups. It is observed that the volume for the rod model used here scales more closely with $\Delta\alpha'$ than the disk model; the difference between the ratios for $\Delta\alpha'$ and volume differing by only 3 and 19%.

Table 5.3: Polarizability anisotropies $\Delta\alpha$ for Na-montmorillonite, as reported here and by other groups. The calculated ratios show a direct correlation between $\Delta\alpha'$ and the disk/rod volumes.

Group	Vol. (cm^3)	$\Delta\alpha$ (Fm^2)	$\Delta\alpha'$ (cm^3)	$\Delta\alpha$ ratio	Vol. ratio *disk/disk*	Vol. ratio *disk/rod*
Current	**disk** = $2.78x10^{-17}$ **rod** = $5.40x10^{-19}$	$5.56x10^{-31}$	$4.98x10^{-15}$	1	1	1
Matsumoto[4]	$1.91x10^{-16}$	$1.6x10^{-28}$	$1.43x10^{-12}$	288	6.87	354
Sasai[8]	$5.11x10^{-17}$	$5.4x10^{-29}$	$4.83x10^{-13}$	97.1	1.84	94.5

The above comparison implies that the rod model might be a better representation of the clay solution. We interpret this result by considering the anisotropy in the

dimensions of a rod and a disk. Given that the rod lengths are three to four times longer than the disk diameters, the magnitude of the induced dipole in the rods could also be larger to the same degree. Such an argument becomes even more reasonable when we consider that the saturation analysis is done at intermediate fields where the alignment due to the induced-dipole has been saturated. The results obtained in this range of field strength could be only representative of the largest polarizability anisotropy.

5.7. Field Dependence of the Rise Time

The rise times were determined by fitting the same experimental data used for the concentration analysis. The resulting rise constants were plotted as a function of E^2 and are displayed in **Figure 5.11**. Unlike the decay, the rise of the birefringent response fits best to a single exponential function. This is somewhat unexpected since the geometry of the particle dictates a minimum of two constants (as was discussed in the earlier section on the rotational diffusion coefficient). It will also be seen in later sections that the fit of the rise to a single exponential is not limited to clay; it is universal among all cases studied herein. It could be argued that, because the rise of the alignment is a driven process, maybe the two constants are difficult to separate. However, this seems an unlikely explanation because the same observation was obtained even at minimal field strength when the rise time was particularly slow. Another explanation offered elsewhere is that, because the alignment is a driven process, it is free from being governed by Brownian motion.[9] Needless to say, at this

time the discrepancy between the fitting of the rise and decay portions of the curve is not understood; a question that should be explored in future work.

As was seen earlier for the decay of the birefringence, the concentration of 5 μg/ml appears to be the percolation threshold. The slower rise times for the 10 and 20 μg/ml samples can be attributed to inter-particle interactions due to an increase in repulsive forces. In contrast, the decay times of the higher concentration samples were shown to decrease; a results that can also be attributed to repulsive forces. In all cases, however, the rise times are observed to be proportional to the square of the field strength.

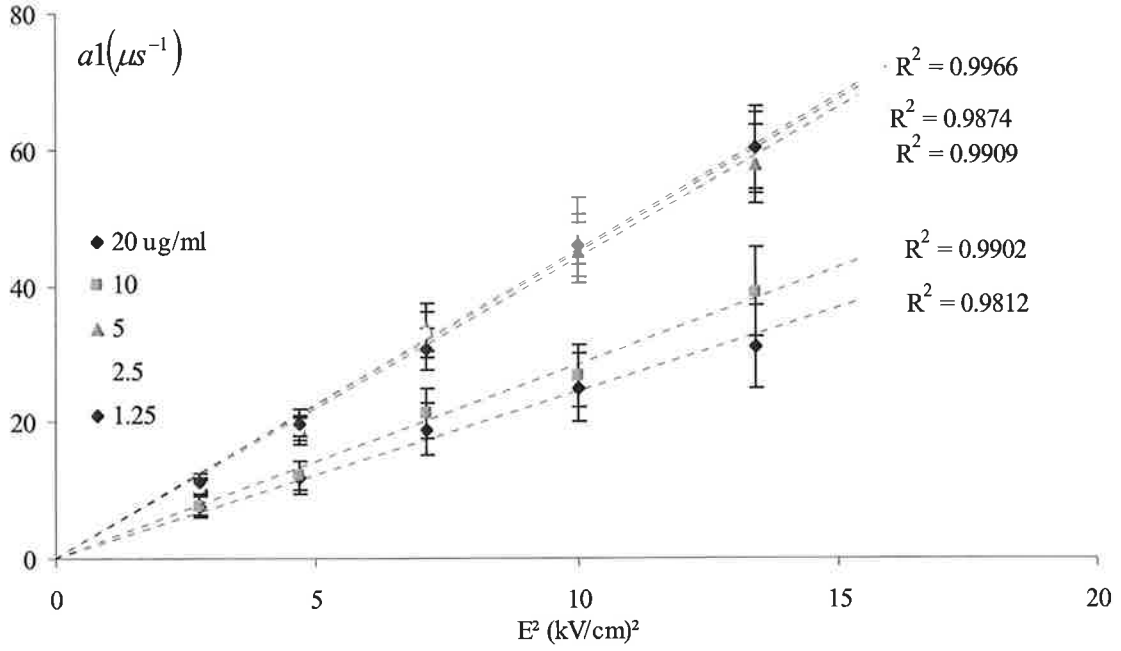

Figure 5.11: Rise constants for clay samples at varying concentrations and field strengths. All concentrations show a linear dependence on the squared field strength.

In order to calculate the polarizability anisotropy of the platelets using their rise times, the birefringence curves are first normalized to their saturation value Δn_s, which is determined by extrapolation of Δn to $E \rightarrow \infty$. The reader may recall that the same method was used in an earlier section as a first step in determining the optical anisotropy Δg. For this application, the method requires that the value of Δn_s be determined for each set of concentrations due to its dependence on the volume fraction of particles in solution. The resulting $\langle P_2 \rangle$ vs. t curve for a 5 μg/ml clay sample, subjected to a 1.7 kV/cm field is shown in **Figure 5.12**.

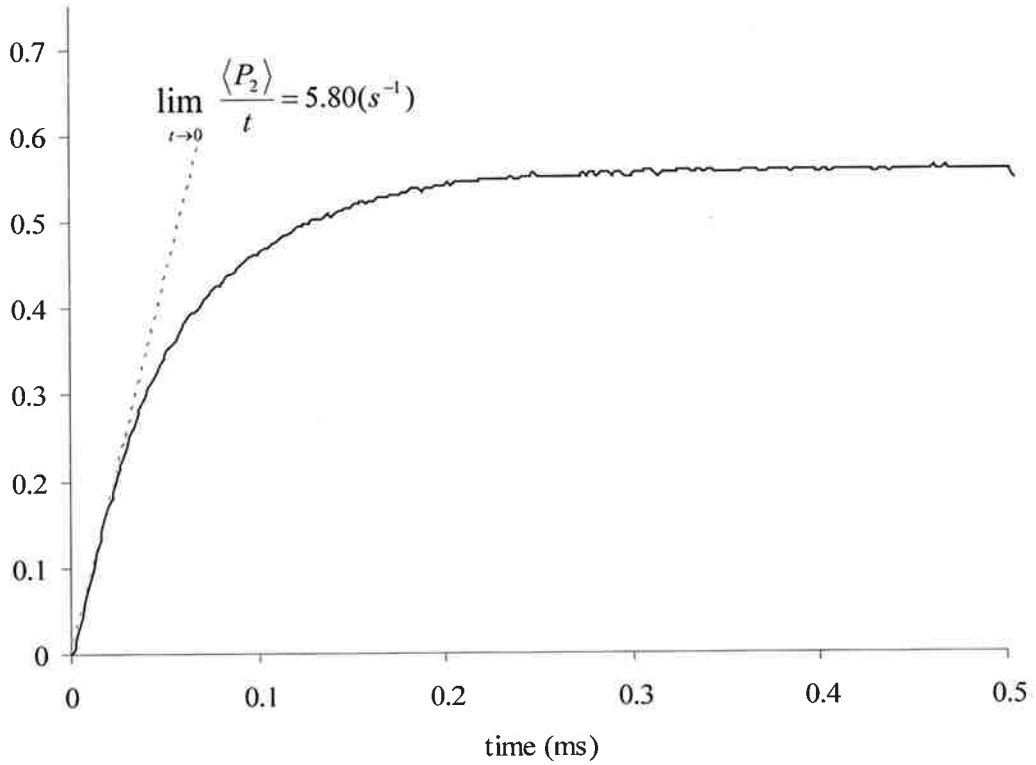

Figure 5.12: Rise curve for a 5 μg/ml clay sample subjected to a 1.7 kV/cm field. The dashed line shows the linear fit of the data in the limit where $t \rightarrow 0$.

In a weak field for a solution with no initial alignment, the response of the birefringence as $E \rightarrow 0$ results in a value of 5.80 s^{-1} for the slope. Using Eq. **(4.62)** and Eq. **(4.63)**, the polarizability anisotropy $\Delta\alpha$ is calculated as follows:

$$a_2 = \lim_{t\to 0} \frac{\langle P_2 \rangle}{tD_R} = \frac{5.80}{.559} = 10.38$$

$$\sigma = \frac{5}{6} a_2 = 8.6$$

$$\Delta\alpha = \frac{3\sigma}{\beta E^2} = \frac{(3)(8.6)}{(2.42x10^{20})(2.77x10^{10})} = 3.87x10^{-30}\, Fm^2$$

$$= \frac{10^6}{4\pi\varepsilon_o} 2.60x10^{-30}\, Fm^2 = \underline{\underline{2.46x10^{-14}\, cm^3}}$$

For this calculation the value of D_R was taken as the weighted average of the two rotational diffusion coefficients: D_R = (.65D_R(fast)+.35D_R(slow)). In comparison, the value of D_R is irrelevant to the calculation of $\Delta\alpha$ if we use the saturation data discussed in the previous section. Thus the consistency of the anisotropy from the two different methods offers some clue as to the validity of the model.

Upon inspection, it can be seen that the rise time analysis gives a value for $\Delta\alpha$ which is approximately five times larger that that obtained from the saturation analysis. The difference between the values calculated for $\Delta\alpha$ using the two methods can be understood from the following consideration. The field dependent trials use the initial response of the particles where $t \rightarrow 0$. In this region, the polarizability of the smaller diameter, disk shaped particles should govern the change in birefringence, since they will respond to the applied field faster and align with the field direction

sooner than their larger, rod shaped counterparts. In contrast, the saturation trials rely on the birefringence once total alignment has occurred. Therefore, the polarizability of the longer and more anisotropic, rod shaped particles will become dominant. Thus, the experimental polarizability anisotropy is only representative of the dominant particles under different conditions, i.e. disks at $t \rightarrow 0$ for the field dependent trials and $t \rightarrow \infty$ for the saturation trials. Of course, for the preceding argument to be considered reasonable, the two methods should result in similar values of $\Delta\alpha$ for a sample with near monodispersity. It will be shown in the upcoming analysis of CdSe quantum dots, which display a very narrow size distribution, that this is in fact the case.

The results for $\Delta\alpha$ from both the saturation and rise time analysis are displayed as functions of particle volume, along with the results from other groups, in **Figure 5.13**. Weighted averages for the disk and rod models are given, along with horizontal error bars to account for the rage of particle volumes based on values of both D_R(fast) and D_R(slow). Vertical bars have also been added to the anisotropies calculated from the rise times as they are depended on D_R as well. The figure is best read by looking at how the data points correlate to the dashed line running diagonally, which represents a linear scaling of polarizability anisotropies with volume. Thus, the close scaling of the rod model from the saturation analysis and the disk model from the rise time analysis can be observed by the fit of the linear regression ($R^2 = .9919$).

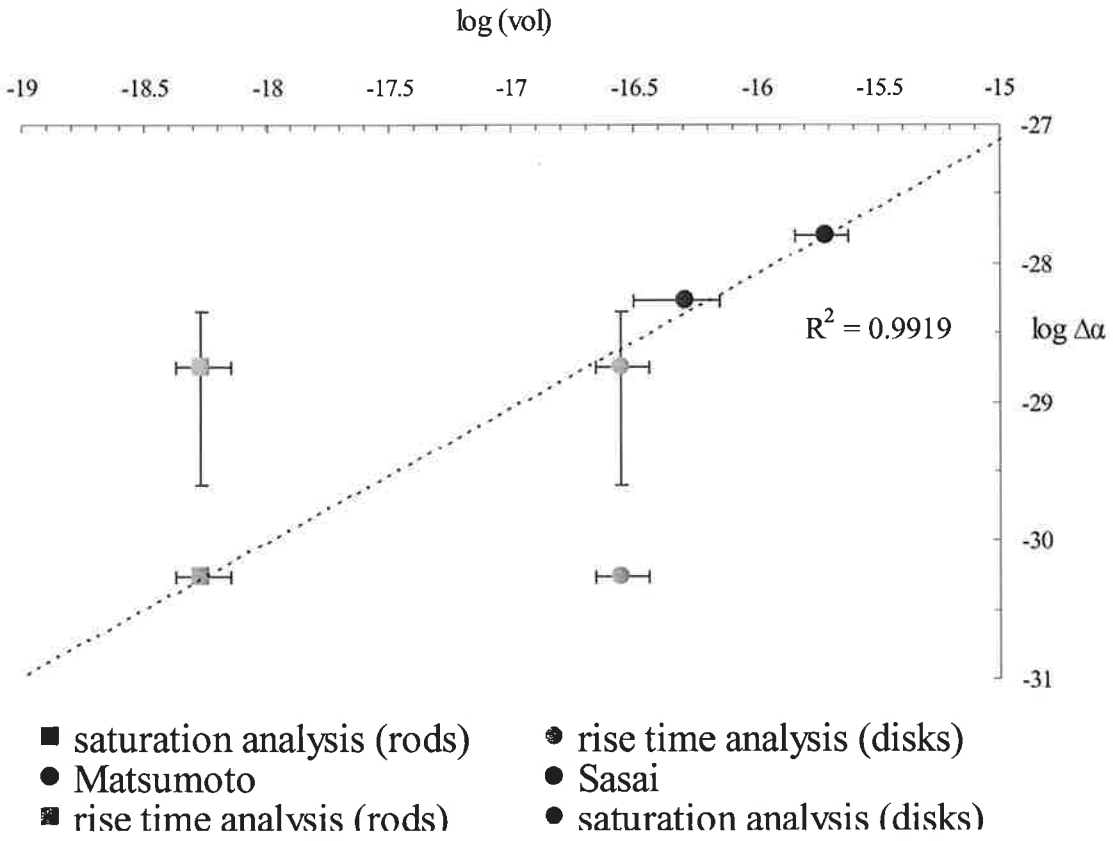

Figure 5.13: Polarizability anisotropies $\Delta\alpha$ from saturation and rise time analysis, plotted as a function of particle volume. The results for $\Delta\alpha$ from outside groups are given for comparison. Error bars are used to express the range of values given two rotational diffusion coefficients.

5.8. Birefringent response to Pulsed AC Fields

It was shown earlier and expressed through Eq. **(4.75)** that, when subjected to an alternating field, it is possible to discriminate between the effects of the permanent and induced dipole-moments on the alignment response of a particle. At low frequencies the permanent-dipole will change direction with the field while the induced-dipole only relaxes between the two extremes of the field. Both effects can result in an

observed AC component to the birefringent signal, but they are governed by two different physical processes, hence they should have different frequency dependence.

The response of a 5 μg/ml clay sample to a .67 kV/cm, pulsed AC field of varying frequency is shown in **Figure 5.14**. The signal at 2 kHz oscillates marginally with the field while, at the same time, increasing in its overall DC value. A similar trend can be seen when the frequency of the field is doubled. However, this time more of the steady state component is observed. By the time the frequency is increased to 200 kHz, the oscillating behavior of the sample has disappeared and the signal behaves as if the sample is subjected to a 500 μs DC pulse. Thus, the limiting case expressed in Eq. **(4.74)** has been reached.

In the case of Na-montmorillonite, the mechanism given by $[.01\beta^2 + .99(2\gamma)]$ does not suggest that an AC component due to a permanent dipole will be readily observed. Thus, the oscillation can be attributed to relaxation of the particles between field maximums and minimums. This explanation makes sense when the birefringence of the sample is below the saturation level and relaxation of the particle alignment instantaneously produces changes in birefringence. If, on the other hand, the birefringence had achieved saturation and the AC component was still observed at the frequencies which exceed the relaxation time of the particles, a permanent dipole could be attributed as the source. This case will be observed and addressed in the later section on quantum dots, where a direct calculation of the change in birefringence as a function of the ratio of permanent to induced-dipole is made. For now, the AC

response is presented as a qualitative method of analysis which serves to support the already determined moments in the particles.

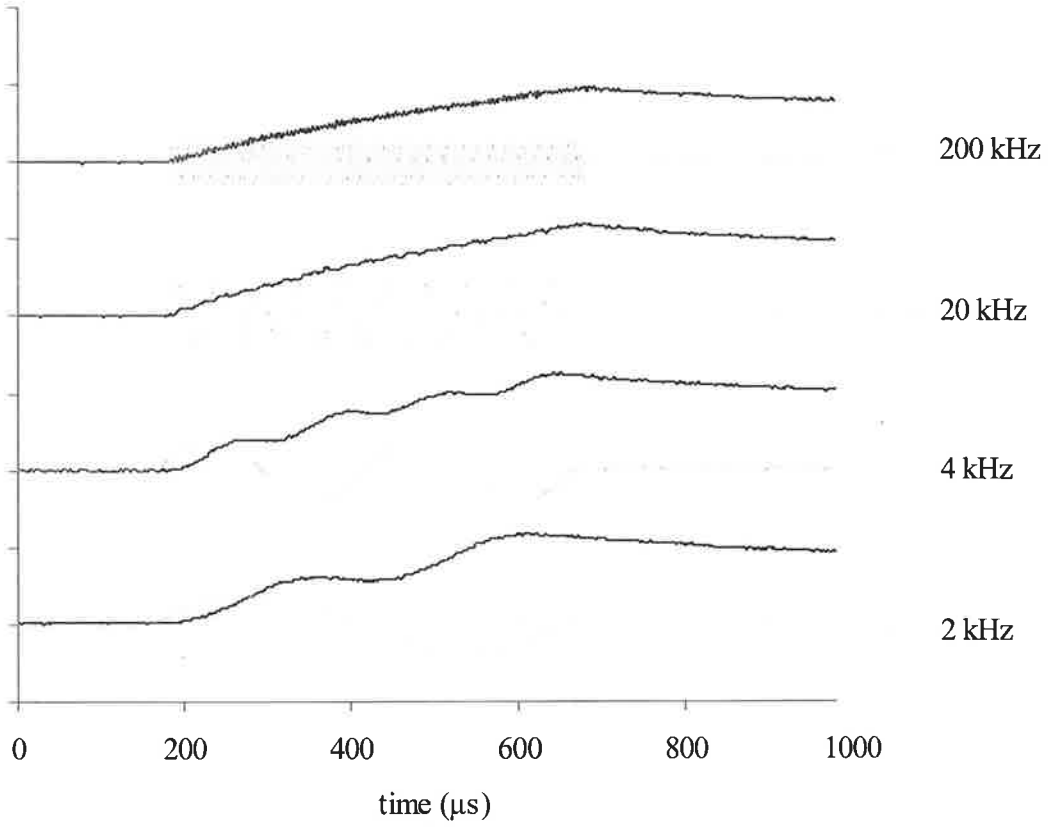

Figure 5.14: Response of a 20 ug/ml clay sample subject to a .67 kV/cm, pulsed AC field of varying frequency.

5.9. Anomalous Behavior

A few birefringent studies on clay have shown anomalous behaviors with regard to its response to alignment fields.[10-12] Some reported inversion of the birefringence upon initial application of the alignment field, while others showed much more complicated behaviors. The work of Holzheu and Hoffmann is duplicated in **Figure 5.15**. A

standard TEB signal is observed for the two curves on the far left, while the remaining curves show responses that fluctuate between positive and negative values over time at high concentrations and high ionic strengths.

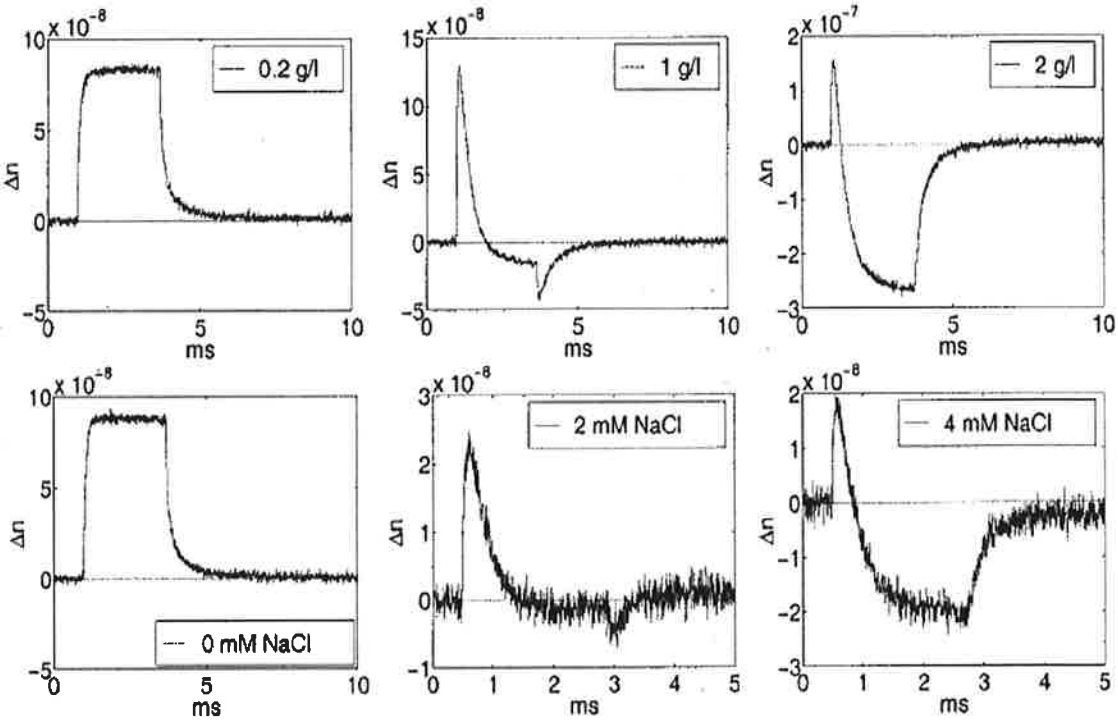

Figure 5.15: TEB signals for pure hectorite at varying concentrations and hectorite at a constant concentration of .2 mg/ml and varying ionic concentrations.

The first explanation of such anomalous signals was based on the assumption of a permanent-dipole moment perpendicular to the clay platelet surface, which would have an opposite effect from that of the fast induced dipole moment parallel to the surface. However, this explanation would imply that the anomalies are intrinsic to the clay particles and that there should be no influence from the environment. The

observations of Figure 5.15 and a few later reports have invalidated such an explanation.[12, 13]

In some cases, the particles demonstrate a negative birefringence at low fields that remains negative over the duration of the field; a behavior that has also been attributed to an apparent permanent-dipole.[14-16] Then, at higher field strengths an induced-dipole develops and, when the two dipoles are not aligned along the same direction, reorientation of the particles may occur, along with a subsequent change in the sign of the birefringence.[17] An example of this process can be seen in **Figure 5.16**, where $\langle P_2 \rangle$ values are plotted as a function of field strength, and the inversion of their steady state birefringence at low fields is observed.

Using a pulsed square wave technique, Shah and coworkers showed a response of Na-montmorillonite analogous to the example just discussed in Figure 5.16. Shah explained the reversal behavior in terms of two orientation mechanisms, i. e., the particles possess a permanent-dipole moment μ along the symmetry axis normal to the disk plane in addition to an induced-dipole moment $\Delta\alpha E$ in the plane.

In a more recent report, Sasai and Yamaoka questioned Shah's proposal by studying the steady-state birefringence in dilute solutions.[18] In order to explain the behavior of the platelets without invoking a permanent-dipole moment μ, they proposed the following, which is also outlined graphically in **Figure 5.17**:

i. The particle possesses an interfacial polarizability anisotropy $\Delta\alpha_i = (\alpha_{33}^i - \alpha_{11}^i)$, where the subscripts 33 and 11 indicate the directions

of the symmetric axis (3) and the axis along the face of the disk (1). This anisotropy is responsible for a "saturable" ionic-dipole moment, which reaches a saturation value of $\Delta\alpha_i E_o$ at the critical field strength E_o. In higher fields, the saturated induced dipole behaves like a permanent-dipole moment μ directed along the symmetry axis.

ii. The particle possesses an electronic polarizability anisotropy $\Delta\alpha_e = (\alpha_{33}^e - \alpha_{11}^e)$, which is along the plane of the platelet and "unsaturated" at the critical field strength E_o.

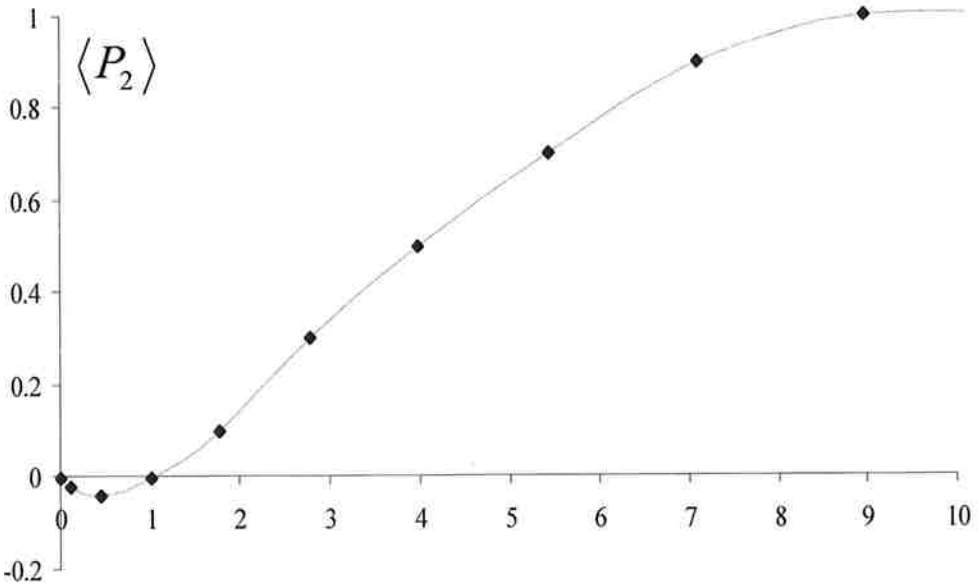

Figure 5.16: An example of the inversion of birefringence at low fields as reported by Shah and coworkers.

This explanation rests on two basic ideas. The first is that the two types of polarizations occur simultaneously, but have differing field dependence. The second is that the instantaneously induced electric dipole moment $\Delta\alpha_e E$ should always be negative. Namely, a particle is more polarizable in its plane than out of the plane. Thus, the alignment direction depends on the nature and ionic atmosphere of the clay, and is further influenced by the frequency, magnitude and duration of the applied field. By describing the alignment mechanism in this way, the time-dependent, saturable, ionic-dipole $\Delta\alpha_i$ is considered responsible for the inversion of birefringence at low fields.

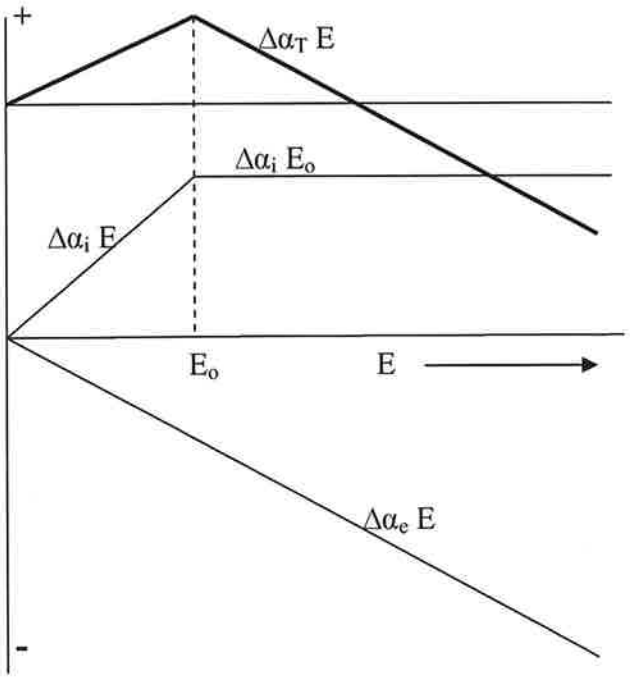

Figure 5.17: Dependence of electric moments on applied external field strength E. $\Delta\alpha_i$, is the saturable induced interfacial dipole moment, $\Delta\alpha_e$ is the unsaturable induced electric dipole moment, E_o the critical field strength, and $\Delta\alpha_T$ is the sum total of electric moments.

An inversion of the birefringence at low fields was noticed during the course of this research. However, the result could not be consistently reproduced. The observation of the sign inversion was also limited to the first few microseconds of a pulse and it

was never possible to maintain the negative value past that point. It should be noted that the lowest clay concentration studied here (1.25 μg/ml) is approximately 400x more dilute than that studied by Shah and 4x more dilute than that studied by Sasai and Yamaoka. At such a low concentration, inter-particle interactions and aggregation are unlikely to occur; as learned from studies of the percolation threshold. Thus, if the inversion phenomenon is somehow related to local field effects created by inter-particle interactions, the lower concentrations in this study should be enough to negate the response.

Although it is not the intention of this research to disprove any earlier finding, there is another issue that brings into question the results of studies which report sign inversions. Because the sign of the birefringent signal is of importance, the groups whose work is highlighted here used a quarter-wave plate in their optical setup. However, as was discussed in a previous section, the use of a quarter-wave plate should be done with extreme caution as even the smallest offset of the optics (analyzer included) can add erroneous effects to the birefringent response. As an example, **Figure 5.18** shows what is observed for a CNXL sample (known to produce only positive birefringence) when the analyzer is rotated away from the alignment direction instead of towards it. For this example the oscilloscope was AC coupled so that the baseline was set to zero. Subsequently, negative birefringence actually appears negative on the scale. The signal in blue is seen passing through a minimum when $\alpha = \delta/2$, before returning to zero and then on to its steady-state value.

This type of behavior is observed because, as the birefringence grows, it must first cancel the "negative" bias which is imposed on the system by rotating the analyzer away from the alignment direction instead of towards it. If the steady-state value is greater than the negative bias then the signal eventually becomes positive. However, as seen by the green curve, any birefringence with a phase shift δ less than 2α will remain negative. The inversion of montmorillonite samples had been studied at very low field strengths (~20 to 40 V/cm) where even the slightest discrepancy in optical adjustment could produce the described result. For this reason, the analysis of clay dispersions in this study has been limited to their response above 200 kV/cm.

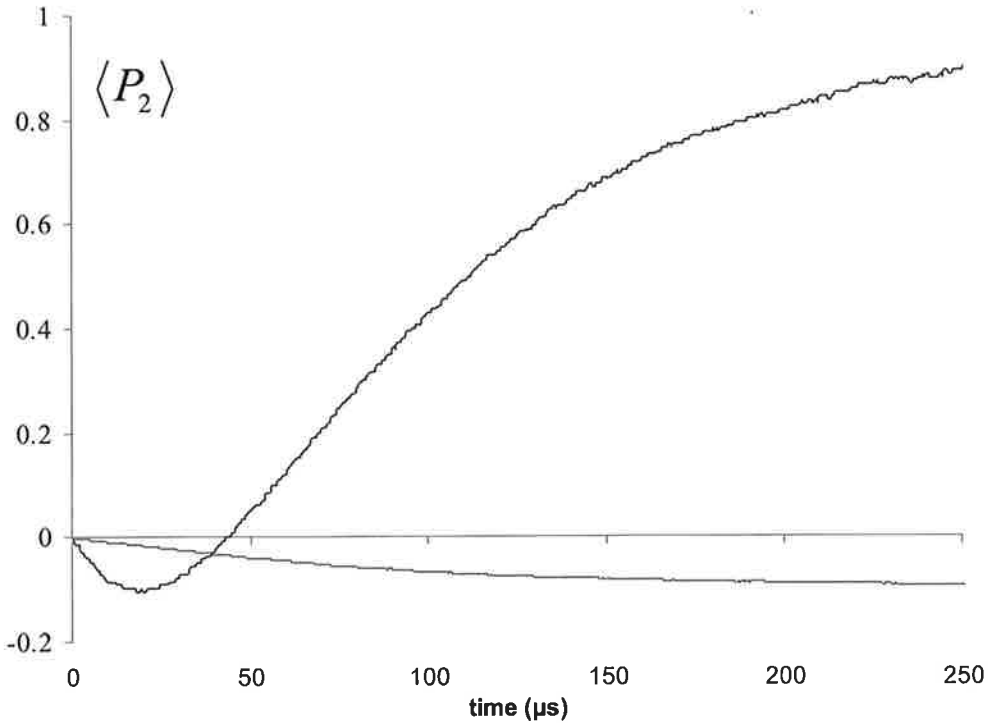

Figure 5.18: The "artificial" inversion and negative birefringence that can be induced in a positively birefringent CNXL sample by rotating the analyzer away from the direction of alignment instead of towards it.

The alignment mechanism of $[.01\beta^2 + .99(2\gamma)]$ reported herein does suggest that a small dipole moment (permanent or otherwise) may exit in conjunction with the induced-dipole moment, directed along the long axis of the particle (surface for a plate). Another possibility is that the dipole is directed at an angle, off the long axis of the particle, which is less than 90 degrees (as a perpendicular orientation would result in no projection along the long axis of the particle). However, given the inability to confidently reproduce the negative birefringence values at low fields, the presence and direction of such a dipole is inconclusive. None-the-less, the consistent observation of anomalies in the birefringence response of Na-montmorillonite by different groups does suggest that more might be going on than is understood.

Undoubtedly, a large contributing factor to the birefringent response of clay is the wide range of particle shapes that can be observed from one sample to the next. There is also a clear influence on its alignment response from the ions and their mobility along the varying clay surfaces. Therefore, although general statements may be made about the response of aqueous clay samples to electric fields, it can be expected that large differences in their physical parameters will be observed if experimental conditions and particle-ion atmospheres are not strictly maintained from one study to the next.

5.10 References

1. Craig, R.F., *Soil Mechanics*. 6th ed. 1997, London: E & FN Spon.

2. Bakk, A., et al., *Viscosity and transient electric birefringence study of clay colloidal aggregation.* Physical review. E, Statistical, nonlinear, and soft matter physics, 2002. **65**(1): p. 21407.

3. Ridgeway, D., *Estimation of particle dimensions from the relaxation of transient electric birefringence of suspensions.* Journal of the American Chemical Society, 1968. **90**(1): p. 18-22.

4. Matsumoto, M., *Transient electric birefringence of colloidal particles immersed in shear flow: Part III: A preliminary report on determination of anisotropy of electric polarizability.* Colloids and Surfaces, A: Physicochemical and Engineering Aspects, 1999. **148**(1-2): p. 75-81.

5. Baily, E.D., *A Study of the Birefringence Exhibited by Celadonite Solutions Subjected to Electric Fields.* Clay Minerals, 1976. **12**(137).

6. Yariv, S. and I. Lapides, *Laser Shadow Analysis of Particle-Size Distribution of Montmorillonites in Aqueous Suspensions.* Clays and Clay Minerals, 2003. **51**(1): p. 23-32.

7. Furukawa, Y., et al., *Aggregation of Montomorillonite and Organic Matter in Aqueous Media Containing Artificial Seawater.* Geochemical Transactions, 2009. **10**(2).

8. Sasai, R. and K. Yamaoka, *Electrooptics in Dispersed Systems. 4. Steady-State Electric Birefringence of Disk-Shaped Particles with Various Electric Moments and the Orientation Function: Case of Montmorillonite in Aqueous Media.* J. Phys. Chem. , 1995. **99**(50): p. 17754-62.

9. Donovan, K.J. and K. Scott, *Transient electric birefringence in suspensions of single-walled carbon nanotubes.* Physical Review B: Condensed Matter and Materials Physics, 2005. **72**(19): p. 195432/1-195432/8.

10. Brown, B. and B.R. Jennings, J. Colloid Sci., 1973. **43**: p. 172.

11. Jennings, B.R., B. Brown, and H. Plummer, J. Colloid Interface Sci., 1970. **32**(606).

12. Holzhen, H. and H. Hoffman, *Mechanistic Origin of Transient Electric Birefringence Anomaly of Clay Mineral Dispersion.* J. Phys. Chem. B., 2002. **106**: p. 4412.

13. Szabo, A., M. Haleem, and D. Eden, *Theory of the transient electric birefringence of rod-like polyions: coupling of rotational and counterion dynamics.* J. Chem. Phys. , 1986. **85**(12): p. 7472-9.

14. O'Konski, C.T., *Electric properties of macromolecules. V. Theory of ionic polarization in polyelectrolytes.* J. Phys. Chem. , 1960. **64**: p. 605-19.

15. Shah, M.J., D.C. Thompson, and C.M. Hart, *Reversal of electro-optical birefringence in bentonite suspensions.* J. Phys. Chem. , 1963. **67**: p. 1170-8.

16. Shah, M.J. and C.M. Hart, *The electro-optical birefringence of polydisperse bentonite suspensions.* IBM J. Res. Develop. , 1963. **7**(No. 1): p. 44-57.

17. Shah, M.J., *ELECTRIC BIREFRINGENCE OF BENTONITE. II. AN EXTENSION OF SATURATION BIREFRINGENCE THEORY.* Journal of Physical Chemistry, 1963. **67**(10): p. 2215-2219.

18. Sassi, J.-F. and H. Chanzy, *Ultrastructural aspects of the acetylation of cellulose.* Cellulose (London) , 1995. **2**(2): p. 111-127.

6. Cellulose Nanocrystals (CNXL)

6.1. Introduction

The decision to include CNXL in this research began during a brief collaboration with Dr. John Simonsen; a professor here at OSU in the department of wood science. He suggested that given the high aspect ratio, high stiffness, and low density of CNXL, they should be an excellent candidate for TEB studies. After a few preliminary measurements it was clear that his hypothesis was correct. Not only did the CNXL samples from his laboratory display field induced birefringence, but also was its birefringence considerably larger than any other material we had seen thus far.

Cellulose is reportedly the world's most abundant biopolymer and acts as a reinforcement material in virtually all plant matter. The structure of cellulose shown in **Figure 6.1** is derived from a linear chain of β-linked glucose monomers, with multiple chains arranging to form cellulose fibrils through hydrogen bonding. The fibrils can be partially dissolved by acid hydrolysis, producing rod shaped nanocrystals (CNXL).

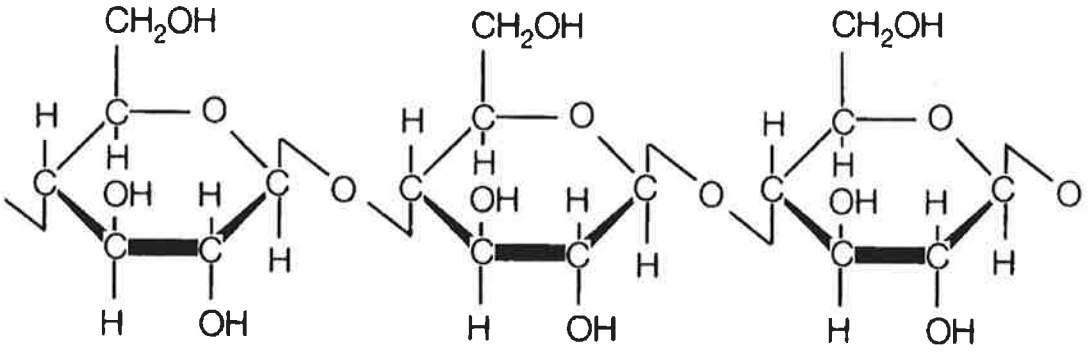

Figure 6.1: Three of the β linked glucose monomers making of the backbone of cellulose nanocrystals.

Individual cellulose crystals are prepared from cotton by hydrolysis, which is typically done using sulfuric or hydrochloric acids. There are many sources by which the crystals can be acquired; each having a different extent of cellulose purity: [1, 2]

- cotton-seed fluff $\geq 94\%$
- wood $\geq 55\%$.

The preparation begins with initial acid action to remove the polysaccharide material closely bonded to the microfibrill. Subsequent hydrolysis then breaks down portions of the long glucose chain in accessible, noncrystalline regions. Once the degree of polymerization is lowered to a level where only the highly crystalline regions of the original cellulose fiber remain, hydrolysis is terminated by rapid dilution of the acid. A combination of centrifugation and extensive dialysis is then employed to remove the acid and the final product is sonicated to complete the process of dispersing the individual crystals. The cellulose rods that remain after this treatment are almost entirely crystalline and as such are termed crystallites (**Figure6.2**).

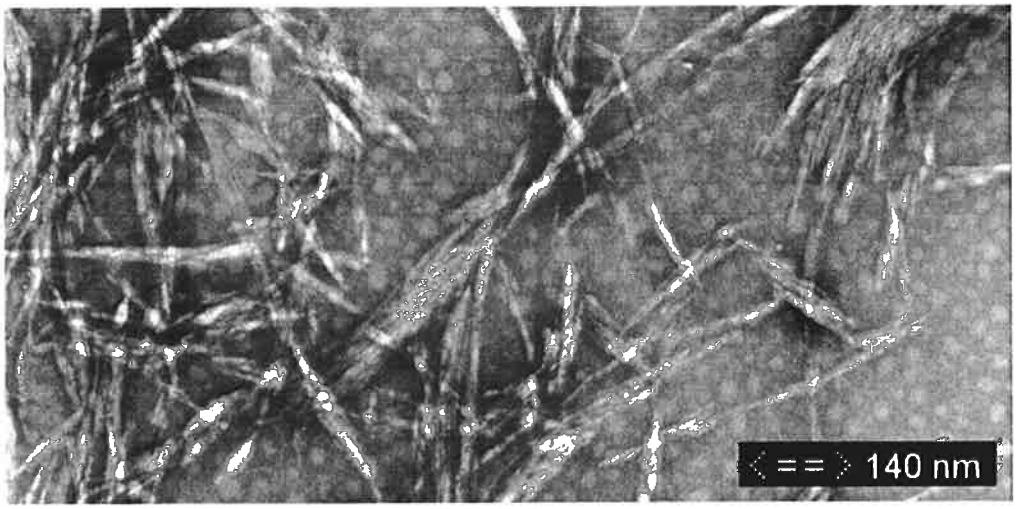

Figure 6.2: TEM image of cellulose nanocrystals derived from cotton.

Forest-based products have long capitalized on the ability of cellulose to form fibrils and new forest-based functional materials have the potential to compete with established materials such as plastics, clays, metals and metal alloys. **Table 6.1** shows some of the physical properties of cellulose and how it compares to other common materials.

Table 6.1: Tensile strength and Modulus of some common materials.

Material	Tensile Strength (MPa)	Elasticity Modulus (GPa)
CNXL	10,000	150
302 Stainless steel[3]	1280	210
Al alloy 380[3]	330	71
Zirconia[4]	240	150
Al with 20% SiC[4]	593	121
Nylon 6/6 30% SiO_2[4]	503	65

The desirability of CNXL as a nano-filler is not only based on performance but also on merits of recyclability, biodiversity, biodegradability, and sustainability. The current uses of cellulose as a reinforcement material in non-biological materials are widely reaching. Examples include, but are not limited to, strengthener in plastics,[5-7] ceramics,[8-10] and in biomedical material applications.[11-13]

Although a large amount of work has been reported on cellulose nanocrystals, almost all has focused on their potential as an additive to other materials and little has been devoted to their single particle properties. As an example, a search on SciFinder using the phrase "cellulose nanocrystals" returned 154 citations; 145 of which pertained to their use in nanocomposites and nanomaterials. Thus, this work represents the first systematic study of cellulose crystallites at the single particle level.

What is presented here is a detailed analysis of the properties of cellulose crystals in an aqueous system. Our results indicate that CNXL has a larger polarizability and an extreme ability to induce large phase shifts in polarized light. The presence of a small dipole will also be addressed, along with its possible contribution to the nematic liquid crystal behavior that CNXL has been shown to display at high concentrations.

6.2. Analysis Overview

The analysis of the CNXL samples will be separated into four parts. The following section outlines each analytical technique, the physical property it depends on, and how that property will be used to characterize the sample:

1) **Concentration dependence of the decay mechanism** will be followed in order to determine the sample's percolation threshold. Once a suitable concentration range has been established, the rotational diffusion coefficient D_R will be calculated from the decay constants and used to determine particle dimensions.
2) **Saturation of the birefringent response** Δn will be studied by plotting its value against varying functions of E^2 and using features such as the slope, local maximum, and y-intercept to determine the following:
   - Optical anisotropy Δg

- Specific Kerr constant K_{sp}
- Orientation mechanism i.e. the ratio of permanent to induced-dipole moment
- Single particle polarizability anisotropy $\Delta\alpha$
- Single particle permanent dipole μ

3) **Field dependence of the rise time** will be followed to elucidate the orientation mechanism (induced-dipole and/or permanent-dipole). The rise times in the low field limit will also be used (along with the rotational diffusion coefficient from section 1) to calculate single particle polarizability anisotropies. The results will then be compared with the values obtained from the analysis of section 2.

4) **Pulsed AC trials** will be conducted as a supplemental study to further confirm the alignment mechanism. The ratio of the permanent dipole to the polarizability anisotropy will be used to estimate the change in birefringence in moving from the low frequency to the high frequency limit. The results of the calculation will then be compared to the response of the crystallites to 2 and 200 kHz, pulsed AC fields.

6.3. Experimental

An aqueous sample of cellulose nanocrystals (~1.5 %wt) was supplied by Melissa Taylor in Dr. Simonsen's research group. The following method was graciously supplied by her and outlines the preparation of the sample:

> 60 g of Avicel PH-101 microcrystalline cellulose (Fluka) was hydrolyzed in 1 liter of 2.4*M* HCl for 2 hours at 100 °C, allowed to cool to room temperature, then washed with deionized water until conductivity of supernatant was less than 100 micro-Seimens. Pellet was brought to pH > 9 with aqueous 4*M* NaOH, then 60 mg of 2,2,6,6-Tetramethylpiperidine-1-oxyl (TEMPO) free radical (Aldrich) per gram cellulose and 10 g NaBr (EM Scientific) per gram cellulose was added to the pellet. Oxidation was initiated by adding 6% sodium hypochlorite (NaOCl). Oxidation reaction was continued for 24 hours while solution was maintained at pH > 9.7 with 1*M* NaOH, and the oxidation/reduction potential above 400 mV with frequent addition of NaOCl. Reaction was quenched by the addition of 100 mL methanol, then solids were cleaned by dialysis against DI water. Pellet was then ultrasonicated 6 hours at a duty cycle of 45%, power output of 4.5 (Branson Sonifier, model 250), then filtered down to 1.5 μm with Whatman glass fiber filters.

Sample solutions were prepared from the stock solution by the direct addition of deionized water, followed by a ten minute sonication period.

6.4. Concentration Dependence of D_R

The purpose of the concentration trials is to determine the percolation threshold for the cellulose crystallites. As the sample concentration increases, the inter-particle distance is reduced and interactions occur due to the limited space. With increasing field strength the order within the system will also increase. A simple method for determining a threshold concentration is to follow the diffusion as a function of the alignment field and concentration. If inter-particle interactions are present, both factors will have an observable effect on D_R.

Following the procedure described for the clay sample, field strength trials were run on CNXL samples ranging from .15 to .019 %wt. In each case the decay curves were fit using the double exponential expression represented by Eq. **(4.71)**. The results for a fast and slow rotational diffusion coefficient D_R as a function of field strength were determined. However, the difference between the amplitudes of the two exponential functions is approximately two orders of magnitude; with values for D_R(fast) and D_R(slow) of .98 and .02, respectively. In order to determine if preference could be given to the biexponential model, an F-test was performed using the χ^2 values from each fitting. A limiting value of $F \approx 3.84$ at a 95% confidence level was taken from the available tables.[14] Given that the decay curves consisted of ~1000 data points and that two and four adjustable parameters were involved in the fitting, the value of F for the given chi squared values was:

$$F = \frac{\chi^2_{v1}}{\chi^2_{v2}} = \frac{\chi^2_1/(1000-2)}{\chi^2_2/(1000-4)} = \frac{.011^2/998}{.004^2/996} = 7.56$$

Hence, a double exponential fit is a more appropriate model for the system. The two observed values for the rotational diffusion coefficient show a similar trend to those of clay in that they are separated by approximately one order of magnitude, as seen in **Figures 6.3 & 6.4**. For each set of data there appears to be a slightly faster decay for the highest concentration sample, while the remaining concentrations have decay constants within the standard deviation, which remained at ~10% for all groups of samples. There also appears to be little change in the fast D_R as the field strength is increased, with virtually no change for the slow values.

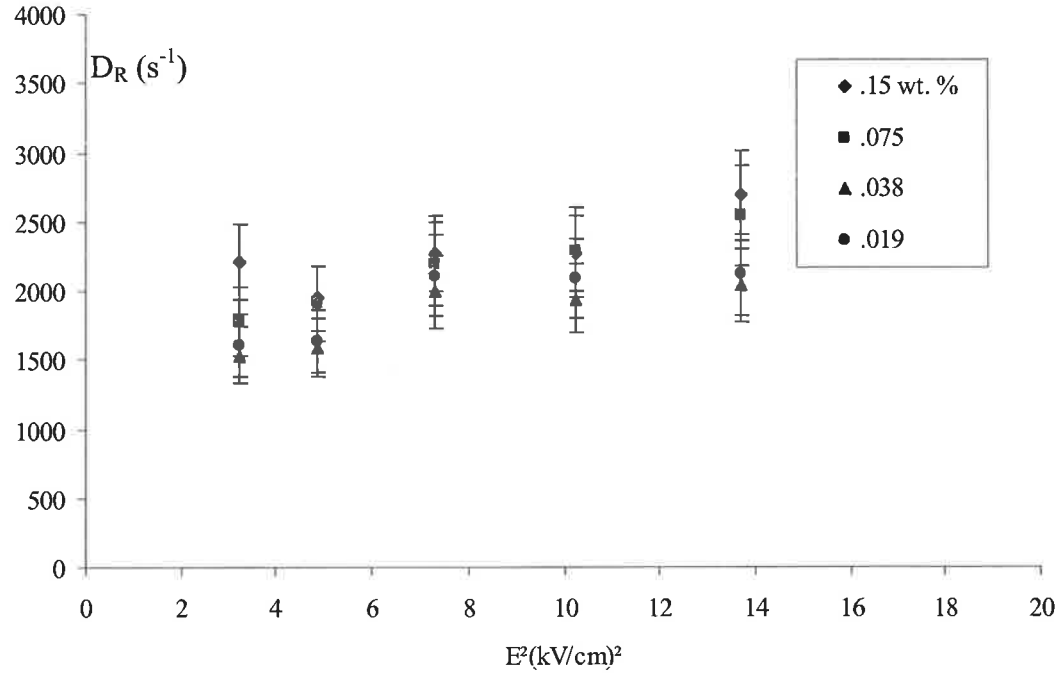

Figure 6.3: "Fast" rotational diffusion coefficients D_R for CNXL at varying concentrations as a function of the squared field strength.

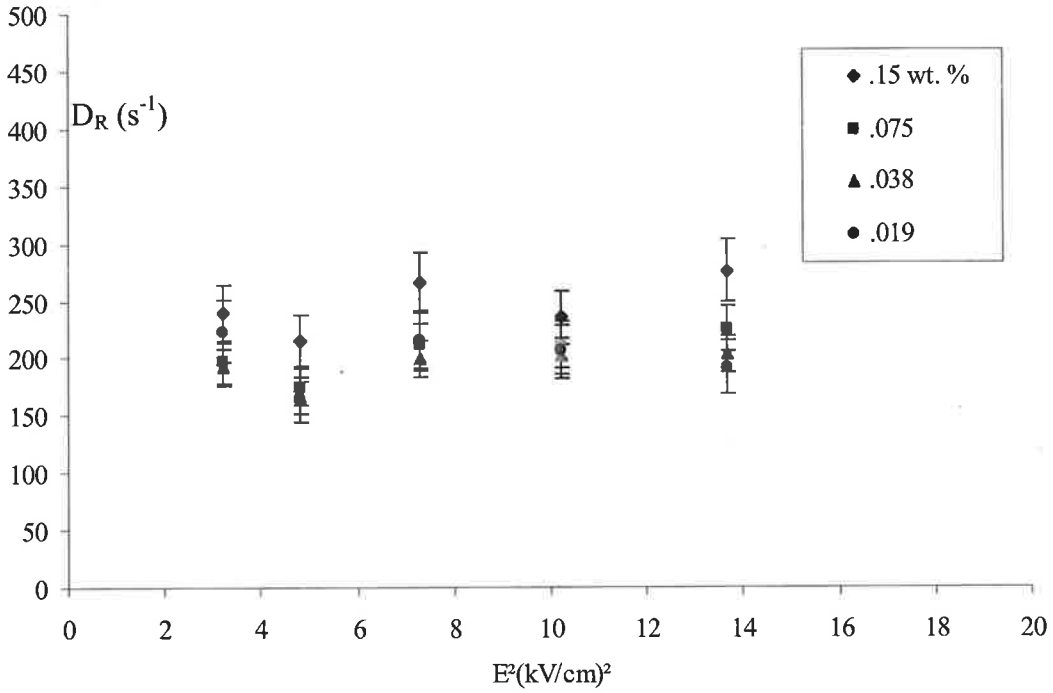

Figure 6.4: "Slow" rotational diffusion coefficients D_R for CNXL at varying concentrations as a function of the squared field strength.

The weak dependence on concentration and negligible dependence on field strength observed in the decay data suggests that even the highest concentration sample is below the percolation threshold for aqueous CNXL. Given the desire to always maintain a large signal to noise ratio, it would seem reasonable to increase the concentration until the maximum value below the threshold is achieved. However, further increase in concentration proved to be unnecessary due to the large optical anisotropy of CNXL, calculated as follows:

$$\Delta g = \frac{\Delta n_s n}{2\pi C_v} = \frac{(3.14x10^{-6})(1.33)}{2\pi(9.37x10^{-6})} = 3.55x10^{-2}$$

For this reason, samples well below the percolation threshold were used to prevent the detection system from being overloaded.

An interesting consequence of the large optical anisotropy of CNXL is "over-rotation" of the probe beam at high concentrations/field strengths, i.e., the induced phase shift reaches multiples of π. **Figure 6.5** shows an example when δ reaches 4π in a 2.0 kV/cm field for a 1.0 %wt CNXL solution. The applied field is overlaid with the birefringent response of the sample. The oscillations to the right of the square wave are due to relaxation, and it was observed that the number of cycles from the relaxation were equal to the number of cycles when the field was applied. In addition, we also confirmed the nature of the oscillation by extending the beam path and changing the concentration.

The ability of cellulose nanocrystals to induce such a significant phase shift is one of their multiple properties shared with liquid crystals. For example, it has been shown by Lima and Borsali that as the concentration of cellulose crystallites is increased, they form spontaneously ordered phases, displaying nematic liquid crystal properties. [15] At higher concentrations, the suspensions form birefringence droplets that coalesce to give cholesteric packing by spontaneous self-assembly. It will also be shown momentarily that the specific Kerr constant of CNXL is of the same order of magnitude (~10^6 m^2V^{-2}) as that of many liquid crystals.[16-18] Such results suggest that CNXL may be a greener alternative to liquid crystals in electrics applications; an idea that should certainly be explored further.

Unlike Na-montmorillonite addressed earlier, CNXL is best modeled as a rigid rod. Thus, calculations for the average crystal length based on the fast and slow rotational diffusion coefficients were done using Eq. **(4.68)** and displayed in **Table 6.2**. The length to diameter ratio of L/a = 40 was chosen based on TEM images in the literature and conversations with Dr. Simonsen,

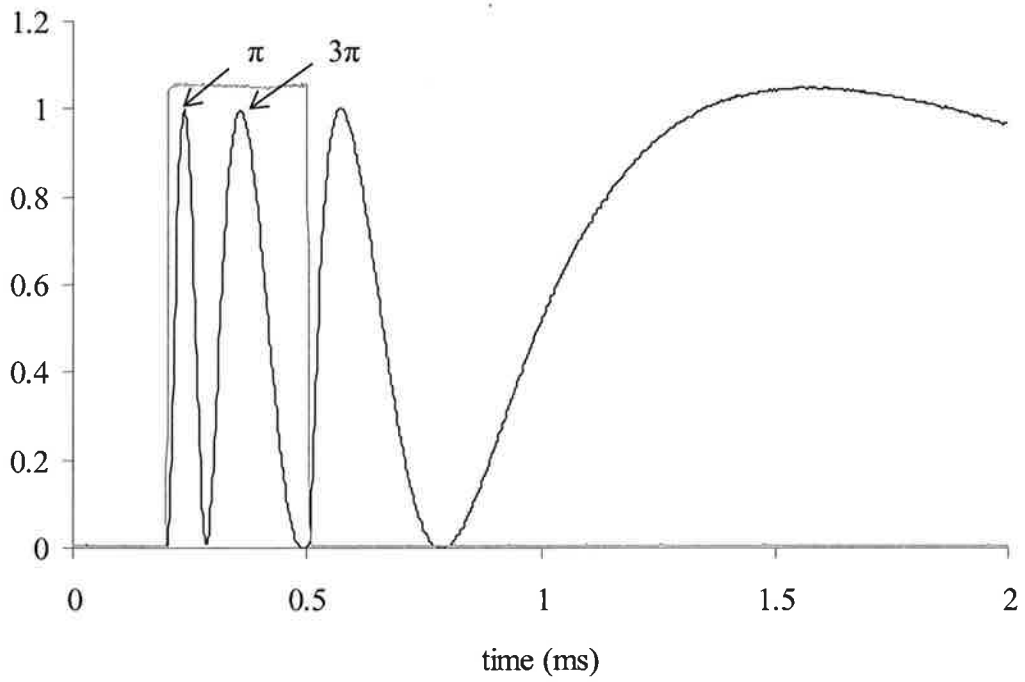

Figure6.5: TEB signal of a 1.0 %wt CNXL sample displaying a phase shift in the probe beam equal to ~4π; each maximum and minimum being equal to a phase shift of π.

The precise dimensions of the crystallites depend on several factors, including the source of the cellulose, the exact hydrolysis conditions, and the ionic strength of the solution environment.[19] Reported dimensions determined by TEM vary for crystallites derived from different species : 4 x 180 ± 75 nm for bleached softwood

pulp,[20] 7 x (100 - 300) nm for cotton,[1] and 20 x (100 – 2000) nm for Valonia.[21] The results reported here of 5 x 205 nm, for the faster coefficient, are in excellent agreement with those of other studies which were also done on cotton derived crystals.

Table 6.2: Average lengths and diameters for aqueous CNXL based on a slow and fast rotational diffusion coefficient and a length to diameter ratio of L/a = 40.

% wt	D_R (s^{-1})		rod length (nm)		rod diameter (nm)	
	fast	slow	fast	slow	fast	Slow
.15	2278 ± 246	266 ± 42	197 ± 7	414 ± 14	5.0 ± .2	10.4 ± .4
.075	2140 ± 304	203 ± 19	201 ± 10	440 ± 14	5.0 ± .2	11.0 ± .4
.038	1823 ± 236	193 ± 16	212 ± 10	449 ± 13	5.2 ± .2	11.2 ± .4
.019	1913 ± 263	201 ± 23	208 ± 10	443 ± 18	5.2 ± .2	11.0 ± .4
	2039 ± 307	**211 ± 29**	**205 ± 11**	**436 ± 19**	**5.0 ± .2**	**11.0 ± .4**

Another study on CNXL using TEB and dynamic depolarized light scattering (DDLS) measurements was reported by Lima and Wong et al.[22] Similar to the results reported here, they also found, using both methods, that the birefringent decays were best fit using a biexponential function. It was mentioned in the earlier section on the rotational diffusion coefficient that it is common for the existence of two constants to be attributed to polydispersity and not the presence of three unique axies in the particle. We see the trend continuing here, as Lima and Wong attributed the existence of two decay constants, with amplitudes of .90 and .10, entirely to polydispersity and

disregarded the constant that did not result in reasonable particle dimensions; suggesting that it represented smaller fragments which are resolved into a separate relaxation mode. The particle dimensions they reported of L= 255 ± 26 nm and d = 15 ± 2 nm (based only on their slower rotational diffusion coefficient, with an amplitude of .90) are also in good agreement with the dimensions determined here for the faster of the two coefficients; both of which are the dominant modes from each study.

6.5. Saturation of the Birefringent Response at Low Fields

The birefringent responses for a $1.50x10^{-3}$ %wt CNXL sample, subject to fields between .02 and 1.5 kV/cm were recorded after averaging over 128 pulses at 2 Hz, with a pulse width of 500 μs. The change in birefringence Δn at each field strength was calculated according to Eq. **(3.35)** for an optical arrangement with a quarter-wave plate.

With the value of the optical anisotropy already acquired ($\Delta g = 3.55x10^{-3}$), the next step is to determine the specific Kerr constant K_{sp}. A non-normalized plot of the data yielded a value for $\Delta n/E^2$ where $E \rightarrow 0$ of $1.57x10^{-6}$ cm^2kV^{-2}. When combined with **(64)**, the specific Kerr constant K_{sp} is calculated as follows:

$$K_{sp} = \frac{1.57x10^{-6}\,cm^2kV^{-2}}{(9.37x10^{-6})(1.33)} = 1.45x10^{-2}\,cm^2kV^{-2}$$

$$= \underline{\underline{1.45x10^{-12}\,m^2V^{-2}}}\,(SI\ units)$$

6.6. Saturation of the Birefringent Response at High Fields

The determination of the ratio of permanent to induced-dipole moment in the cellulose nanocrystals was carried out using the plot in **Figure 6.6** of $\Delta n/E^2$ vs. $logE^2$, normalized to its low field limit, for a series of CNXL samples. The slope of -1.12 at intermediate field strengths, when combined with Eq. **(4.26)**, results in an estimated contribution of $[.05\beta^2 + .95(2\gamma)]$, i.e., 95% of the alignment originated from the induced dipole in the cellulose crystals. For comparison, a theoretical curve was constructed and plotted against the experimental result. The peak value of 1.10 for the CNXL response matches that obtained from theory; further supporting a ratio of $[.05\beta^2 + .95(2\gamma)]$ for the crystals.

In order to determine the permanent and induced-dipole, a horizontal shift of 0.265 was applied to the experimental data so to overlap with the theoretical curve. This procedure was addressed in an earlier section, but has not been utilized up to this point. It uses the logarithmic relation in Eq. **(4.30)** that results from the graph of the normalized data as a function of $logE^2$ as follows:

$$\log(P+Q)+\log E^2 = 0.265+\log E^2$$

$$\log(P+Q)=0.265$$

$$P+Q=1.84x10^{-10}\,m^2V^{-2}$$

where P, the permanent-dipole term, is $P = \beta^2/E^2 = \mu^2/k^2T^2$ and Q, the induced-dipole term is $Q = 2\gamma/E^2 = \Delta\alpha/kT$.

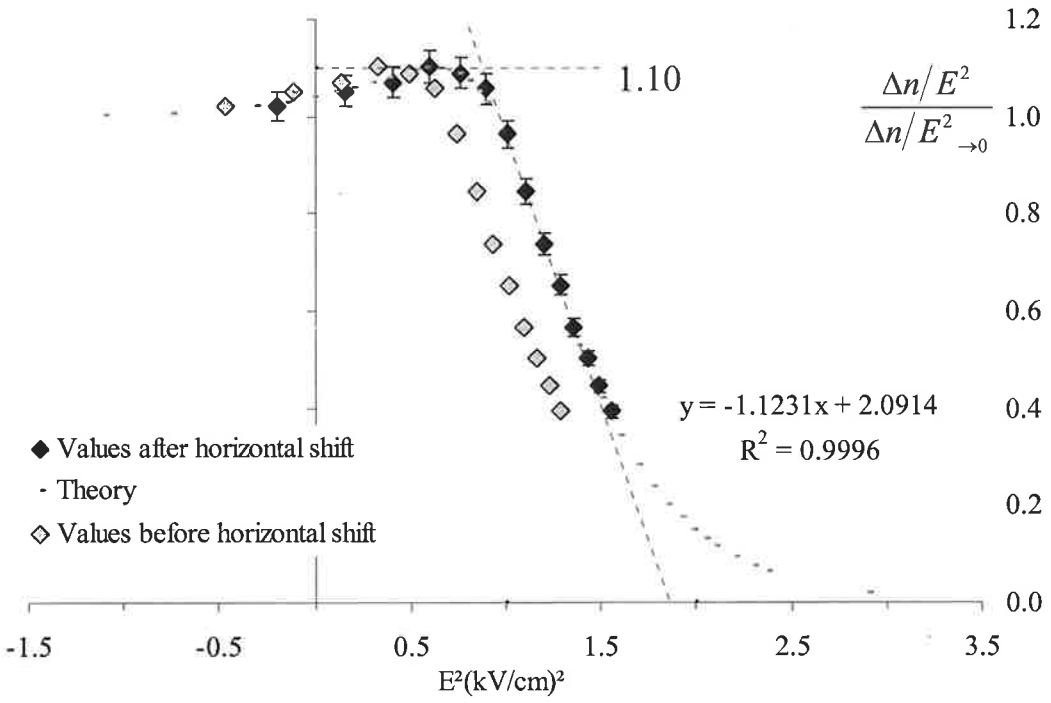

Figure 6.6: Normalized plot of $\Delta n/E^2$ vs. $logE^2$ for a CNXL sample laid over the theoretical curve for an alignment mechanism of the ratio $[.05\beta^2 + .95(2\gamma)]$.

From the specific Kerr constant K_{sp}, and the ratio of the permanent moment and polarizability anisotropy, we can now determine both the permanent-dipole and polarizability anisotropy using Eq. **(4.29)** as follows:

$$P = 1.84x10^{-10}\, m^2V^{-2} - Q \qquad [.05P + .95Q] = \frac{15K_{sp}n^2}{2\pi\Delta g}$$

$$[.05(1.84x10^{-10}\, m^2V^{-2} - Q) + .95Q] = \frac{15(1.45x10^{-12}\, m^2V^{-2})(1.33)^2}{2\pi(3.55x10^{-2})}$$

$$9.20x10^{-12}\, m^2V^{-2} - .90Q = 1.73x10^{-10}\, m^2V^{-2}$$

$$Q = 1.82x10^{-10}\, m^2 V^{-2} \qquad P = 2.21x10^{-12}\, m^2 V^{-2}$$

$$\frac{\Delta\alpha}{k_B T} = 1.82x10^{-10}\, m^2 V^{-2} \qquad \frac{\mu^2}{k_B^2 T^2} = 2.21x10^{-12}\, m^2 V^{-2}$$

$$\Delta\alpha = 7.53x10^{-31}\, Fm^2 \qquad \mu = 6.16x10^{-27}\, Cm$$

$$\Delta\alpha' = 6.74x10^{-15}\, cm^3 \qquad \mu = 1.84x10^{3}\, D$$

Although not ideal, a comparison with the clay sample studied earlier can serve as a reference for the value of $\Delta\alpha$. In this case it is appropriate to use the rod model for the clay sample. The volume of clay rods was determined to be ~$5.4x10^{-19}$ cm^3, and the corresponding polarizability anisotropy from saturation analysis was $\Delta\alpha = 5.56 \times 10^{-31}$ Fm^2. For cellulose crystals, a volume of $1.26x10^{-18}$ cm^3 was obtained based on the results from field free relaxation. The ratios of polarizability and volume for the two samples are:

$$\frac{\Delta\alpha(CNXL)}{\Delta\alpha(clay)} = 1.35 \qquad \frac{vol(CNXL)}{vol(clay)} = 2.32$$

Although not identical, the similarity between the two ratios does suggest that the value of $\Delta\alpha$ determined for CNXL here should be not too far off.

There are currently no reports in the literature on the existence of a dipole in CNXL. However, its likely presence can be argued based on some properties in

aggregation. For example, above a critical concentration, cellulose suspensions separate into isotropic and anisotropic phases. It has also been found that nanocrystal suspensions prepared from cellulose form *chiral nematic order* at appreciably high concentrations.[23] Several hypotheses have been presented to explain the origin of a *chiral nematic phase* in cellulose nanocrystals, such as the particle shape being twisted,[24, 25] or a twisted charge distribution.[2] However, the true mechanism has yet to be established. Since only chiral molecules (those lacking inversion symmetry) can give rise to a nematic phase, CNXL must to either the C_n or D_n point groups. Compounds in the C_n point group have exactly one C_n axis and nothing more, while compounds in the D_n point group contain the same C_n axis and nC_2 axes perpendicular to it. The rules for symmetry grouping confine the shape of the crystals to virtually perfect cylinders if they are going to exist in the nonpolar D_n point group. Therefore, if twisting of the crystal structure, twisting of charged groups, or edge imperfections exits, the perpendicular nC_2 axes required by the D_n point group are absent and the presence of a permanent-dipole is possible.

6.7. Field Dependence of the Rise Time

The rise times were determined by fitting the same curves used for the concentration analysis. Unlike the decay, the rise of the birefringent response fits best to a single exponential function. The resulting rise constants were plotted as a function of E^2 and are displayed in **Figure 6.7**.

In all cases the rise times appear proportional to the square of the field strength. The linear response of the rise times as a function of E^2 is in excellent agreement with the earlier assessment of the alignment mechanism which suggests a response driven mostly by the induced-dipole moment of the crystals. There does appear to be an increase of the slope with concentration, which would suggest a small influence from inter-particle attractions. However, no such response was seen in the decay fittings so the exact cause of the decreased rise times is unclear.

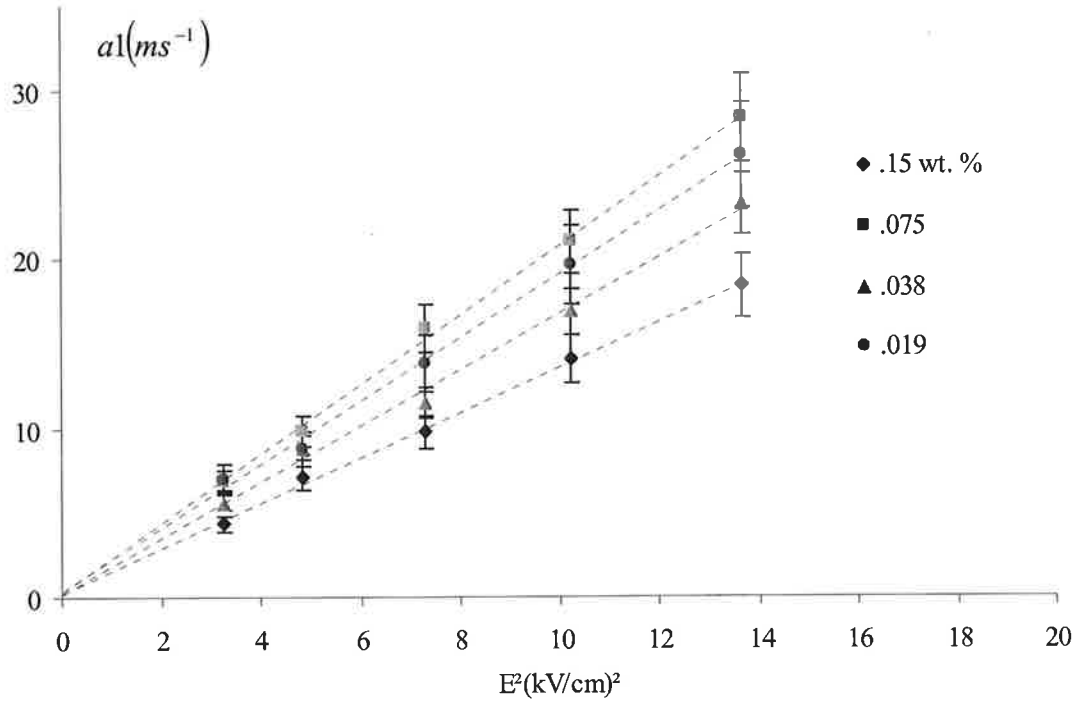

Figure_6.7: Rise constants for cellulose samples at varying concentrations and field strengths. All concentrations show a linear dependence on the squared field strength with a small increase in the slope with concentration.

Linear fits of the rise curves were used with Eq. **(4.62)** and Eq. **(4.63)** to calculate the polarizability anisotropy. **Table 6.3** gives average results for the range of field strengths at each concentration. The result obtained here for the polarizability anisotropy has a difference of ~11% when compared with that from saturation analysis. The discrepancy can be easily accounted for by recognizing an earlier assumption that was made in the derivation of the rise time with regard to field dependence. Specifically, any permanent dipole in the particle is directed perpendicular to the principal symmetry axis. This assumption simplified the model of the rise time by retaining inversion symmetry in the particle. However, the theory becomes inappropriate for this situation when a dipole is present with a projection along the symmetry axis.

Table 6.3: Average polarizability anisotropies as calculated using the rise times at varying field strengths.

% wt.	**$\Delta\alpha$ x 10^{-31} (Fm^2)**	**$\Delta\alpha'$ x 10^{-15} (Fm^2)**
0.15	5.80 ± 1.24	5.19 ± 1.11
0.075	6.59 ± 1.97	5.90 ± 1.76
0.038	7.01 ± 2.04	6.27 ± 1.82
0.019	7.42 ± 2.23	6.64 ± 2.00
	6.71 ± 1.87	**6.00 ± 1.67**

For curiosity's sake, we can extend the discussion further by recalculating the polarizability anisotropy using the saturation method. We would like to compare the two methods of deriving the polarizability anisotropy, by assuming that the CNXL has a negligible permanent dipole in both methods. We can recalculate $P + Q$ using the saturation method but this time, P = 0:

$$P = 15\frac{n^2 K_{sp}}{2\pi\Delta g}$$

Substituting in the relation $Q = \Delta\alpha/kT$, in addition to multiplying both sides of the equation by kT, then yields:

$$\Delta\alpha = 15\frac{n^2 K_{sp}}{2\pi\Delta g}kT = 15\frac{(1.33)^2(1.45x10^{-12})}{(2\pi)(3.55x10^{-2})}4.14x10^{-21} = 7.16x10^{-31}\,Fm^2$$
$$= \frac{10^6}{4\pi\varepsilon_o}7.16x10^{-31}\,Fm^2 = \underline{\underline{6.40x10^{-15}\,cm^3}}$$

It can be seen from the resulting value that the agreement between the two methods is now much better, with a difference of only ~6%. The resulting improvement in the percent difference between the two methods suggests that the rise time analysis actually gives a result which is a combination of both the permanent and induced-dipoles. Thus, by treating the saturation analysis as induced dipole only, we have a method to directly compare results from two different types of measurements.

The above agreement is in stark contrast to the large discrepancy that was observed with the clay sample. However, the difference in values of $\Delta\alpha$ for clay was

attributed to polydispersity in shape, with different shaped particles dominating different measurements (disks in the rise time analysis and rods in the saturation analysis). For the case of cellulose crystallites, only the particle size varies, while the shape is uniform and the rod model can be clearly defined.

6.8. Birefringent Response to Pulsed AC Fields

The response of a .15 % wt CNXL sample to a .67 kV/cm, pulsed AC field of varying frequency is shown in **Figure 6.8**. The signal at 2 kHz oscillates appreciably with the field, almost reaching a zero value in the region where the pulsed AC field approaches zero. A similar trend can be seen when the frequency of the field is doubled. However, this time more of the steady state component is observed. By the time the frequency is increased to 200 kHz, the oscillating behavior of the sample has disappeared and the signal responds as if it's been subject to a 500 μs DC pulse.

For CNXL, we expected to see the effects of both a permanent and induced-dipole at low frequencies, even though the permanent-dipole contribution is small (~5%). However, the cause of the oscillation is questionable due to the signal not reaching saturation. The oscillation could be attributed to the permanent dipole following the change in field or simply, the faster relaxation times of the cellulose crystals.

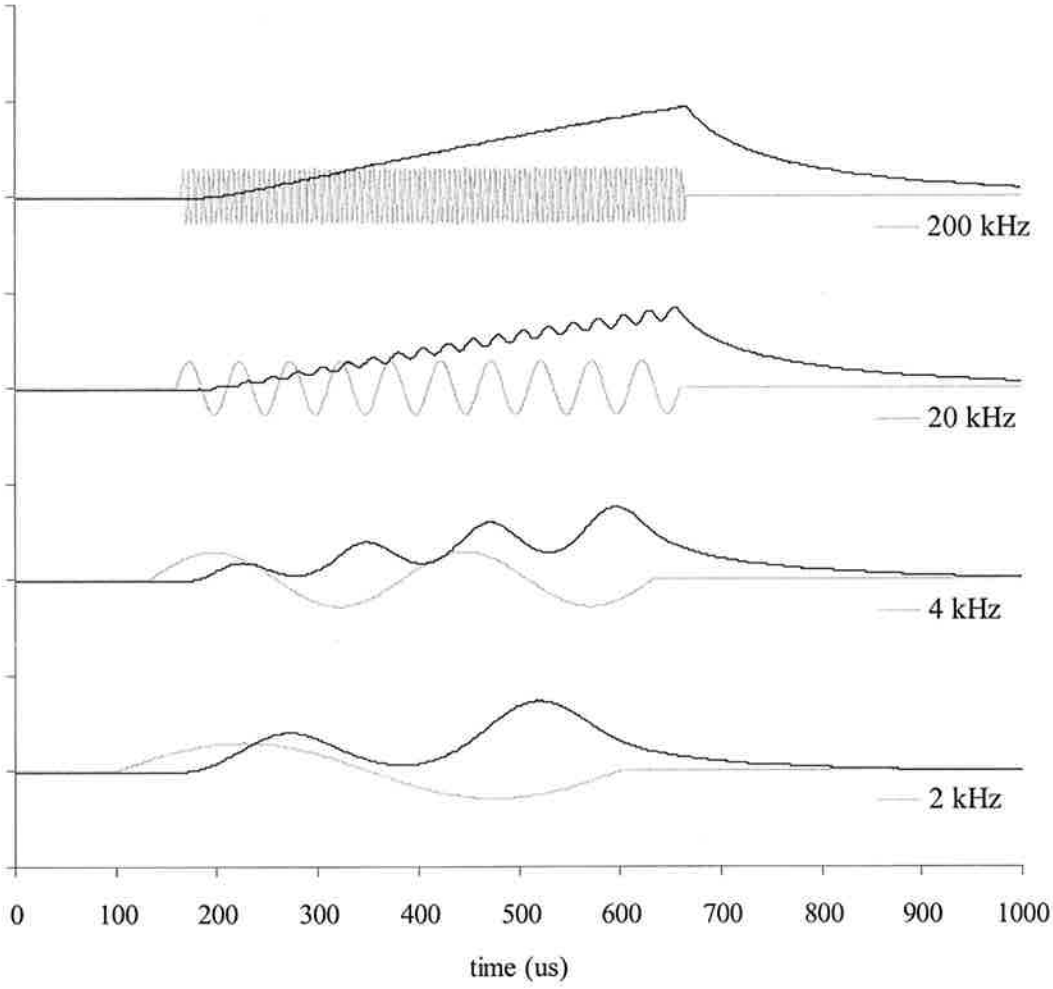

Figure 6.8: Response of a .15 %wt CNXL sample subject to a .67 kV/cm, pulsed AC field of varying frequency.

6.9. References

1. Dong, X.M., J.-F. Revol, and D.G. Gray, *Effect of microcrystallite preparation conditions on the formation of colloid crystals of cellulose.* Cellulose (London) , 1998. **5**(1): p. 19-32.

2. Revol, J.F., et al., *Helicoidal self-ordering of cellulose microfibrils in aqueous suspension.* Int. J. Biol. Macromol. , 1992. **14**(3): p. 170-2.

3. International, A., *ASM Handbook.* 10th ed. Vol. 2. 1990, Metals Park, OH: AMS International. 1328.

4. Peters, D.M., J.W. Weeton, and K.L. Thomas, *Engineers' Guide to Composite Materials*. 1987: Asm Intl.

5. Oksman, K., D. Bondeson, and P. Syre, *Nanocomposites based on cellulose whiskers and cellulose plastics*. 2008, (Ntnu Technology Transfer AS, Norway). Application: US. p. 13pp.

6. Eichhorn, S.J., *Regenerated cellulose reinforced plastics.* Nat. Fibers, Plast. Compos. , 2004: p. 287-303.

7. Hadano, S., et al., *Synthesis of biodegradable cellulose plastics having poly(L-lactic acid) graft chains.* Kobunshi Ronbunshu , 2003. **60**(9): p. 454-461.

8. Kurokawa, Y., *Ceramics obtained from mixed cellulose derivative-alkoxide gels, and their manufacture*. 1995, (Shingijutsu Kaihatsu Jigyodan, Japan). Application: JP
JP. p. 3 pp.

9. Hoepfner, P., *Cellulose ethers in ceramics.* Ber. Dtsch. Keram. Ges., 1968. **45**(3): p. 103-7.

10. Reveley, A., *Methyl cellulose in ceramics and refractories.* Refract. J., 1963. **39**(9): p. 372-3.

11. Panzer, D., *Use of cellulose ether for producing a medical lubricant*. 2001, (Germany). Application: WO. p. 16 pp.

12. Radovich, J.M., M. Rothberg, and G. Washington, *Improved process for making cellulose acetate semipermeable membranes and medical products therefrom*. 1996, (Althin Medical Inc., USA). Application: EP. p. 8 pp.

13. Ikada, Y., *Biomedical applications of cellulose membranes.* Cellulose, 1990: p. 447-55.

14. Shoemaker, D.P., C.W. Garland, and J.W. Nibler, *Experiments In Physical Chemistry*. 6th ed. 1996: McGraw-Hill. 778.

15. Lima, M. and R. Borsali, *Static and Dynamic Light Scattering from Polyelectrolyte Microcrystal Cellulose.* Langmuir, 2002. **18**: p. 992-996.

16. Dhara, S., et al., *Kerr constant and third-order nonlinear optic susceptibility measurements in a liquid crystal composed of bent-shaped molecules.* Phys. Rev. E: Stat., Nonlinear, Soft Matter Phys. , 2008. **78**(5-1): p. 050701/1-050701/4.

17. Khoshsima, H., A. Ghanadzadeh, and H. Tajalli, *Kerr Effect of Low Melting Nematic Liquid Crystals with Negative Dielectric Anisotropy.* Liquid Crystals, 2006. **33**(6): p. 747-751.

18. Khoshsima, H., et al., *Kerr effect investigations in liquid crystals containing the isothiocyanato and cyano groups with identical flexible tails.* Mol. Cryst. Liq. Cryst. , 2006. **460**: p. 93-106.

19. Fleming, K., D.G. Gray, and S. Matthews, *Cellulose crystallites.* Chem.--Eur. J. , 2001. **7**(9): p. 1831-1835.

20. Araki, J., et al., *Flow properties of microcrystalline cellulose suspension prepared by acid treatment of native cellulose.* Colloids Surf., , 1998. **142**(1): p. 75-82.

21. Imai, T., et al., *Unidirectional processive action of cellobiohydrolase Cel7A on Valonia cellulose microcrystals.* , 1998. **432**(3): p. 113-116.

22. De Souza Lima, M.M., et al., *Translational and Rotational Dynamics of Rodlike Cellulose Whiskers.* Langmuir, 2003. **19**: p. 19-24.

23. Gray, D.G., *Chiral nematic ordering of polysaccharides.* Carbohydr. Polym. , 1994. **25**(4): p. 277-84.

24. Revol, J.F. and R.H. Marchessault, *In vitro chiral nematic ordering of chitin crystallites.* Int. J. Biol. Macromol. , 1993. **15**(6): p. 329-35.

25. Orts, W.J., et al., *Enhanced ordering of liquid crystalline suspensions of cellulose microfibrils: a small-angle neutron scattering study.* Macromolecules , 1998. **31**(17): p. 5717-5725.

7. CdSe Nanocrystals

7.1. Introduction

QDs are nanometer-scale atomic clusters, containing from a few hundred to a few thousand atoms of a semiconductor material (mixtures of periodic groups II-VI, III-V, and IV-VI), they are typically coated with an additional semiconductor shell (usually zinc sulfide) to improve their optical properties. In recent years, QDs have been the focus of many studies. In fact, a search of the phrase "quantum dots," returned 42,683 references. One property of rod shaped quantum dots which fueled the interest of this study is their emission of linearly polarized light. It is hypothesized here that, if the particles can be successfully aligned in a polymer or thin film, they could be used as a source of linearly polarized light for thin panel displays. This idea is addressed more in a later section on polymer composites.

Fundamentally, quantum dot nanocrystals are fluorophores; substances that absorb photons and then re-emit at a different wavelength. However, they exhibit some important differences from traditional fluorophores, such as organic fluorescent dyes. These differences stem from their size and chemical composition. For a QD, concepts of bandgap, conduction band and valence band, which govern the behavior of bulk materials, still apply. However, quantum confinement results in discrete energy levels and the material ceases to resemble those of the corresponding bulk. The quantum confinement has large repercussions on the absorptive and emissive behavior of the semiconductor material in that the addition or subtraction of just a few atoms has the effect of altering the boundaries of the bandgap. Changing the geometry

of the surface of the quantum dot also changes the bandgap energy, owing again to its small size. This property has been referred to as "tunability", and is being widely exploited in the development of multicolor assays by companies such as Invitrogen.

Quantum dots have a wide range of applications in both biological and material applications. Encapsulated within a layer of protective surfactant,[1, 2] QDs have been used as active components inside plastic electronics,[3-5] proposed as the foundation for a new class of LED,[6] and heavily used in the biomedical field for cell imaging and cancer research.[7-10] It has also been shown that rod shaped CdSe QDs spontaneously form liquid crystalline phases when dispersed in solvent at high concentration.[11] Thus, it is of great interest to use external electric and magnetic fields to align these liquid crystalline samples in order to manipulate their orientations on a large scale.

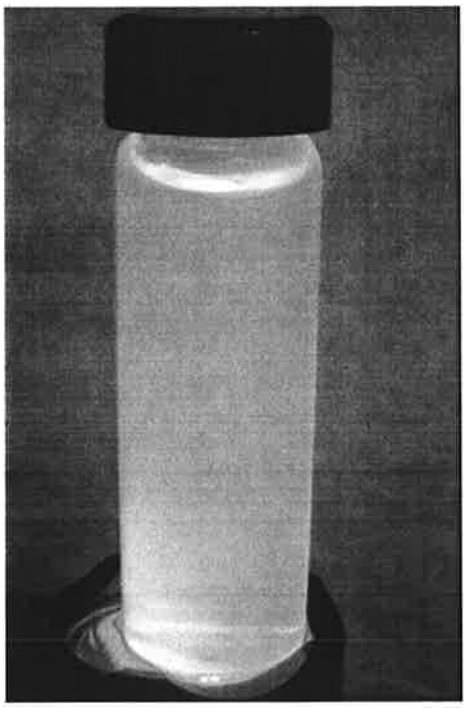

Figure 7.1: Aqueous quantum dots emitting 655 nm light under UV irradiation.

For this research, the focus will be on nanorods of CdSe because they have an anisotropic geometry and also exhibit excellent monodispersity.[12-14] Upon absorption of UV radiation, these nanorods will emit light at a wavelength of 655 nm. A 2 μM aqueous sample of carboxylated CdSe

quantum dots is displayed in **Figure 7.1**. The solution is being irradiated with 350 nm UV light and emission at 655 nm is clearly observable.

The nanorods are made by the reaction of organometallic precursors of Cd and Se in a hot surfactant mixture. By varying the composition of the surfactant, the rodlike CdSe nanocrystals can be tuned to varying widths and lengths.[14] The CdSe core is then coated with a ZnS shell, in order to minimize tunneling effects between the core and solvent, and to increase the quantum efficiency of emission. Finally, a polymer coating is added, for the attachment of biomolecules specific to the application. Typically, the aspect ratio of CdSe QDs can be varied from 1 to 15, with widths from 3 to 7 nm, and length from 3 to 70 nm. The distribution is typically 5% of the average value for width and 10% for length. A TEM image of the CdSe rods used for this study is shown in **Figure 7.2**; it illustrates the range and quality of the nanorods.

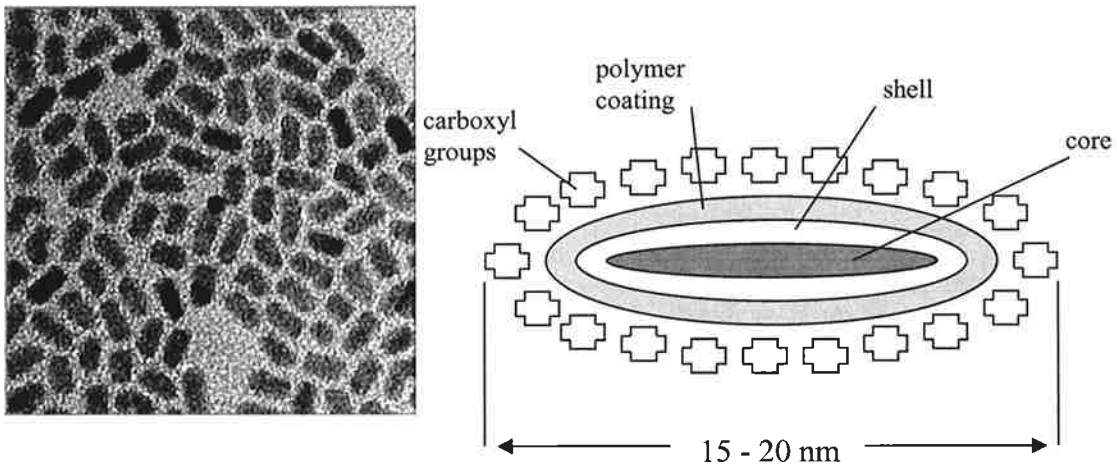

Figure 7.2: Transmission electron microscope image of core-shell Qdot® nanoparticles at 200,000x magnification and the schematic of the overall structure of a Qdot® conjugate. The layers represent the distinct structural elements of the Qdot® nanocrystal conjugates.

CdSe nanorods are typically functionalized with amphiphilic molecules, such that a polar functional group is bound to the nanocrystal surface, and a long alkyl chain projects outward. These alkyl chains provide high solubility of the nanorods in organic solvents. However, if the rods are to be used in water, the amphiphilic shell can be replaced with a shell of hydrophilic nature. The quantum dots used herein are functionalized with carboxyl groups.

7.2. Analysis Overview and Experimental

CdSe nanocrystals (Qdot® ITK™ 655 carboxyl quantum dots) were used as supplied by Invitrogen and the sample parameters are listed in **Table 7.1**. Sample solutions were prepared from the 16 μM stock solution by the direct addition of deionized water.

Table 7.1: Specific physical properties of the CdSe QD sample supplied by Invitrogen.

Concentration (μM)	density (g/cm^3)	Particle length (nm)
16.0	15.58	15 – 20 90%
		≥ 20 <10%

The analysis of the QD samples will be separated into four parts. The following section outlines each analytical technique, the associated physical property, and how that property will be used to characterize the sample:

1) **Concentration dependence of the decay mechanism** will be followed in order to determine the sample's percolation threshold. Once a suitable concentration range has been established, the rotational diffusion coefficient D_R will be calculated from the decay constants and used to determine particle dimensions.
2) **Saturation of the birefringent response** Δn will be studied as a function of the field strength, and information thus obtained will entail:
   - Optical anisotropy Δg
   - Specific Kerr constant K_{sp}
   - Orientation mechanism i.e. the ratio of permanent to induced-dipole moment
   - Single particle polarizability anisotropy $\Delta\alpha$
   - Single particle dipole moment μ
3) **Field dependence of the rise time** will be followed to further elucidate the orientation mechanism (induced-dipole and/or permanent-dipole) and to derive the single particle polarizability anisotropy.
4) **Pulsed AC trials** will be conducted as a supplemental study to further confirm the alignment mechanism.

7.3. Concentration Dependence of D_R

The concentration trials were run in order to determine the percolation threshold for the quantum dots. An increase in concentration results in a decrease in the inter-particle distance and inter-particle interactions occur due to space limitations. With increasing field strength the order within the system will also increase. The easiest method for determining a threshold concentration is to follow the diffusion of the particles as a function of field strength and concentration. If inter-particle interactions are present, both factors will have an observable effect on the diffusion constant D_R.

Following the procedure described for the clay sample, field strength trials were run on QD samples ranging from 1.6 to .1 μM, and the decay curves were fit using the double exponential expression represented by Eq. **(4.71)**. The results for a fast and slow rotational diffusion coefficient D_R as a function of field strength were determined to be $D_R = 13062 \pm 1511\ s^{-1}$ and $D_R = 1295 \pm 320\ s^{-1}$. However, the difference between the amplitudes of the two exponential functions is approximately three orders of magnitude; with values for D_R(fast) and D_R(slow) of .001 and .999, respectively. In order to determine if preference could be given to the biexponential model, an F-test was performed using the χ^2 values from each fitting. A limiting value of $F \approx 3.84$ at a 95% confidence level was taken from the available tables.[15] Given that the decay curves consisted of ~1000 data points and that two and four adjustable parameters were involved in the fitting, the value of F for the given chi squared values was:

$$F = \frac{\chi^2_{\nu 1}}{\chi^2_{\nu 2}} = \frac{\chi^2_1/(1000-2)}{\chi^2_2/(1000-4)} = \frac{.021^2/998}{.012^2/996} = 3.05$$

Hence, single exponential fit is a more appropriate model for the system, even though the χ^2 is larger, because the calculated F value does not exceed the limiting value of 3.84.

The origin of the single exponential fitting function can be attributed to the highly symmetric nature of the nanocrystals. According to Ridgeway, as detailed in **Section 4.9,** when the asymmetry of an asymmetric ellipsoid diminishes, the biexponential decay converges into a single exponential, and one of the amplitudes approaches zero. In the case of CdSe quantum dots, as seen from the TEM pictures, the two axes orthogonal to the long axis of the rod are essentially indistinguishable.

The values for D_R as a function of E^2 can be seen in **Figure 7.3**. A slight increase is observed with samples of relatively higher concentrations, however, the values are essentially constant over the range of applied field strengths. Based on these results, we chose the 1.6 μM concentration for further study. This choice was to maximize the signal to noise ratio in the birefringent response. The length of the rods was calculated using Eq. **(4.68)** assuming a ratio L/a = 4, a value provided by Invitrogen and our own TEM images. The results are presented in **Table 7.2**.

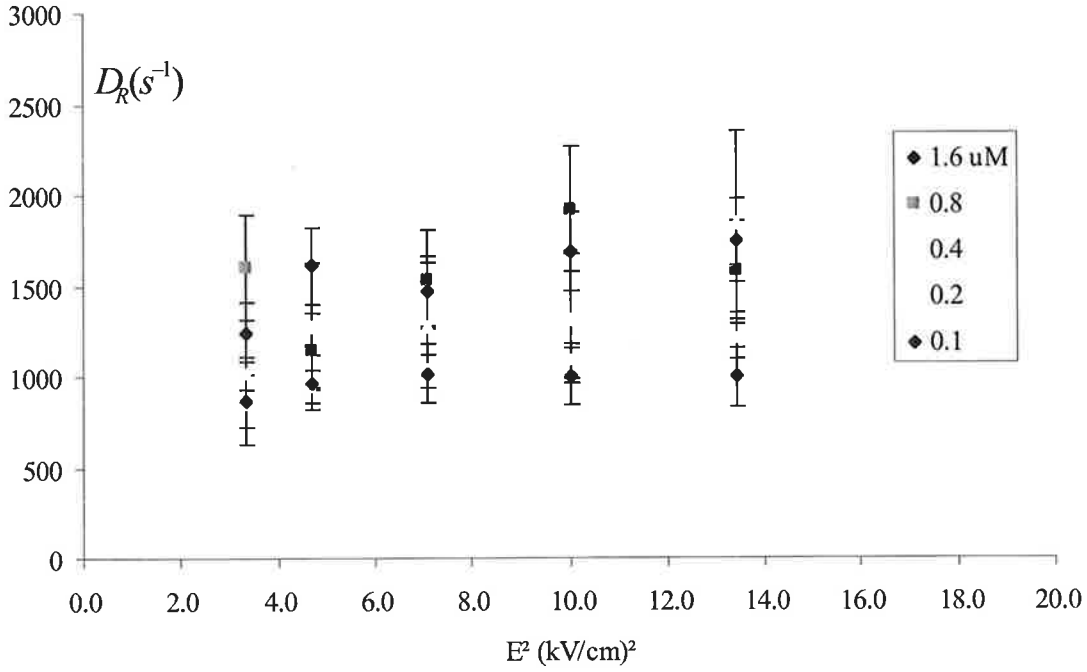

Figure 7.3: Rotational diffusion coefficients D_R for Qdot® nanoparticles at vary squared field strengths as a function of concentration.

The calculated lengths are in excellent agreement with those reported in the literature and the information supplied by Invitrogen. As measured, the nanorods are coated with a polymer shell and then carboxyl groups; and these additional layers have brought the average length of the nanorods from 12 nm, for just the core, up to 16 nm.

Table 7.2: Values for the rotational diffusion D_R coefficient and diameter for CdSe quantum dots varying fields and concentrations.

μM	D_R (s^{-1})	rod length (nm)	rod diameter (nm)
.16	1553 ± 200	15.28 ± .7	3.82 ± .18
.08	1556 ± 275	15.3 ± .9	3.83 ± .24
.04	1316 ± 352	16.3 ± 1.5	4.08 ± .37
.02	1055 ± 96	17.3 ± .5	4.34 ± .13
.01	970 ± 60	17.8 ± .4	4.46 ± .10
	1290 ± 323	**16.4 ± 1.3**	**4.10 ± .34**

7.4. Saturation of the Birefringent Response at Low Fields

The birefringent responses for a 1.6 μM quantum dot sample subject to fields between .02 and 1.5 kV/cm were recorded after averaging over 128 pulses at 2 Hz, with a pulse width of 500 μs. The change in birefringence Δn at each field strength was calculated according to Eq. **(3.35)** for an optical arrangement with a quarter-wave plate. The value for $\Delta n/E^2$ where $E \rightarrow 0$ was determined to be 1.99×10^{-9} cm^2kV^{-2}. When combined with Eq. **(4.28)**, the specific Kerr constant K_{sp} is calculated as follows:

$$K_{sp} = \frac{1.99x10^{-9}\,cm^2kV^{-2}}{(2.03x10^{-7})(1.33)} = 7.34x10^{-3}\,cm^2kV^{-2}$$

$$= \underline{\underline{7.34x10^{-13}\,m^2V^{-2}}}$$

7.5. Saturation of the Birefringent Response at High Fields

Extrapolation of the birefringence to infinite field gives a saturation value for the birefringence of $\Delta n_s = 1.17\text{x}10^{-8}$ and results in an optical anisotropy of:

$$\Delta g = \frac{\Delta n_s n}{2\pi C_v} = \frac{(1.17x10^{-8})(1.33)}{2\pi(2.03x10^{-7})} = 1.21x10^{-2}$$

The determination of the ratio of permanent to induced-dipole moment in the quantum dots was carried out using the plot in **Figure 7.4** of $\Delta n/E^2$ vs. $logE^2$, normalized to its low field limit. The slope of -0.60 at intermediate field strengths, when combined with Eq. **(4.26)**, results in an estimated contribution of $[.88\beta^2 + .12(2\gamma)]$ toward the alignment mechanism from the permanent and induced-dipoles in the nanoparticles.

A horizontal shift of 0.47 was necessary to align the experimental data with the theoretical curve. This procedure was first used in **Section 6.6** when a shift was necessary to determine the dipole in cellulose nanocrystals. It uses the logarithmic relation in Eq. **(4.30)** that results from the graph of the normalized data as a function of $logE^2$, seen in Figure 11.5, as follows:

$$\log(P+Q) + \log E^2 = 0.61 + \log E^2$$

$$\log(P+Q) = 0.47$$

$$P+Q = 2.95x10^{-10}\, m^2V^{-2}$$

where P, the permanent-dipole term, is $P = \beta^2/E^2 = \mu^2/k^2T^2$ and Q, the induced-dipole term is $Q = 2\gamma/E^2 = \Delta\alpha/kT$.

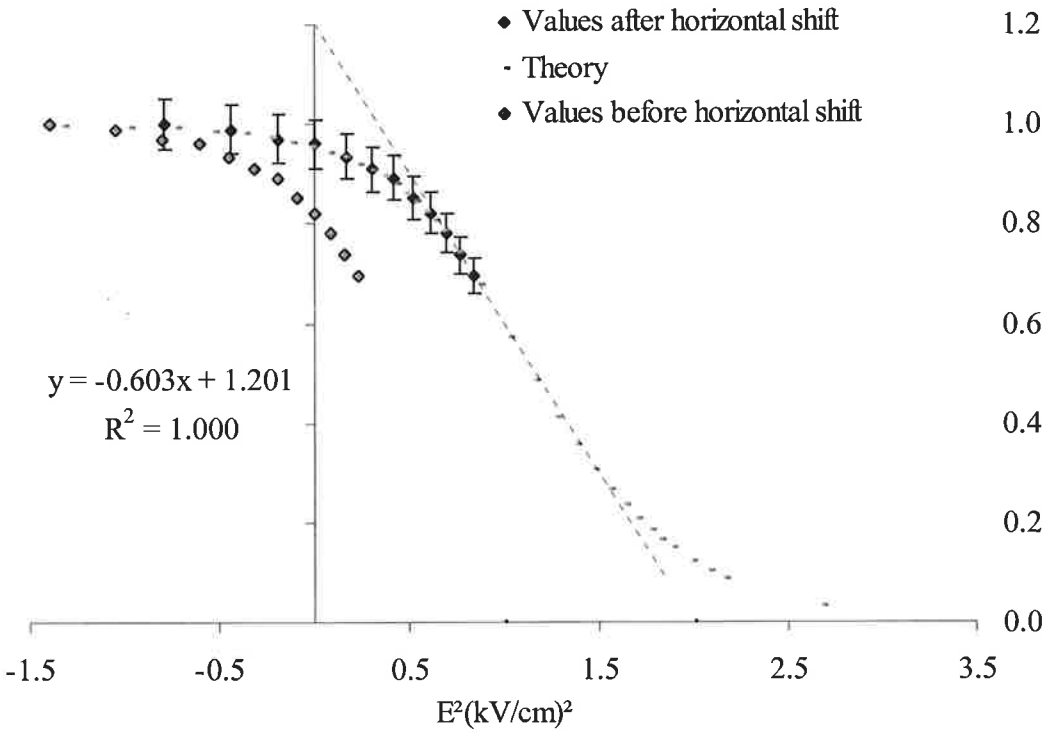

Figure 7.4: Normalized plot of $\Delta n/E^2$ vs. $logE^2$ for a quantum dot sample laid over the theoretical curve for an alignment mechanism represented by the ratio $[.87\beta^2 + .12(2\gamma)]$.

The polarizability anisotropy $\Delta\alpha$ and permanent dipole moment μ of the quantum dots may now be obtained from **(65)** as follows:

$$P = 2.95x10^{-10}\,m^2V^{-2} - Q \qquad [.88P + .12Q] = \frac{15K_{sp}n^2}{2\pi\Delta g}$$

$$[.88(2.95x10^{-10}\,m^2V^{-2} - Q) + .12Q] = \frac{15(7.34x10^{-13}\,m^2V^{-2})(1.33)^2}{2\pi(1.21x10^{-2})}$$

$$3.58x10^{-10}\,m^2V^{-2} - .64Q = 2.55x10^{-10}\,m^2V^{-2}$$

$$Q = 5.85x10^{-12}\, m^2V^{-2} \qquad P = 2.89x10^{-11}\, m^2V^{-2}$$

$$\frac{\Delta\alpha}{k_BT} = 5.85x10^{-12}\, m^2V^{-2} \qquad \frac{\mu^2}{k_B^2T^2} = 2.89x10^{-11}\, m^2V^{-2}$$

$$\Delta\alpha = 2.42x10^{-32}\, Fm^2 \qquad \mu = 7.04x10^{-27}\, Cm$$

$$\Delta\alpha' = 2.17x10^{-14}\, cm^3 \qquad \mu = 2.11x10^{3}\, D$$

7.6. Field Dependence of the Rise Time

The rise times were determined by fitting the same data used for the concentration analysis. Unlike the decay, the rise of the birefringent response fits best to a single exponential function. The resulting rise constants were plotted as a function of E^2 and are displayed in **Figure 7.5**.

In all cases the rise times appear proportional to the square of the field strength. The linear response of the rise times as a function of E^2 is somewhat counterintuitive. Given that the quantum dots are shown to possess a large dipole moment, it would seem reasonable to expect them to show a linear dependence on E at low fields. However, the E^2 response of the induced moment seems to govern the response, even down to the lowest fields used in this study.

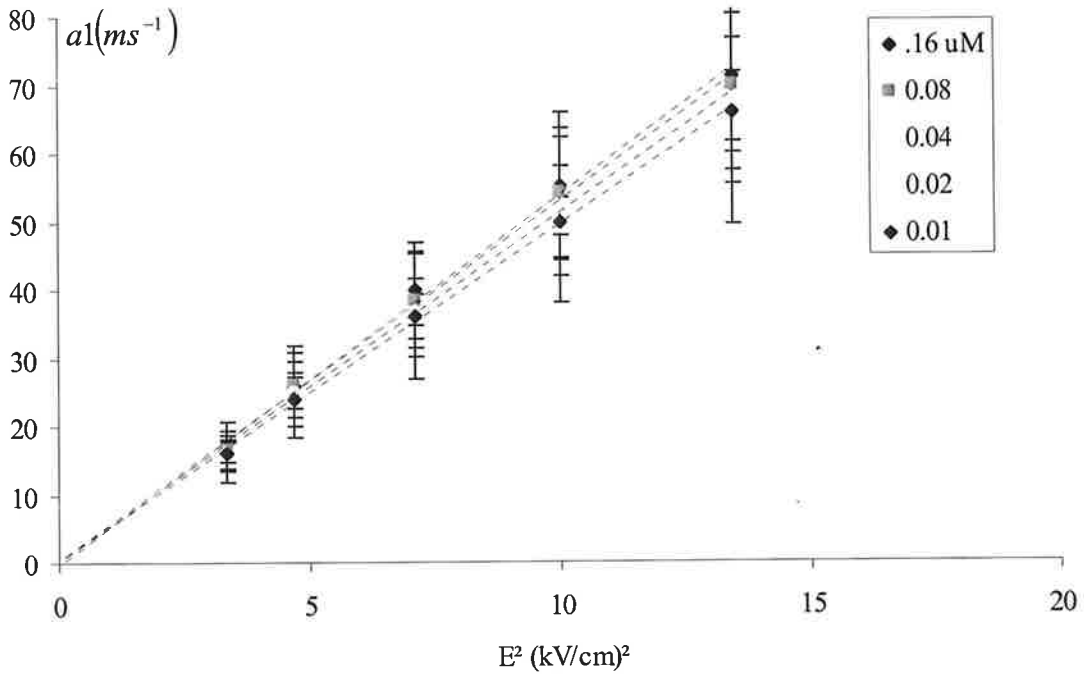

Figure 7.5: Rise constants for quantum dot samples at varying concentrations and field strengths. All concentrations show a linear dependence on the squared field strength.

Linear fits of the rise curves were used with Eq. **(4.62)** and Eq. **(4.63)** to calculate the polarizability anisotropy. **Table 7.3** gives average results for the range of field strengths at each concentration.

The result obtained here for the polarizability anisotropy is approximately two orders of magnitude larger than that from the saturation analysis ($\Delta\alpha = 2.42x10^{-32}\,Fm^2$). This is a much larger difference than that from the two methods in the earlier discussion on CNXL in **Section 6.7**, where the value for $\Delta\alpha$ varied by only 11%. However, the reader will recall the discussion which highlighted

the fact that the rise time analysis does not separate the permanent and induced-dipoles and so both dipoles are represented by an equivalent value of $\Delta\alpha$. In the case of CNXL, the permanent-dipole's contribution was only 5% and so the difference was small. In the case of QDs, the permanent-dipole makes up 88% of the observed birefringent response and so the disparity between the two methods is much greater.

Table 7.3: Average polarizability anisotropies as calculated using the rise times at varying field strengths.

µM	**$\Delta\alpha$ x 10^{-30} (Fm^2)**	**$\Delta\alpha'$ x 10^{-14} (cm^3)**
1.6	1.23 ± .25	1.10 ± .12
.8	1.30 ± .24	1.16 ± .14
.4	1.18 ± .16	1.06 ± .08
.2	1.17 ± .07	1.05 ± .06
.1	1.13 ± .16	1.01 ± .08
	1.20 ± .19	**1.08 ± .10**

Since QD is the only sample in this thesis that has well characterized mono-dispersity, it is worthwhile to make some more detailed investigations. We would like to compare the two methods of deriving the polarizability anisotropy, by assuming that the QDs have a negligible permanent dipole in both methods. We can recalculate $P + Q$ using the saturation method but this time, P = 0:

$$\Delta\alpha = 15\frac{n^2 K_{sp}}{2\pi\Delta g}kT = 15\frac{(1.33)^2(7.34x10^{-13})}{(2\pi)(1.21x10^{-2})}4.14x10^{-21} = 1.06x10^{-30}\,Fm^2$$
$$= \frac{10^6}{4\pi\varepsilon_o}7.16x10^{-31}\,Fm^2 = \underline{\underline{9.45x10^{-15}\,cm^3}}$$

This value agrees with the result from the saturation analysis to within 12%. Thus, the "equivalent polarizability" obtained from both methods do agree.

7.7. Birefringent Response to Pulsed AC Fields

The response of a .8 μM CdSe quantum dot sample to a .67 kV/cm, pulsed AC field of varying frequencies is shown in **Figure 7.6**. This result is markedly different from those of other samples. In each of the previous cases, the eventual loss of the alternating component of the birefringent signal was observed once the field frequency exceeded 20 kHz. In the case of the quantum dots, the AC component persists up to 200 kHz.

Another observation unique to the quantum dot is the saturation of the birefringence at all frequencies. This was possible because, unlike the clay and CNXL samples, the rise time for the alignment of the QDs was fast enough that saturation

could be achieved during the pulse duration. In an earlier discussion, it was mentioned that if signal saturation is achieved in an AC field, relaxation of alignment may play a minimal part in decreased birefringence, and oscillatory behaviors can be contributed primarily to the presence of a dipole in the particles.

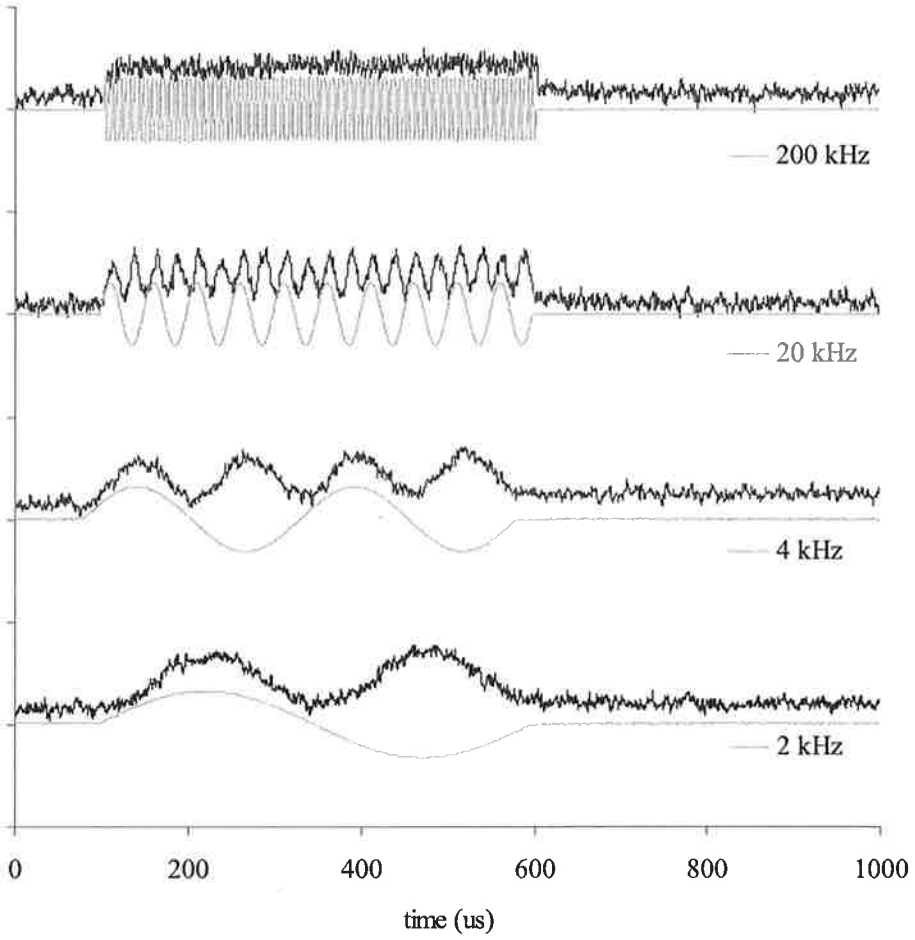

Figure 7.6: Response of a .8 μM quantum dot sample, subject to a .67 kV/cm, pulsed AC field of varying frequency.

Of course, even if saturation is achieved at the peak of the field, it is definitely not achieved when the field changes sign, so relaxation will have some contribution. However, if we look at the average birefringence, we can compare it to what is predicted by the ratio of permanent to induced-dipoles per Eq. **(4.75)** and determine if the calculated values for μ and $\Delta\alpha$ are consistent with the AC response.

Thus, taking the values of $\mu = 6.83x10^{-26}\,Cm$ and $\Delta\alpha = 5.61x10^{-31}\,Fm^2$ determined from the saturation analysis, an approximation of the observed birefringence at the highest applied frequency goes as follows:

$$\Delta n_{st\infty} = \Delta n_o\left(\frac{1}{1+P/Q}\right) = \Delta n_o\left(\frac{1}{1+.49}\right) = .67\Delta n_o$$

where $$P/Q = \frac{\mu^2}{\Delta\alpha kT} = \frac{(7.04x10^{-27})^2}{(2.42x10^{-32})4.14x10^{-21}} = .49$$

The response of the quantum dots to the 2 and 200 kHz AC fields can be seen in **Figure 7.7**, where both curves have been normalized to that of the 2 kHz response, so that the relation $\Delta n_{st\infty} = .67\Delta n_o$ is clearly visible. The decrease in the steady state at 200 kHz (green) confirms the calculation of the permanent dipole and polarizability anisotropy in the saturation analysis.

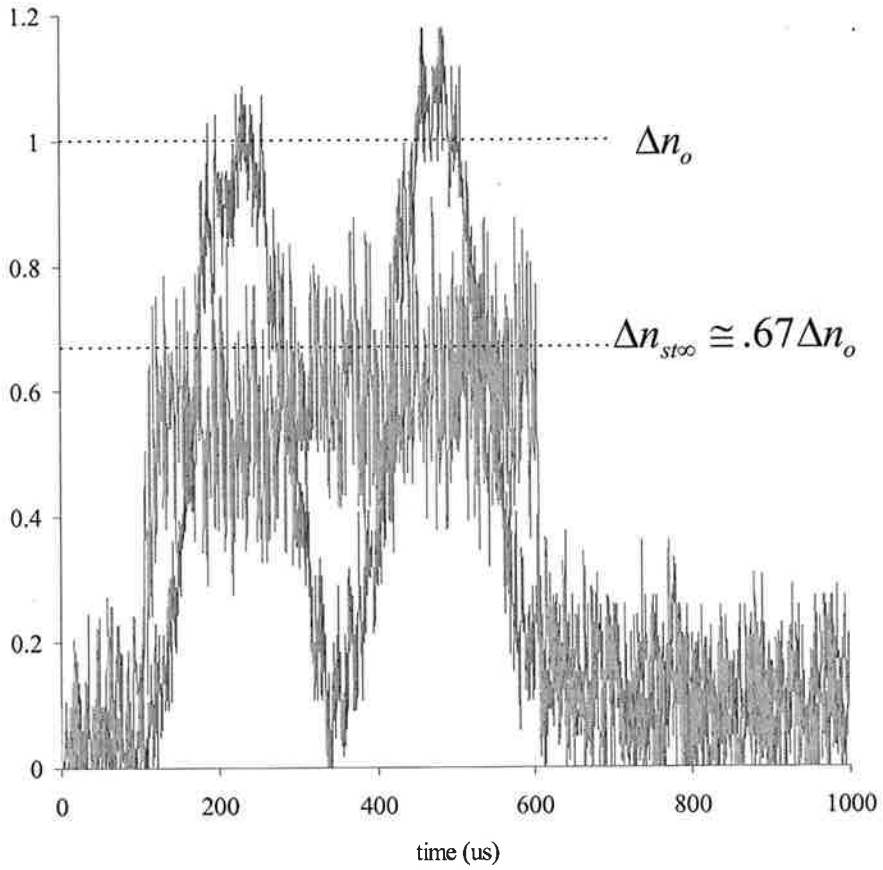

Figure 7.7: Response of a .8 μM quantum dot sample, subject to a .67 kV/cm, pulsed AC field at 2 kHz (blue) and 200 kHz (green).

7.8. Discussion of Dipole

There have been many detailed theoretical and experimental studies on the electronic properties of CdSe quantum dots. A still unresolved question concerns the origin of a dipole moment in these nanocrystals; a question that has spurred somewhat contradictory results.[17-20] Unlike other types of quantum dots such as the III-V dots grown by molecular beam epitaxy,[16] colloidal CdSe (II-VI) dots have a wurtzite hexagonal structure with no inversion center. In some cases, the dipole moment has been attributed to the lack of inversion symmetry in hexagonal nanocrystals, or from charges localized on the surface. A close examination of the structure of $Cd_{83}Se_{81}$ through numerical calculations by Rabani et al revealed that it is highly symmetric along the *z* direction, having a plane of symmetry for Cd atoms and for Se atoms separately. Consequently, the dipole of each unit cell of the hexagonal crystal structure adds up to result in a macroscopic dipole moment.[17] The same was shown to be true for other combinations. However, there were also cases, such as $Cd_{68}Se_{69}$ and $Cd_{232}Se_{251}$, where it appeared that there are some structural cancellations which decrease the dipole moment along the *z* direction. The primary difference between the varying combinations was the center atom of the lattice structures, i.e. Se-centered or cell-centered. Thus small changes in the crystal structure can have a significant influence on the particles' observed dipole.

Unfortunately, the exact structure of a specific batch of QDs is very difficult to control. The particles are made at high temperature (~315°C) and the initial "seeding" process occurs very quickly once the precursors are injected into the reaction mixture.

Even the most subtle differences in temperature, precursor concentrations, or injection time of the reagents can influence the resulting lattice structure. In some cases the lattice will be Se-centered and in others it will be cell-centered.

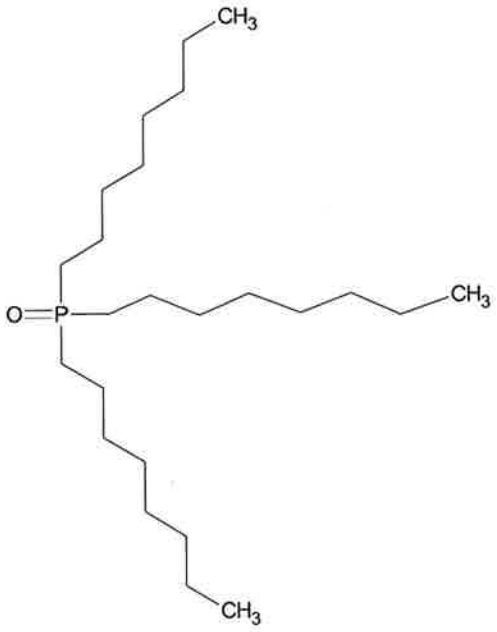

Figure 7.8: Structure of trioctylphosphine oxide (TOPO)

The dipole moment calculated here for the CdSe nanocrystals is approximately one order of magnitude larger than the value of 209 ± 32 *D* reported recently by Liang-shi and Alivisatos.[21] In their study, TEB measurements were taken on CdSe nanorods with an average dimension of 5 by 26 nm dispersed in cyclohexane. The nanorods were coated with organic ligands such as trioctylphosphine oxide (TOPO) so that they were stable in the non-polar solvent. The large hydrocarbon tails of the TOPO molecules (**Figure 7.8**) extend out from the quantum dot core with no surface charges. In contrast, the quantum dots used in the current study were functionalized with carboxyl groups so that they would be stable in an aqueous solution. For these QDs, both an interfacial polarizability, due to the movement of hydronium ions, and charged surface groups, contribute to the interfacial polarizability and dipole, respectively. In the case of the permanent-dipole, any uneven distribution of charged surface groups will have a significant effect on its measured value.

Rabani el al also addressed solvent effects when they reported the electronic properties of the nanocrystals in dielectric media.[17] Their calculations and results showed a dependence of the first and second moments of the charge density on the dielectric constant ε outside the nanocrystal, and that the dipole-moment could as much as double with increasing ε for the crystals they studied. This could also be a contributing factor to the large difference between the dipole moment reported here and those by Liang-shi and Alivisatos, as cyclohexane has a dielectric constant of ε = 2, while water has a value of ε = 88. It is clear that the moment depends strongly on the detailed structure of the nanocrystal and may vary significantly with small structural changes. Thus, in summary, the differences in the nanocrystal surface ligands, solvents, and possible lattice variation, could account for the large difference between the observed dipoles between this study and that of Liang-shi et al. [21]

7.9. References

1. Steigerwald, M.L., et al., *Surface derivatization and isolation of semiconductor cluster molecules.* J. Am. Chem. Soc. , 1988. **110**(10): p. 3046-50.

2. Schmid, G., *Large clusters and colloids. Metals in the embryonic state.* Chem. Rev. , 1992. **92**(8): p. 1709-27.

3. Colvin, V.L., M.C. Schlamp, and A.P. Allvisatos, *Light-emitting diodes made from cadmium selenide nanocrystals and a semiconducting polymer.* Nature (London) , 1994. **370**(6488): p. 354-7.

4. Dabbousi, B.O., et al., *Electroluminescence from CdSe quantum-dot/polymer composites.* Appl. Phys. Lett. , 1995. **66**(11): p. 1316-18.

5. Huynh, W.U., X. Peng, and A.P. Alivisatos, *CdSe nanocrystal rods/poly(3-hexylthiophene) composite photovoltaic devices.* Adv. Mater. (Weinheim, Ger.) , 1999. **11**(11): p. 923-927.

6. Tesster, N., et al., *Efficient near-infrared polymer nanocrystal light-emitting diodes.* Science (Washington, DC, U. S.) , 2002. **295**(5559): p. 1506-1508.

7. Wu, F. and J. Cai, *Applications of quantum dots in cancer research.* Jiguang Shengwu Xuebao , 2007. **16**(6): p. 800-804.

8. Orndorff, R.L. and S.J. Rosenthal, *Neurotoxin Quantum Dot Conjugates Detect Endogenous Targets Expressed in Live Cancer Cells.* Nano Lett. 9. Ko, M.H., et al., *In vitro derby imaging of cancer biomarkers using quantum dots.* Small , 2009. **5**(10): p. 1207-1212.

10. Chang, S.-q., et al., *UV-enhanced cytotoxicity of thiol-capped CdTe quantum dots in human pancreatic carcinoma cells.* Toxicol. Lett. , 2009. **188**(2): p. 104-111.

11. Li, L.-s., et al., *Semiconductor Nanorod Liquid Crystals.* Nano Lett. , 2002. **2**(6): p. 557-560.

12. Peng, X., et al., *Shape control of CdSe nanocrystals.* Nature (London) , 2000. **404**(6773): p. 59-61.

13. Peng, Z.A. and X. Peng, *Mechanisms of the Shape Evolution of CdSe Nanocrystals.* J. Am. Chem. Soc. , 2001. **123**(7): p. 1389-1395.

14. Hu, J., et al., *Linearly polarized emission from colloidal semiconductor quantum rods.* Science , 2001. **292**(5524): p. 2060-3.

15. Shoemaker, D.P., C.W. Garland, and J.W. Nibler, *Experiments In Physical Chemistry*. 6th ed. 1996: McGraw-Hill. 778.

16. Leon, R., et al., *Spatially resolved visible luminescence of self-assembled semiconductor quantum dots.* Science (Washington, D. C.) , 1995. **267**(5206): p. 1966-8.

17. Rabani, E., et al., *Electronic properties of CdSe nanocrystals in the absence and presence of a dielectric medium.* J. Chem. Phys. , 1999. **110**(11): p. 5355-5369.

18. Huong, N.Q. and J.L. Birman, *Origin of polarization in polar nanocrystals.* J. Chem. Phys. , 1998. **108**(5): p. 1769-1772.

19. Blanton, S.A., et al., *Dielectric dispersion measurements of CdSe nanocrystal colloids: observation of a permanent dipole moment.* Phys. Rev. Lett. , 1997. **79**(5): p. 865-868.

20. Shim, M. and P. Guyot-Sionnest, *Permanent dipole moment and charges in colloidal semiconductor quantum dots.* J. Chem. Phys. , 1999. **111**(15): p. 6955-6964.

21. Li, L.-s. and A.P. Alivisatos, *Origin and Scaling of the Permanent Dipole Moment in CdSe Nanorods.* Phys. Rev. Lett. , 2003. **90**(9): p. 097402/1-097402/4.

8. Polymer Nanocomposites

8.1. History

The origin of today's polymers can be traced to the work of Wallace Carothers at Du Pont, where his greatest achievement was the synthesis of nylon as a superior replacement for silk. Over the next two decades new polymers were rapidly introduced and began to become a common substitute for wood and metal. Today the trend perpetuates as plastics overtake the food packaging industry where traditional glass, metal and paper packaging continue to be displaced. The automotive industry has also begun using plastics to lower the weight of cars and improve methods of manufacturing. Despite the vast improvements plastics have been able to make, however, they are not free from limitations. For instance, in the packaging industry certain foods are sensitive to oxygen and cannot be stored in plastic containers due to their oxygen permeability. In the auto industry, low tensile strength and the tendency to warp under heat have limited the use of plastics in certain applications.

The first successful attempt at pushing polymers to a new level of performance was accomplished by Toyota Central Research Laboratories where two divergent organic and mineral materials were successfully integrated. This first practical application of a "nanocomposite" of nylon-montmorillonite is a timing belt cover on a Toyota Camry. The new material exhibited increased tensile strength, modulus and heat distortion temperature without a loss in impact resistance. It was also less sensitive to water and had a low gas permeability. This initial success has spurred a

large amount of research in industrial and university settings which continues in full force today.

8.2. Promise and Challenges

The term "polymer nanocomposite" has now come to refer to a multi-component system where the primary constituent is a polymer or blend of polymers and the minor constituent is a material exhibiting at least one dimension below 1 μm on one single particle scale. Over the past two decades the benefits of using nanoparticles as additives to enhance polymer performance have been well established and now many nanocomposites are finding their way into a diverse number of applications.[1-6] Properties which have been shown to undergo significant improvements include:

1. Mechanical properties such as strength, modulus and dimensional stability[7-9]
2. Decreased permeability to water, gases, and hydrocarbons[10, 11]
3. Thermal stability and distortion temperature[12-14]
4. Flame resistance and reduced smoke emissions[2]
5. Chemical resistance[15-17]
6. Electrical conductivity[18, 19]
7. Optical clarity[20]

It is also important to recognize that many of these improved physical properties were accomplished with very low loading levels. Low-volume additions (1-10%) of isotropic nanoparticles such as titania, silver, or alumina, and anisotropic particles

such as layered silicates (clays) or carbon nanotubes provide property enhancements that are comparable to that achieved by conventional loadings (15-40%) of traditional micrometer-scale fillers.[21] The lower loading levels reduce component weight and thereby facilitating the processing method.

The objective for a vast majority of today's nanocomposite research is to achieve increased performance through dispersion at the single-particle level. The resulting composites are treated as isotropic, filled polymers. Thus, nanocomposites today are really just nanoparticle-filled plastics (**Figure 8.1**).[22] This should be considered a significant problem if polymer nanocomposites are to move beyond commodity plastics and provide optimal performance for high-technology applications such as electronic packaging, engineered aerospace structural components, and optical gratings to name a few.

There are many discussions which consider the implications of controlling the particle orientation.[23-26] Some reports predict huge improvements in mechanical, barrier, and electrical performance in morphology controlled nanoparticles. As an example, Gusev and Rozman showed that comparable shear could be obtained at half the volume fraction of particles if a web-like morphology could be generated versus a random or hexagonal arrangement.[27]

An extensive number of review papers are available that summarize the status of various particle-polymer combinations, the proposed advantages of invoking spatial order in a matrix, and the challenges that still need to be overcome.[28-34] Reports over the last few years on morphology control of composites have shown the ability to

create uniaxial alignment of nanoparticles (both plates and rods) using external forces. Common approaches include sedimentation,[35] spin coating,[36] mechanical deformation,[37-41] magnetic fields,[42, 43] and electric gradients.[44] However, more detailed studies are needed, and a robust process is still yet to be found.

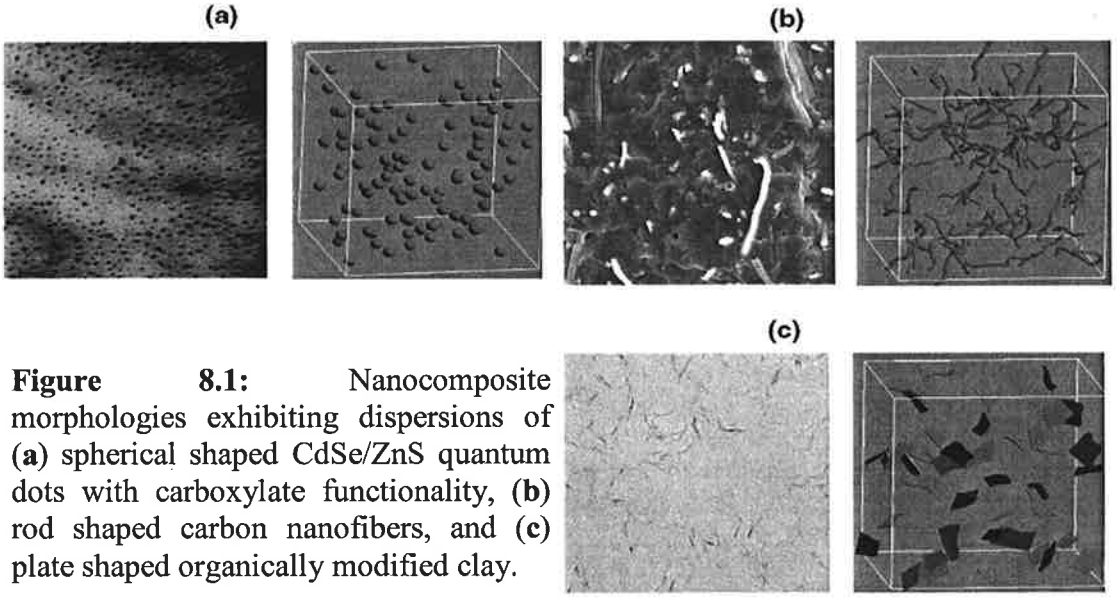

Figure 8.1: Nanocomposite morphologies exhibiting dispersions of (**a**) spherical shaped CdSe/ZnS quantum dots with carboxylate functionality, (**b**) rod shaped carbon nanofibers, and (**c**) plate shaped organically modified clay.

8.3. Field Induced Alignment

The following sections highlight the use of electric fields as a patterning tool in detail. It has already been in the current work that electric fields induce alignment and thus "order" within a system of aqueous nanoparticles. However, because permanent and induced-dipoles generally scale with particle size, as particle volumes decrease, the field strengths needed to overcome the thermal motion increase considerably. The result is an imposition on filler dimensions. Additionally, the time necessary to

achieve appreciable alignment increases considerably with viscosity. An example of this is shown in **Figure 8.2** where the log of the rise time of a clay sample is plotted as a function of solvent viscosity. Through varying combinations of water and PEG the solvent viscosity was increased by a factor of three and resulted in a subsequent increase in rise time by 47 fold.

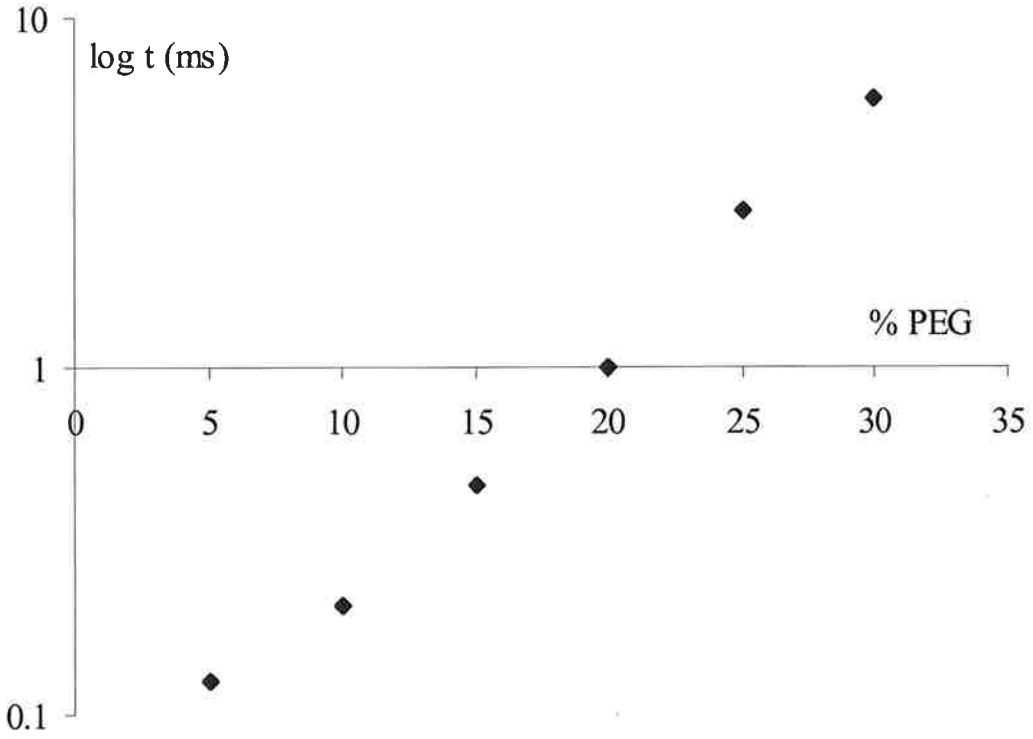

Figure 8.2: Rise times of a 20 ug/ml clay sample subject to a 5.0 kV/cm field as a function of solvent flow rate. Composition of the solvent ranged from 5 – 30% PEG.

One of the goals of this research is to show that application of a pulsed DC field will produce appreciable alignment of a composite during the curing process while, at the same time, avoiding polymer breakdown. The ability to align the nanofiller in this

manner rests on the fact that the relaxation process is orders of magnitude slower than that of the alignment. In addition, polymer breakdown can be avoided because, although the field strength may be large, it is applied for a relatively short period of time. This could offer a pathway to a viable manufacturing method.

The buildup of alignment in a water/PEG/clay sample is shown in **Figure 8.3**. DC coupled TEB signals were captured on an oscilloscope every 30 seconds for ten minutes. What is observed is a steady buildup in the DC signal until a saturation level is achieved. Such a result suggests that if the viscosity of the solution is low enough prior to curing, residual alignment can be captured in the final product.

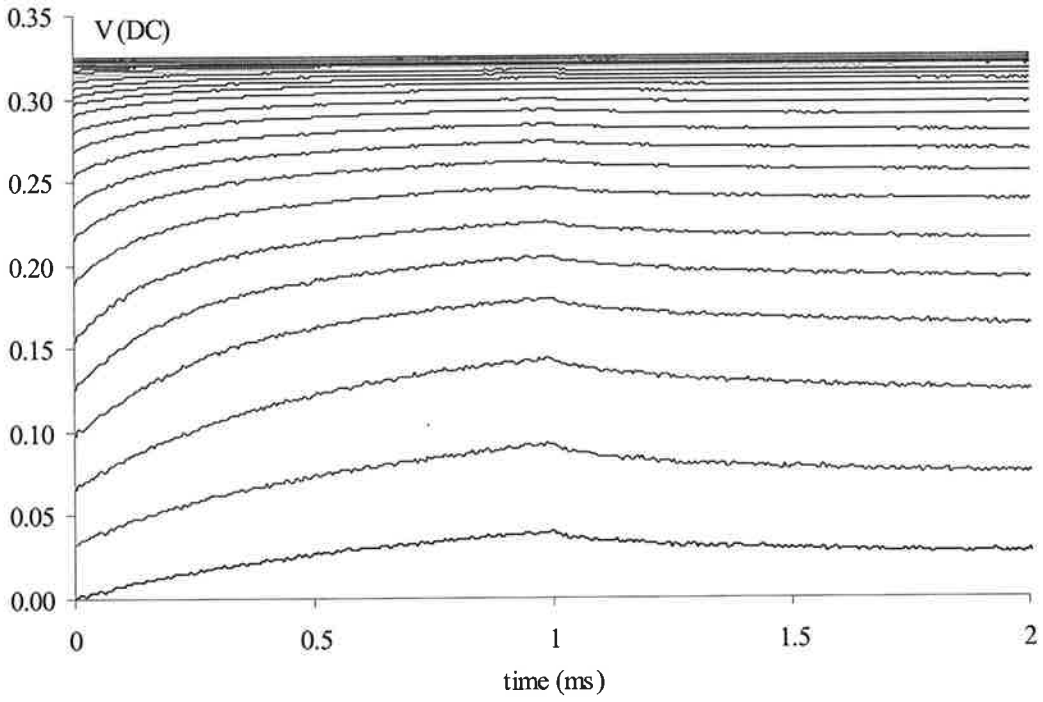

Figure 8.3: Birefringent response of a 20 ug/ml clay sample subject to a 5.0 kV/cm field as a function of solvent flow rate. Composition of the solvent ranged from 5 – 30% PEG.

8.4. Experimental Setup

The objective of this study was to produce a nanocomposite containing a spatially ordered filler. Two methods for making the nanocomposites were explored. The first was an evaporation technique which was chosen initially for its simplicity and the ability to control the size and shape of the polymer units. The process required slow addition and stirring of a polymer to a solvent until a reasonably viscous, but workable solution is obtained. The nanofiller could then be added to the solution and sonicated so it is adequately dispersed. A Teflon mold containing two stainless steel electrodes was constructed (**Figure 8.4**) so that a field could be applied to a small aliquot of the final solution, as the solvent was allowed to evaporate.

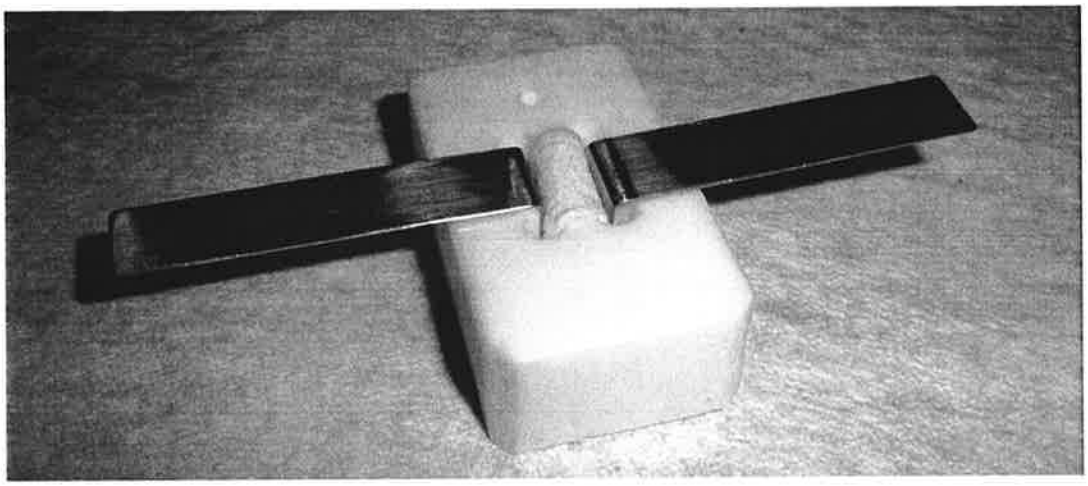

Figure 8.4: Sample holder constructed for the creation of nanocomposites through solvent evaporation.

After trying various combinations of polymer and solvent, we came to the conclusion that polystyrene dissolved in tetrahyrofuran (THF) was the most promising. The

structure of polystyrene is simple and the polymer can be purchased in predetermined molecular weights. Thus, interference of the alignment by a "bulky" polymer could be minimized by keeping the molecular weight low. THF is also very volatile and quick evaporation of the solvent is ideal in order to minimize the curing time. In an effort to make a set of control samples, initial trials were attempted on polymer solutions absent of any filler. Unfortunately, we soon discovered that total evaporation of the solvent was very hard to achieve. In most cases, only the top layer of the solution would harden. We also found that removal of the composite was difficult, often resulting in the polymer being stretched apart. This method of composite synthesis was therefore abandoned.

The second method was radical initiated polymerization. The technique involves using molecules with an O-O single bond that is unstable and breaks apart upon application of heat. The resulting products contain a lone electron and are termed radical initiators. **Figure 8.5** shows an example of a radical initiated polymerization on an ethene monomer. One electron pair is held securely between the two carbons in a sigma bond, while the other is more loosely held in a pi bond. The free radical uses one electron from the pi bond to form a new bond, while the second electron remains unpaired, turning the whole molecule into another radical. Termination occurs when a radical reacts in a way that prevents further propagation. The most common method of termination is by coupling two radicals to form a single molecule.

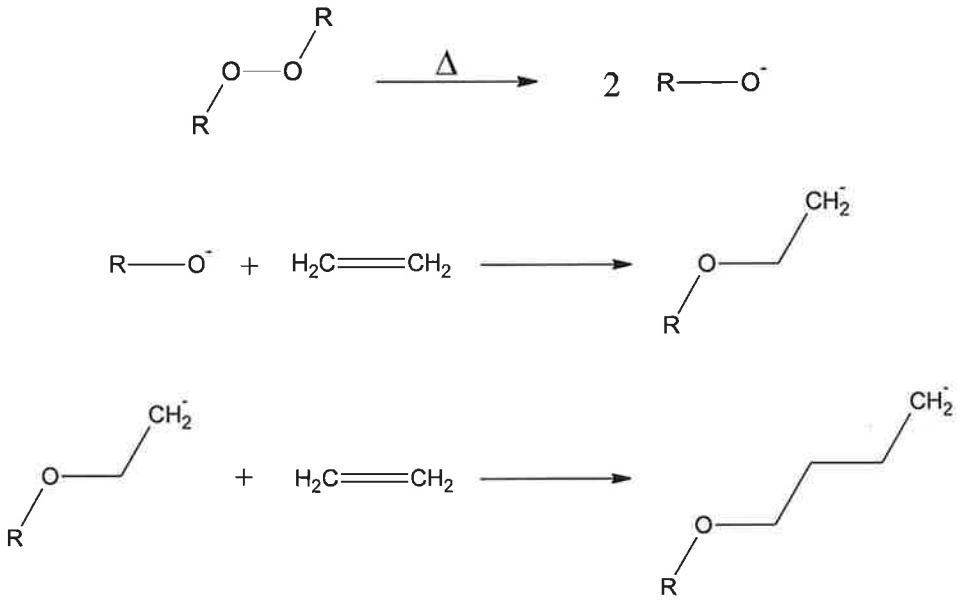

Figure 8.5: Steps involved in the radical initiated polymerization of ethene.

The main drawback to radical polymerization is the termination process which occurs randomly when two chains collide, leaving no ability to control the lengths of individual chains. However, the curing process is fast, requiring only a couple of hours. Once complete, the reaction should result in a hardened polymer that is solid throughout.

A method for addition of CdSe quantum dots to a polymer using a radical initiator was found in the literature.[45] The process involves the use of laurylmethacrylate monomer to produce polylaurylmethacrylate (PLMA) with ethyleneglycol dimethacrylate as a cross-linker. The monomer solution was placed in a glass beaker containing a Teflon insert with two small grooves for the electrodes (**Figure 8.6**). The benefit of this setup was that everything could be removed as one

piece, at which time the electrodes could be pulled apart without disturbing the composite material between them.

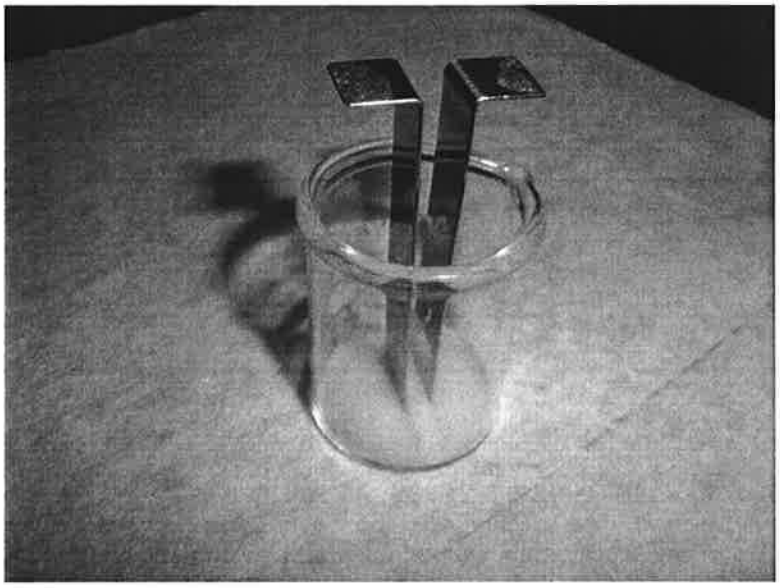

Figure 8.6: Sample holder constructed for the creation of polymer nanocomposites through radial initiation.

Initial trials of pure polymer samples were successful. The sample holder was easy to work with, primarily due to the ease at which the samples could be removed. Subsequent experiments were performed with composite materials containing either carbon nanotubes or CdSe quantum dots as fillers. The resulting nanocomposites can be seen in **Figure 8.7**. The black cube on the left of the figure contains the carbon nanotubes at a concentration of ~ 7.5 x 10^5 g/ml. The cube on the right contains the CdSe quantum dots at a concentration of ~ .8 μM and appears bright because the photo was taken while irradiating the polymer with UV light.

8.4.1. Experimental

Organic quantum dots or multi-walled carbon nanotubes were dispersed into laurylmethacrylate monomer with trioctylphosphine (TOP) (5% v/v) and ultrasonicated for ten minutes. Then, the cross-linker ethyleneglycol dimethacrylate was added to the monomer solution with a 1:4 volume ratio of cross-linker to monomer. After azobisisobutyronitrile (AIBN) radical initiator (<1 % w/w) was added, the final solution was polymerized in an oven at 70 ~ 75 °C for 2 h. Samples cured under an external field were subjected to a 1 ms, pulsed 5.0 kV/cm DC field, which was applied at a frequency of 10 Hz for the duration of the curing process.

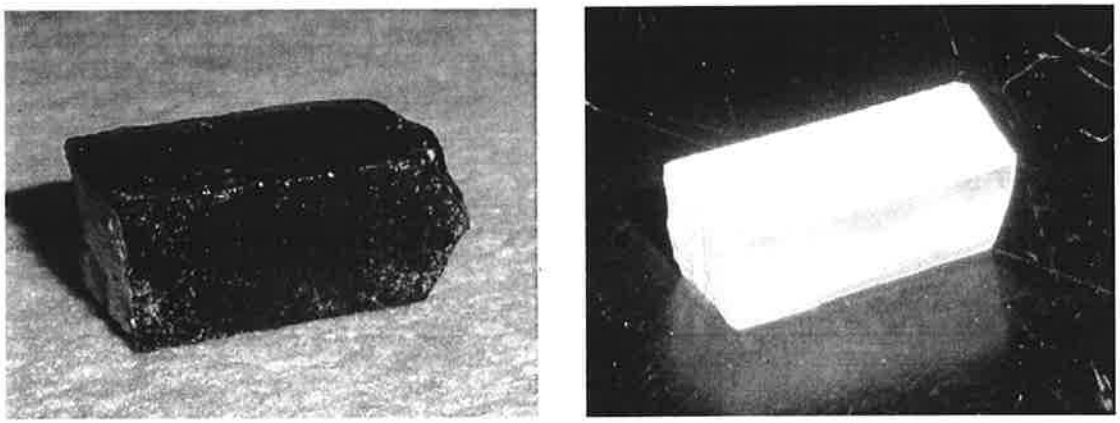

Figure 8.7: Polymer nanocomposites containing carbon nanotubes (left) and CdSe quantum dots (right).

8.5. Carbon Nanotube Composite

8.5.1. Introduction

The outstanding chemical and physical properties of nanotubes have been well documented for over a decade.[46, 47] There are speculations that many of these properties can be best exploited by incorporating the nanotubes into some form of matrix, and the preparation of nanotube containing composite materials is now a rapidly growing field.[48]

A commonly used method for preparing nanotube polymer composites involves solvent evaporation. As was previously mentioned, this process was attempted in the current study but with little success. An alternative method is to use the corresponding monomers and initiate polymerization in situ. Cochet et al. were among the first to use this latter method and prepared a nanotube/polyaniline composite.[49] A number of other nanotube/polymer composites have also been prepared using the same method, including MWNT/polystyrene[50] and SWNT/polyimide.[51] Several groups have also used electrochemical polymerization to grow porous composite films of nanotubes for use as supercapacitors.[52, 53] In the techniques described so far, the aim has been to produce uniformly distributed nanotubes in the composites, with no attention to the alignment of the nanotubes

The goal of the present work was to observe the influence of electric fields on alignment of carbon nanotubes in a polymer matrix. The expectation was that a clearly visible alignment of the particles would be present if the curing process of the polymer did not disrupt the effect of an external field. In **Appendix C**, the response of CNT to

a pulsed DC electric field is discussed. Although the alignment mechanism is dominated by the induced dipole, the contribution of a permanent dipole is not negligible.

8.5.2. Results

Dispersions of carbon nanotubes have been achieved in a wide range of materials by either shear mixing or by the use of a high-energy ultrasonic probe. The aqueous and polymer dispersions created in this study were made using a GE600 Ultrasonic Processor, with a 13 mm diameter Ti alloy probe. However, even though the nanotubes were sonicated and dispersed well in the monomer solution, they aggregated considerably during the curing process. **Figure 8.8** shows images of the composite under varying magnifications through a light microscope. The top two images are of a section cut from a composite that was cured in the absence of an external field. The random nature of the composite is evident, as well as a considerable amount of aggregation in the nanotube filler. The bottom images show a section cut parallel to the alignment direction but for a sample which was subjected to a pulsed DC field. Aggregation is observed again, but there is a clear orientation to the aggregated particles, directed along the field (white arrows). The results show that the morphology of the composite can be directed using a pulsed DC field. However, aggregation of the nanotubes during the polymer cure is a major problem.

Although it is desirable to have an evenly dispersed solution, the dispersive step in creating the nanocomposites is of little help in minimizing the aggregation of

particles during the curing process. Overcoming this crucial step is important if improved physical properties of the composite materials are to be realized. In a 2004 interview, Satish Kumar, a professor in Georgia Tech's School of Polymer, Textile and Fiber Engineering, was paraphrased as saying: The greatest impact of carbon nanotubes will be realized only if researchers can learn how to break up the bundles to produce individual nanotubes, a process called exfoliation. If that can be done, the quantity of tubes required to improve the properties of fibers could be reduced from 10 percent to as little as 0.1 percent by weight. That could help make use of the nanotubes – which now cost hundreds of dollars per gram –feasible for commercial products. [54]

A few methods have been established for the exfoliation of carbon nanotubes to produce stable aqueous and polymer solutions. However, in some cases they are very specific to the polymer and are limited to the dispersion of CNTs into polymers created through the evaporation method;[55-57] thus, not allowing for their direct application to PLMA. In other cases, the dispersion is achieved by processing techniques which are carried out on the tubes themselves and were not achievable in our lab.[58-60] Thus, future work should focus first on maintaining the exfoliated nature of the nanotubes through the curing process of a radical initiated polymerization, followed by the field induced alignment of the nanocomposite.

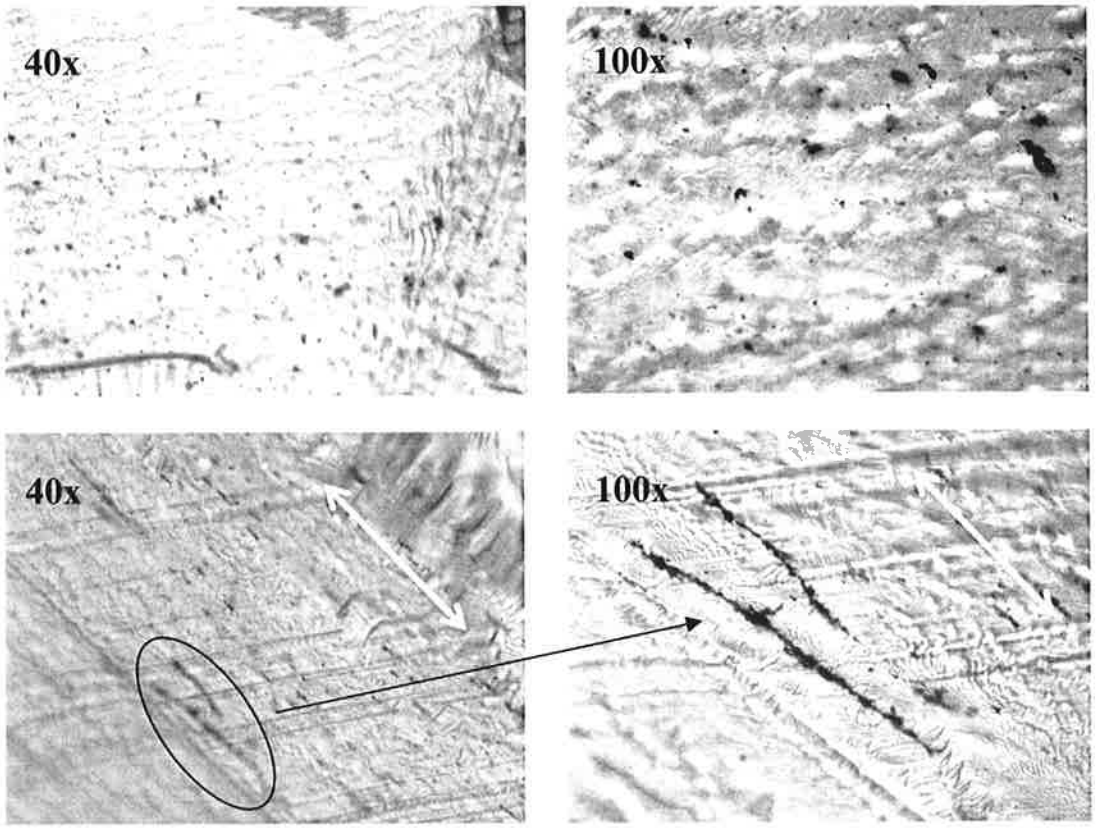

Figure 8.8: Light microscope images of the CNT nanocomposite. The top images show the random nature of a polymer composite containing carbon nanotubes that was cured with no alignment field present. The bottom images show the net orientation induced in aggregates of nanotubes contained in the nanocomposite that was cured in the presence of a pulsed DC alignment field that was applied in the direction of the white arrows.

8.6. CdSe Quantum Dot Composites

8.6.1. Introduction

Unlike the majority of nanocomposites, which are being studied because of their improved mechanical properties, quantum dot nanocomposites are of interest primarily because of their possible improvement in optical properties. The optical enhancements that quantum dots add to their host material are due to their unique properties as quantum confined semiconductors. This imparts them with the ability to emit very narrow bands of light when they fluoresce. Thus, it is no surprise that, in recent years, the focus has been on the addition of quantum dots to polymers as a first step toward an efficient, organic light emitting diode (OLED). This is evidenced by the peaked interest in OLEDs as a possible replacement for the current LED. For certain device applications, semiconducting polymers can replace inorganic semiconductors at lower costs because they are more easily processed. One example is the development of OLEDs for full-color screen applications.[61]

Another recently discovered and highly significant property of rod shaped quantum dots is their emission of polarized light. The significance of a polarized LED lies in the potential improvement in the energy efficiency of liquid crystal displays (LCDs). LCDs use polarized light, hence a polarizer is typically used with a unpolarized light source, resulting in an energy efficiency less than 50%. The importance of polarized backlight in LCD technology was recognized in 2008 by the Massachusetts Institute of Technology, when they awarded the $30,000 Lemelson-Rensselaer Prize to Martin Schubert for his development of a new LED with a

polarization ratio of ~2:1. Schubert's innovation uses a carefully constructed back reflector to redirect the more polarized light from the edges of current LEDs so that it projects forward.[62]

On the other hand, Hu et al discovered that the emission from CdSe quantum dots with an aspect ratio of 2:1 or greater is ~ 70% polarized.[63] It is conceivable then that the polarized emission from these rod shaped nanoparticles could be used to produce the first polarized OLED. Thin films of quantum dots have already been shown to electroluminescence at relatively low voltages (~10 – 17V),[64] so application of a voltage across the back panel of the display could result in a polarized light source. **Figure 8.9** shows the layers of a liquid crystal display and where the quantum dot thin film would be incorporated.

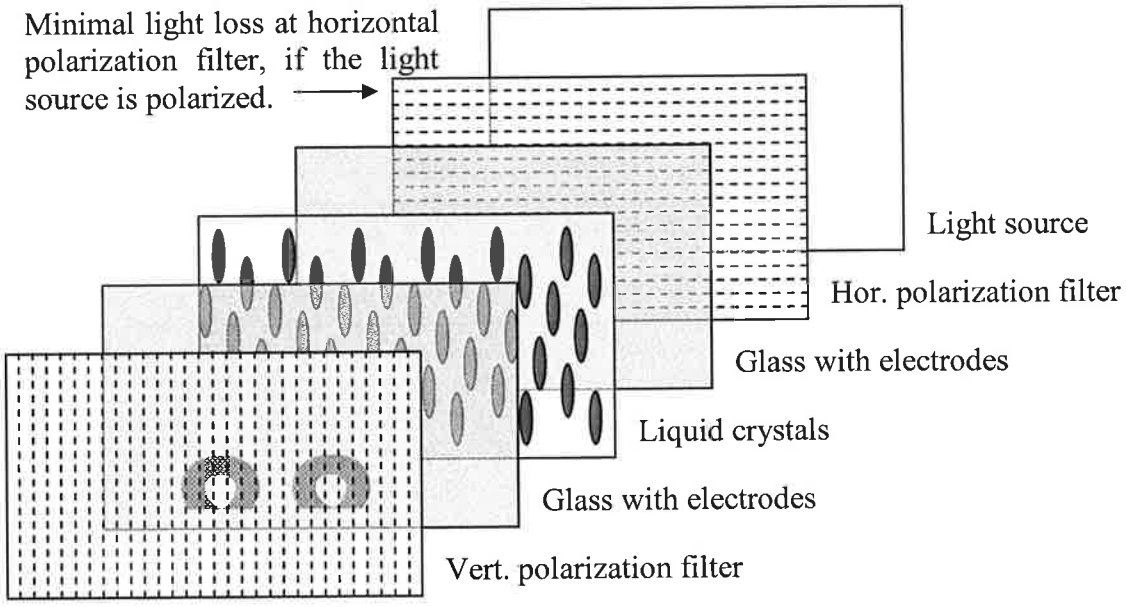

Figure 8.9: The various layers of a liquid crystal display. The light source, which rests at the back of the display, could be a QD nanocomposite that emits polarized light when a voltage is applied to it.

8.6.2. Results

CdSe quantum dots were added to PLMA to see if alignment could be induced and retained in the particles during the curing process. **Figure 8.10** shows TEM images of polymer samples containing the quantum dots, which were cured both in the presence and absence of an external field. It can be seen in the first two images (a and b) that a small preferred orientation is visible in the samples that were cured in a field directed from the top left to the bottom right (white arrow). In contrast, image *c* shows the random nature of the quantum dots in the nanocomposite that was cured in the absence of a field.

There appeared to be a small electrophoretic effect, which was visible in the bulk samples. This was evidenced when the nanocomposite was irradiated with UV light and fluorescence was not observed from approximately the first half millimeter of composite, closes to the negative electrode. This is most likely due to the small size of the quantum dots, which made it easier for them to be pulled through the polymer solution before it was completely cured. Unfortunately, the power supply is unipolar, which means that the direction of the alignment field cannot be varied. An improvement to the system would be the ability to alter the direction of the applied wave from one pulse to the next.

With alignment of the QDs possible, the next step should be directing the process toward the creation of a thin polymer film composite. This could be accomplished by spray coating a polymer solution onto a glass slide which has been treated on its edges with TiO_2, to act as electrodes. If the film is thin enough, an

evaporation method, like the one described earlier, may be effective. We suspect that the radical initiated polymerization process may be an inhibiting factor in achieving maximum alignment of the filler, due to the uncontrolled nature in which the polymerization proceeds. Thus, returning to evaporation may also result in better alignment. If the polymer is slightly conducting, application of a voltage across the TiO2 electrodes may induce electroluminescence in the composite. The electroluminescent thin film could be the first step toward a polarized light source for use in thin panel displays.

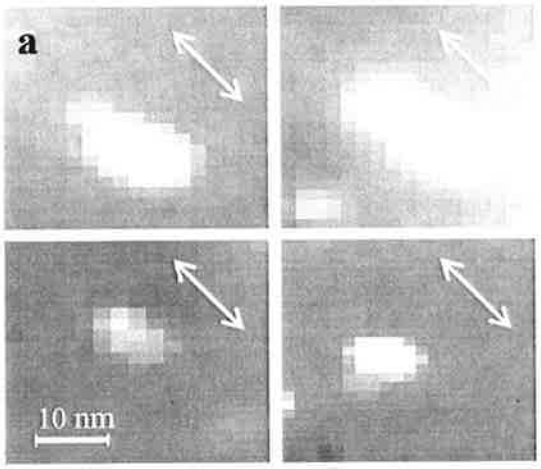

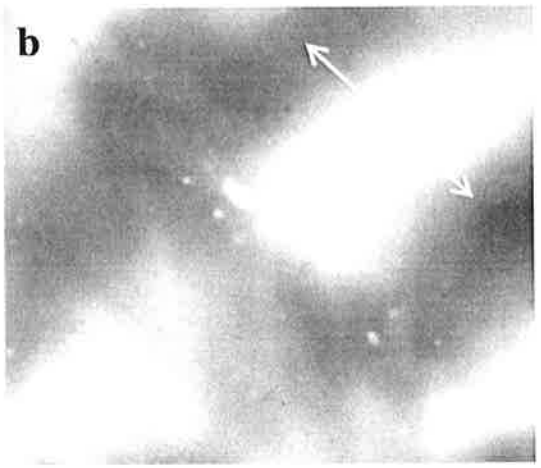

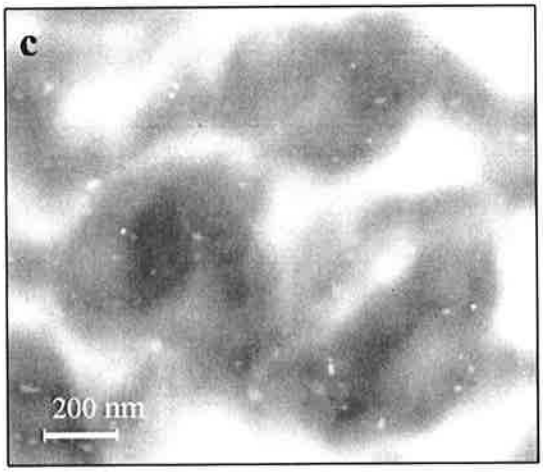

Figure 8.10: a,b) polymer composite containing CdSe quantum dots which exhibit a small preferred alignment, due to the application of a pulsed DC field during the curing process. **c)** polymer composite containing CdSe quantum dots which show a random orientation.

8.7. References

1. Camargo, P.H.C., K.G. Satyanarayana, and F. Wypych, *Nanocomposites: synthesis, structure, properties and new application opportunities.* Mater. Res. (Sao Carlos, Braz.) , 2009. **12**(1): p. 1-39.

2. Horrocks, A.R. and B.K. Kandola, *Potential applications of nanocomposites for flame retardancy.* Flame Retard. Polym. Nanocompos. , 2007: p. 325-353.

3. Althues, H., J. Henle, and S. Kaskel, *Functional inorganic nanofillers for transparent polymers.* Chem. Soc. Rev. , 2007. **36**(9): p. 1454-1465.

4. Sanders, T., T. Liu, and G. Veser, *Nanocomposite materials for clean energy applications.* Abstracts of Papers, 233rd ACS National Meeting, Chicago, IL, United States, March 25-29, 2007

5. Thomas, P.S., et al., *Polymer nanocomposites: preparation, properties and applications.* Gummi, Fasern, Kunstst. , 2006. **59**(9): p. 544-552.

6. Maiti, A., J. Wescott, and G. Goldbeck-Wood, *Mesoscale modeling: recent developments and applications to nanocomposites, drug delivery and precipitation membranes.* Int. J. Nanotechnol. , 2005. **2**(3): p. 198-214.

7. Okhlopkova, A.A., et al., *Tribological and physical-mechanical properties of nanocomposites based on PTFE and aluminum oxide.* Trenie Iznos , 2008. **29**(6): p. 635-639.

8. Siqueira, G., J. Bras, and A. Dufresne, *Cellulose Whiskers versus Microfibrils: Influence of the Nature of the Nanoparticle and its Surface Functionalization on the Thermal and Mechanical Properties of Nanocomposites.* Biomacromolecules , 2009. **10**(2): p. 425-432.

9. Gonzalez, I., J.I. Eguiazabal, and J. Nazabal, *Structure and mechanical properties of nanocomposites based on an amorphous copolyester.* Macromol. Mater. Eng. , 2008. **293**(9): p. 781-788.

10. Ashurov, N.R., et al., *Permeability of nanocomposites based on polyamide-6 and montmorillonite.* O'zb. Fiz. J. , 2006. **8**(3): p. 100-104.

11. Tsou, A.H. and A.J. Dias, *Low permeability nanocomposites*. 2002, (Exxonmobil Chemical Patents Inc., USA). Application: WO WO. p. 29 pp.

12. Kuan, H.-C., et al., *Synthesis, characterization, and thermal stability of PMMA/SiO2/TiO2 tertiary nanocomposites via non-hydrolytic sol-gel method.* J. Appl. Polym. Sci. , 2009. **113**(3): p. 1959-1965.

13. An, L., et al., *Rod-like attapulgite/polyimide nanocomposites with simultaneously improved strength, toughness, thermal stability and related mechanisms.* J. Mater. Chem. , 2008. **18**(41): p. 4928-4941.

14. Park, S.-J., D.-I. Seo, and J.-R. Lee, *Surface Modification of Montmorillonite on Surface Acid-Base Characteristics of Clay and Thermal Stability of Epoxy/Clay Nanocomposites.* J. Colloid Interface Sci. , 2002. **251**(1): p. 160-165.

15. Huang, B. and N. Li, *Corrosion resistance of electrodeposited Ni-ZrO2 composite coating.* Kuangye Gongcheng (Changsha, China) , 2009. **29**(1): p. 97-100.

16. Sun, W.-m., Z. Zheng, and Z. Liu, *Preparation and oxidation resistance of Fe-TiC composite nanopowders.* Gongneng Cailiao , 2007. **38**(8): p. 1373-1376.

17. Giaya, A., et al., *Nanocomposite barrier fabric for chemical and biological agent resistant tent.* Sel. Top. Electron. Syst. , 2006. **42**(Transformational Science and Technology for the Current and Future Force): p. 485-490.

18. Ma, P.-C., et al., *Enhanced Electrical Conductivity of Nanocomposites Containing Hybrid Fillers of Carbon Nanotubes and Carbon Black.* ACS Appl. Mater. Interfaces , 2009. **1**(5): p. 1090-1096.

19. Jana, S., et al., *Electrical conductivity of nanocomposites with lithium compound and gold nanoparticles.* SAMPE Conf. Proc. , 2007. **52**: p. 106/1-106/9.

20. Thompson, C.M., et al., *Preparation and characterization of metal oxide/polyimide nanocomposites.* Compos. Sci. Technol. , 2003. **63**(11): p. 1591-1598.

21. Vaia, R.A. and J.F. Maguire, *Polymer Nanocomposites with Prescribed Morphology - Going Beyond Nanoparticle-Filled Polymers.* Chem. Mater., 2007. **19**: p. 2736-2751.

22. Koerner, H., et al., Polymer, 2005. **47**: p. 3426.

23. Jurenkova, M. and A. Marcincin, *Fiber-forming polymeric nanocomposites. II. Rheology of polymeric nanocomposites.* Vlakna Text. , 2005. **12**(1): p. 29-32.

24. Famulari, A., et al., *Clay-induced preferred orientation in polyethylene/compatibilized clay nanocomposites.* J. Macromol. Sci., Part B: Phys. , 2007. **46**(2): p. 355-371.

25. Zhao, W., et al., *Facile preparation of epoxy-based composite with oriented graphite nanosheets.* Polymer , 2006. **47**(26): p. 8401-8405.

26. Wang, X., et al., *Unusual Rheological Behavior of Liquid Polybutadiene Rubber/Clay Nanocomposite Gels: The Role of Polymer-Clay Interaction, Clay Exfoliation, and Clay Orientation and Disorientation.* Macromolecules , 2006. **39**(19): p. 6653-6660.

27. Gusev, A.A. and M. Rozman, Comput. Theor. Polym. Sci., 1999. **9**: p. 335.

28. Pinnavaia, T.J. and G.W. Beall, *Polymer-Clay Nanocomposites.* 2001, New York: Wiley & Sons.

29. Giannelis, E.P., *Polymer layered silicate nanocomposites.* Advanced Materials (Weinheim, Germany), 1996. **8**(1): p. 29-35.

30. Alexandre, M. and P. Dubois, *Polymer-layered silicate nanocomposites: preparation, properties and uses of a new class of materials.* Materials Science & Engineering, R: Reports, 2000. **R28**(1-2): p. 1-63.

31. Ray, S.S. and M. Okamoto, Prog. Polym. Sci., 2003. **2**: p. 1539.

32. Thostenson, E.T. and C.-m. Li, Compos. Sci. Technol., 2005. **65**: p. 491-516.

33. Tjong, S., Mater. Sci. Eng. R, 2006. **53**: p. 73.

34. Hussain, F., et al., *Polymer-matrix nanocomposites, processing, manufacturing, and application: an overview.* Journal of Composite Materials, 2006. **40**(17): p. 1511-1575.

35. Grillet, A.-C., et al., *Control of the morphology of waterborne nanocomposite films.* Polymer International, 2004. **53**(5): p. 569-575.

36. Fong, H., et al., *Self-Passivation of Polymer-Layered Silicate Nanocomposites.* Chemistry of Materials, 2001. **13**(11): p. 4123-4129.

37. Fong, H., et al., *Generation of electrospun fibers of nylon 6 and nylon 6-montmorillonite nanocomposite.* Polymer, 2001. **43**(3): p. 775-780.

38. Pavlikova, S., et al., *Fiber spinning from poly(propylene)-organoclay nanocomposite.* Journal of Applied Polymer Science, 2003. **89**(3): p. 604-611.

39. Vigloo, B., et al., Science, 2003. **290**: p. 1331.

40. Kumar, S., et al., *Synthesis, Structure, and Properties of PBO/SWNT Composites.* Macromolecules, 2002. **35**(24): p. 9039-9043.

41. Dirama, T. and L. Goettler, *Film Blowing of Layered Silicate Nanocomposites.* Materials and Manufacturing Processes, 2006. **21**(2): p. 199-210.

42. Koerner, H., et al., *Deformation-morphology correlations in electrically conductive carbon nanotube-thermoplastic polyurethane nanocomposites.* Polymer, 2005. **46**(12): p. 4405-4420.

43. Casavant, M.J., et al., *Neat macroscopic membranes of aligned carbon nanotubes.* Journal of Applied Physics, 2003. **93**(4): p. 2153-2156.

44. Koerner, H., et al., *Tuning polymer nanocomposite morphology: AC electric field manipulation of epoxy-montmorillonite (clay) suspensions.* Advanced Materials (Weinheim, Germany), 2004. **16**(4): p. 297-302.

45. Lee, J., et al., *Full Color Emission from II±VI Semiconductor Quantum Dot±Polymer Composites.* Advanced Materials, 200. **12**(15): p. 1102-1105.

46. Ajayan, P.M. and T.W. Ebbesen, *Nanometer-size tubes of carbon.* Rep. Prog. Phys. , 1997. **60**(10): p. 1025-1062.

47. Forro, L. and C. Schonenberger, *Physical properties of multi-wall nanotubes.* Top. Appl. Phys. , 2001. **80**(Carbon Nanotubes): p. 329-390.

48. Thostenson, E.T., et al., *Carbon nanotube/carbon fiber hybrid multiscale composites.* J. Appl. Phys. , 2002. **91**(9): p. 6034-6037.

49. Cochet, M., et al., *Synthesis of a new polyaniline/nanotube composite: "in-situ" polymerisation and charge transfer through site-selective interaction.* Chem. Commun. (Cambridge, U. K.) , 2001(16): p. 1450-1451.

50. Shaffer, M.S.P. and K. Koziol, *Polystyrene grafted multi-walled carbon nanotubes.* Chem. Commun. (Cambridge, U. K.) , 2002(18): p. 2074-2075.

51. Park, C., et al., *Dispersion of single wall carbon nanotubes by in-situ polymerization under sonication.* Chem. Phys. Lett. , 2002. **364**(3,4): p. 303-308.

52. Jurewicz, K., et al., *Supercapacitors from nanotubes/polypyrrole composites.* Chem. Phys. Lett. , 2001. **347**(1,2,3): p. 36-40.

53. Hughes, M., et al., *Electrochemical Capacitance of a Nanoporous Composite of Carbon Nanotubes and Polypyrrole.* Chem. Mater. , 2002. **14**(4): p. 1610-1613.

54. Toon, J., *New Class of Fibers: Composites Made with Carbon Nanotubes Offer Improved Mechanical & Electrical Properties*. 2004: Atlanta, Ga.

55. Lee, G.-W., et al., *Carbon nanotube dispersion and exfoliation in polypropylene and structure and properties of the resulting composites.* Polymer , 2008. **49**(7): p. 1831-1840.

56. Chae, H.G., M.L. Minus, and S. Kumar, *Oriented and exfoliated single wall carbon nanotubes in polyacrylonitrile.* Polymer , 2006. **47**(10): p. 3494-3504.

57. Uchida, T. and S. Kumar, *Single wall carbon nanotube dispersion and exfoliation in polymers.* J. Appl. Polym. Sci. , 2005. **98**(3): p. 985-989.

58. Chen, L., L.S. Schadler, and R. Ozisik, *Improving dispersion of SWNT in polymers by supercritical carbon dioxide assisted processing.* Abstracts of Papers, 236th ACS National Meeting, Philadelphia, PA, United States, August 17-21, 2008 59.

59. Chen, L., R. Ozisik, and L.S. Schadler, *Improvement of the dispersion of single-walled carbon nanotubes in polymer matrices by supercritical carbon dioxide foaming process.* Abstracts of Papers, 234th ACS National Meeting, Boston, MA, United States, August 19-23, 2007 60.

60. Kasimatis, K.G., et al., *Polymer nanocomposites by pulverization: enhanced properties and dispersion.* Annu. Tech. Conf. - Soc. Plast. Eng. , 2005. **63rd**: p. 1965-1969.

61. Dodabalapur, A., et al., *Resonators and materials for organic lasers based on energy transfer.* IEEE J. Sel. Top. Quantum Electron. , 1998. **4**(1): p. 67-74.

62. Cho, J.-H., et al., *Light emitting diodes and liquid crystal display apparatuses using the same as edge type backlight units to improve optical efficiency*. 2008, (Samsung Electro-Mechanics Co., Ltd., S. Korea; Rensselaer Polytechnic Institute). Application: US
US. p. 12 pp.

63. Hu, J., et al., *Linearly Polarized Emission from Colloidal Semiconductor Quantum Rods.* Science, 2001. **292**(5524): p. 2060-2063.

64. Dabbousi, B.O., et al., *Electroluminescence from CdSe quantum-dot/polymer composites.* Appl. Phys. Lett. , 1995. **66**(11): p. 1316-18.

9. Summary Remarks

9.1. General Conclusions

The experimental results described in **Chapters 5 – 7** and **Appendix C** illustrate the physical and chemical parameters which can be studied by means of electro-optical measurements. The principal ones are:

i. The rotational diffusion coefficient D_R (determined through the relaxation time), which allows for the calculation of particle dimensions and percolation thresholds (when plotted against field strength E).

ii. The optical anisotropy Δg and specific Kerr constant *Ksp*, which are directly related to the permanent and/or induced-dipole moment through the alignment parameter $\langle P_2(\beta^2, 2\gamma) \rangle$.

iii. The field dependence of the rise time, which can be used to determine the sum of the permanent dipole and polarizability anisotropy when the thermal energy kT is taken into account and the rotational diffusion coefficient D_R is known.

Several deductions can be made from these findings. Electronic polarizabilities furnish information about the existence of an ionic atmosphere and its behavior under different conditions. Permanent dipole moments are related to distributions of charged groups on particles. In addition, relaxation times offer information on the polydispersity, state of aggregation, and interparticle interactions.

On the other hand, interpretations of the intrinsic anisotropy and polarizability in terms of precise structural features have proved difficult; a fact that was exemplified in the behavior of Na-montmorillonite. It should be pointed out that one has to exert extreme caution and be aware of the drawbacks of the electro-optical method when attempting an interpretation of an experimental result. For example, it was shown that much of the anomalous, field dependent data of Na-montmorillonite could be artificially reproduced through misalignment of optical components. Thus, conclusions about intrinsic anisotropy made from single measurements over limited field strengths are of limited value, and a number of experimental tests under different conditions and using different methods are essential.

Nevertheless, TEB is a powerful method for the determination of the physical parameters identified above, owing to its simplicity and its applicability to virtually any non-conducting solutions. This point is evidenced in the current work by the wide range of particle types, ranging from a polydispersed system of relatively large sheets and rods (Na-montmorillonite) to a virtually monodispersed system of small sized rod shaped semiconductive QDs. In all cases, particle dimensions were accurately calculated and confirmed by comparisons with reports from other groups and/or TEM images, as well as permanent dipole moments and polarizability anisotropies, which were confirmed through similar comparisons.

The most significant finding of this research, however, may be related to the association of the polarizability anisotropy to the particle volume. This relationship was highlighted in the analysis of Na-montmorillonite and CNXL, and can be

extended to the QD and CNT samples as well. **Figure 9.1** shows the log of the polarizability anisotropies for the particles studied in the current work, along with those of Matsumoto and Sasai, plotted as a function of the log of particle volume. The data clearly shows a linear relationship that yields a value for the slope $m = 9670$. If the data is plotted on a linear scale, as shown by the inset of the figure, a linear relation with an intercept of zero is obtained. Thus, if we know the volume of a particle, we can estimate its polarizability anisotropy $\Delta\alpha$. In fact, the relation of size and polarizability anisotropy has been investigated by Spence J.C. et al.[1] According to the authors, studies of the protein lysozyme and the virus TMV showed that the polarizability anisotropy $\Delta\alpha'$ was approximately 30% less than the volume.

The current work clearly shows a much different relationship between the polarizability anisotropy and the particle volume; the later being approximately three to five orders of magnitude smaller. However, the results were consistent with those of other groups in similar solution environments. In addition, calculations of the total volume for the polarizability anisotropy of a 1 ml aqueous sample clearly indicate that the resulting values are not unreasonable. Taking, for instance, the volume fraction of the .16 μM QD sample studied in **Section 7** ($C_v = 2.03\text{x}10^{-7}$), it can be seen that its relative polarizability anisotropy volume ($C_v = 1.45\text{x}10^{-4}$) is still well below the total volume of the sample itself, by four orders of magnitude:

$$2.03x10^{-7}\,\frac{2.17x10^{-16}(\Delta\alpha'\ cm^3)}{3.03x10^{-19}(vol.\ cm^3)} = 1.45x10^{-4}$$

Thus, although the exact value of the polarizability is dependent on the solution environment, the qualitative agreement between our observation and that of Spence J.C. et al is quite convincing of this relation.

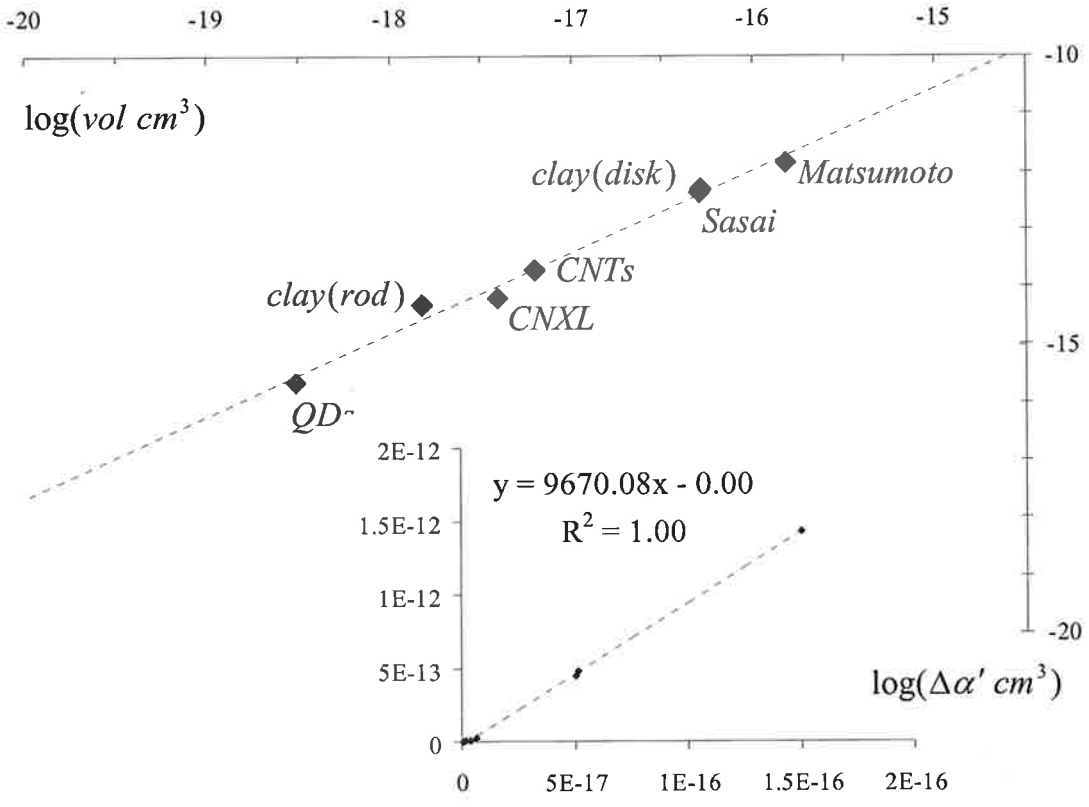

Figure 9.1: Polarizability anisotropies of the particles studied in the current research, as a function of volume. Plotted directly, the data shows a linear trend with a slope of $m = 9670$.

9.2. Future Work

We shall now examine the points which require new studies in the near future, in order to improve the theoretical and technical aspects of the methods described here and to enlarge the scope of their application. The theory of relaxation phenomena for monodisperse systems of spheroids has been well established by Benoit and is widely accepted as the governing model. However, Ridgway's treatment for the asymmetric ellipsoid has proven to be the preferred model in the current work. The relationship between the amplitudes of the two rotational diffusion coefficients was shown to follows Ridgway's theory, with one of them approaching zero as the particles being studied become more symmetrical around a primary symmetry axis. This relationship should be further explored by extending the systems of study, so that a broader range of shapes are included.

Additional work should also be done using the saturation and rise time data to calculate polarizabilities of polydisperse systems. The results here suggest that, for a system of particles containing a broad range of shapes, the two methods can be used simultaneously to determine the polarizability anisotropies of each shape class individually. Unfortunately, the direct application of the two methods is only possible in the case of a system of particles which does not contain a permanent dipole parallel to the long axis of the particles; as was witnessed by the results of the two methods in the analysis of CNXL and QDs.

Finally, the relationship between the polarizability anisotropy $\Delta\alpha$ of a particle and its volume should be further explored by applying the TEB method to a wider

range of particle sizes. In addition, the effects of ion concentration on the systems already studied, as well as any future studies, should be incorporated into the model so that an accurate representation of the scaling of $\Delta\alpha$ with volume, given a specific ionic atmosphere, can be determined.

9.3. References

1. Spence, J.C.H., et al., *Diffraction and imaging from a beam of laser-aligned proteins: resolution limits.* Acta Crystallogr., Sect. A: Found. Crystallogr., 2005. **A61**(2): p. 237-245.

Appendices

Appendix A: Dealing With Residual Light

The intensity "at rest" is given by **(3.23)**, modified as:

$$I_R = I_o \frac{(1-\cos\delta_R)}{2} \qquad \textbf{(A1)}$$

for the crossed position when $\alpha = 0$, and by **(3.22)** becomes:

$$I_\alpha = I_o \frac{1-\cos 2\alpha \cos\delta_R}{2} \qquad \textbf{(A2)}$$

when the analyzer is turned away from the crossed position and $\alpha \neq 0$. Upon application of an aligning field (analyzer and polarizer crossed), the result is:

$$I_\delta = I_o \frac{1-\cos(\delta+\delta_R)}{2} \qquad \textbf{(A3)}$$

The change in light intensity is then equal to:

$$\Delta I_\delta = I_o \frac{\cos\delta_R - \cos(\delta+\delta_R)}{2} \qquad \textbf{(A4)}$$

$$= I_o \sin(\delta/2)\sin(\delta_R+\delta/2) \qquad \textbf{(A5)}$$

and the relative change with respect to the intensity at an angle α is:

$$\frac{\Delta I_\delta}{I_\alpha} = \frac{2\sin(\delta/2)\sin(\delta_R+\delta/2)}{1-\cos 2\alpha\cos\delta_R} \qquad \textbf{(3.38)}$$

Appendix B: Physical Parameters Acquired From TEB

Parameter	Units	Description	Equations
E^2	kV^2cm^{-2}	The square of the field strength applied to the sample.	n/a
$log\ E^2$	$\log (kV^2cm^{-2})$	Log of the applied field strength; needed for the comparison of the experimental data to the theoretical curve and the determination of the percent contribution of permanent and induced-dipole to the alignment mechanism of the particles.	n/a
δ	degrees	Optical phase shift of the probe beam by the sample upon application of the alignment field.	**(25b)**
Δn	unitless	Change in birefringence of the sample upon application of the alignment field.	**(2)**
$\frac{\Delta n}{E^2}$	$cm^{-2}kV^2$	The change in birefringence divided by the squared field strength; when plotted against E^2, the y-intercept can be used along with the volume fraction of the molecule C_v to determine the sample's optical anisotropy Δg.	**(60)**
$\frac{\Delta n/E^2}{\Delta n/E^2_{\to 0}}$	unitless	The change in birefringence divided by the squared field strength and normalized to its low-field limit; when plotted against $log\ E^2$, the slope at intermediate fields can be used to determine the percent contribution of permanent and induced-dipole to the alignment mechanism of the particles.	**(61c)**
$\langle P_2 \rangle$	unitless	The alignment parameter for the sample solution.	**(44)**
Δg	unitless	Optical anisotropy of the sample; used in combination with the specific Kerr constant K_{sp} to determine the anisotropy in the polarizability of the particles.	**(40)** **(65)**
K_{sp}	m^2V^{-2}	Specific Kerr constant; determined using the volume fraction of the sample C_v and the birefringent response at the low field limit where $E \to 0$.	**(64)**

Appendix C: Carbon Nanotubes

In this section, I will discuss some alignment properties of carbon nanotubes (CNTs) which were used as a filler in a polymer composite. The following sections outline the TEB results and analyses, following the same procedure as that used for other nanomaterials in this thesis.

C1. Experimental

Hydroxide functionalized Carbon nanotubes were used as supplied by Cheap Tubes. Approximately 2 mg of nanotubes were added to Millipore deionized water and ultrasonicated for 20 minutes. The suspension was left to stand for 24 hours and then filtered through a 2 μm ceramic filter. The concentration of the subsequent stock solution was determined to be $3.2x10^{-3}$ %wt by evaporation of a known volume of solution to dry weight. Sample solutions were prepared from the stock solution by the direct addition of deionized water. A TEM image of tubes taken from the stock solution can be seen in **Figure C1**.

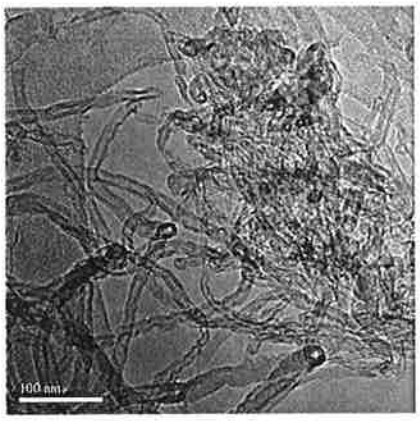

Figure C1: TEM image of tubes taken from the stock solution used for the current work.

Outside diameter: ~ 10 nm

Length: .5 – 2 μm

C2. Concentration Dependence of D_R

Field free relaxation studies were conducted using carbon nanotube (CNT) solutions with concentrations from $1.6x10^{-3}$ %wt down to $2.0x10^{-4}$ %wt. The amplitudes for the two exponential decay functions, D_R(slow) and D_R(fast), from **Section 4.9** were .99 and .01 respectively. The seemingly single exponential decay property of CNT parallels the results for QDs in **Section 7.3**. We tentatively attribute this result to the uniform coherent length of the particles. **Figures C2 & C3** show the two decay constants D_R(fast) and D_R(slow) at varying concentrations as a function of field strength. The variations for both the fast and slow rotational diffusion coefficients are very similar. In both cases a steady increase in the value of D_R occurs for the concentration of $1.6x10^{-3}$ %wt.; whereas at lower concentrations, it is essentially constant. This suggests that any concentration at or below $.8x10^{-3}$ %wt. should be free of inter-particle interactions. Calculations for the average tube length based on the fast and slow rotational diffusion coefficients were done using Eq. **(4.68)** and displayed in **Table C1**.

Table C1: Average lengths and diameters for aqueous CNT based on a slow and fast rotational diffusion coefficient.

% wt 10^3	D_R (s^{-1})		rod length (nm)		rod diameter (nm)	
	fast	slow	fast	slow	fast	Slow
0.8	996 ± 164	87 ± 6	254 ± 13	572 ± 14	4.3 ± .1	9.5 ± .3
0.4	970 ± 169	75 ± 6	257 ± 15	601 ± 17	4.2 ± .1	10.0 ± .3
0.2	934 ± 99	81 ± 5	259 ± 9	585 ± 13	4.3 ± .2	9.7 ± .4
	967 ± 139	**81 ± 8**	**256 ± 12**	**586 ± 19**	**4.2 ± .1**	**9.7 ± .4**

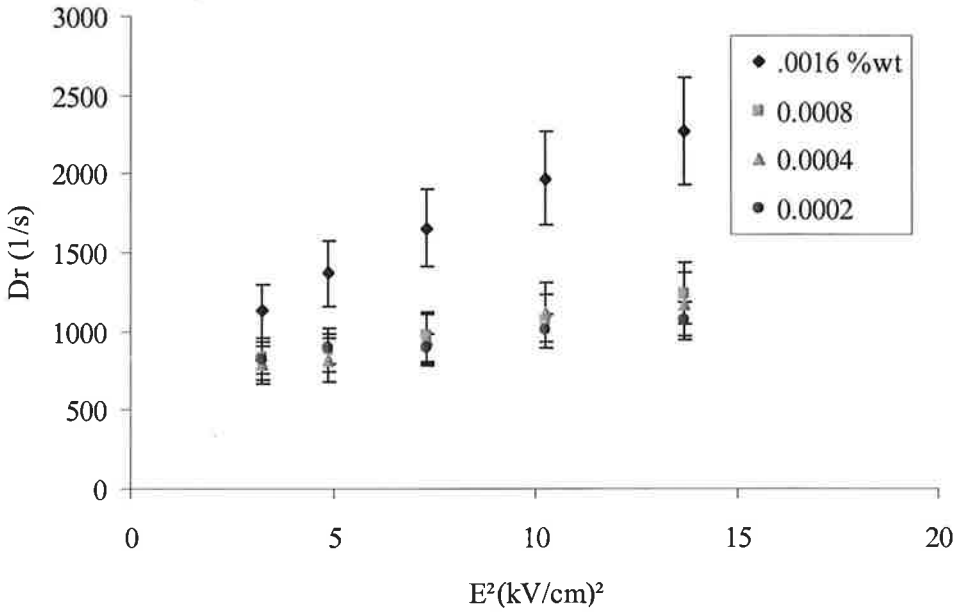

Figure C2: "Fast" rotational diffusion coefficients D_R for carbon nanotubes at varying concentrations as a function of the squared field strength.

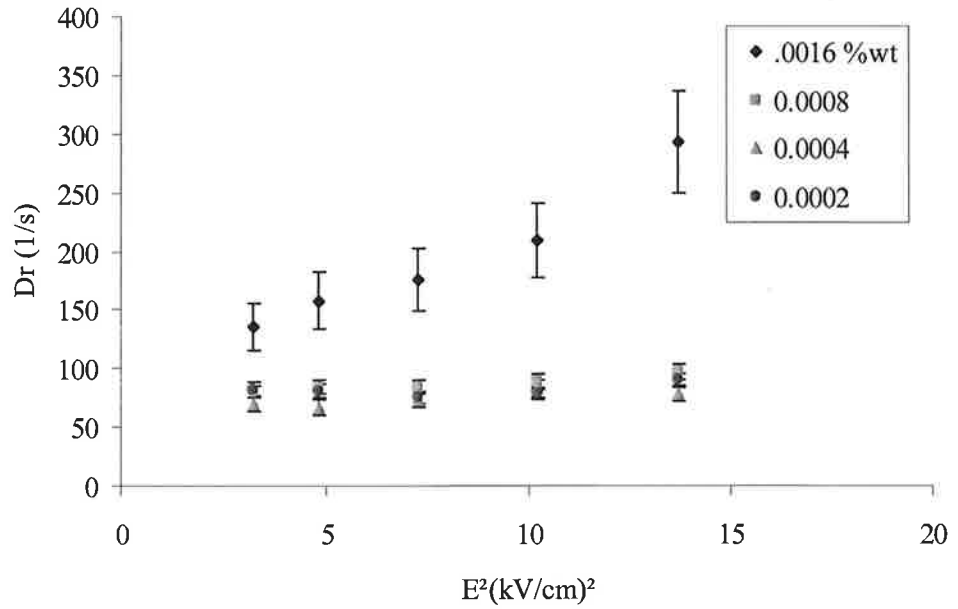

Figure C3: "Slow" rotational diffusion coefficients D_R for carbon nanotubes at varying concentrations as a function of the squared field strength.

C3. Saturation of the Birefringent Response

The birefringent responses for a $8.0x10^{-3}$ %wt carbon nanotube sample, subjected to fields between .02 and 1.5 kV/cm were recorded after averaging over 128 pulses at 2 Hz, with a pulse width of 500 μs. The change in birefringence Δn at each field was calculated according to Eq. **(3.35)** for an optical arrangement with a quarter-wave plate. **Figure C4** shows the plot of $\Delta n/E^2$ vs. $logE^2$, normalized to its low field limit, for a series of CNT samples. The slope of -0.97 at intermediate field strengths, when combined with Eq. **(4.26)**, results in an estimated contribution of $[.27\beta^2 + .73(2\gamma)]$ toward the alignment mechanism from the permanent and induced-dipoles. The presence of a permanent dipole can be rationalized when we consider the existence of chiral tubes. Upon OH functionalization, the chiral tubes can lead to a permanent dipole along the tube axis.

Extrapolation of the birefringence to the infinite field yielded a saturation value of $\Delta n_s = 3.71x10^{-9}$. When combined with the calculated value for the volume fraction, the optical anisotropy was determined to be:

$$\Delta g = \frac{\Delta n_s n}{2\pi C_v} = \frac{(5.06x10^{-6})(1.33)}{2\pi(1.52x10^{-5})} = 7.03x10^{-2}$$

This value is in good agreement with the optical anisotropy of $\Delta g = 1.02x10^{-2}$ determined by Donovan and Scott.[1] A plot of $\Delta n/E^2$ vs E^2 yielded a y-intercept of $5.06x10^{-6}$ cm^2kV^{-2} when extrapolated by to $E = 0$. When combined with Eq. **(4.28)**, the specific Kerr constant K_{sp} was calculated as the following:

$$K_{sp} = \frac{5.06x10^{-6}\,cm^2kV^{-2}}{(1.52x10^{-5})(1.33)} = 1.55x10^{-3}\,cm^2kV^{-2}$$

$$= \underline{\underline{1.55x10^{-13}\,m^2V^{-2}}}\,(SI\ units)$$

A horizontal shift of .89 was necessary to align the experimental data with the theoretical curve. Using the logarithmic relation in Eq. **(4.30)**:

$$P + Q = 1.29x10^{-11}\,m^2V^{-2}$$

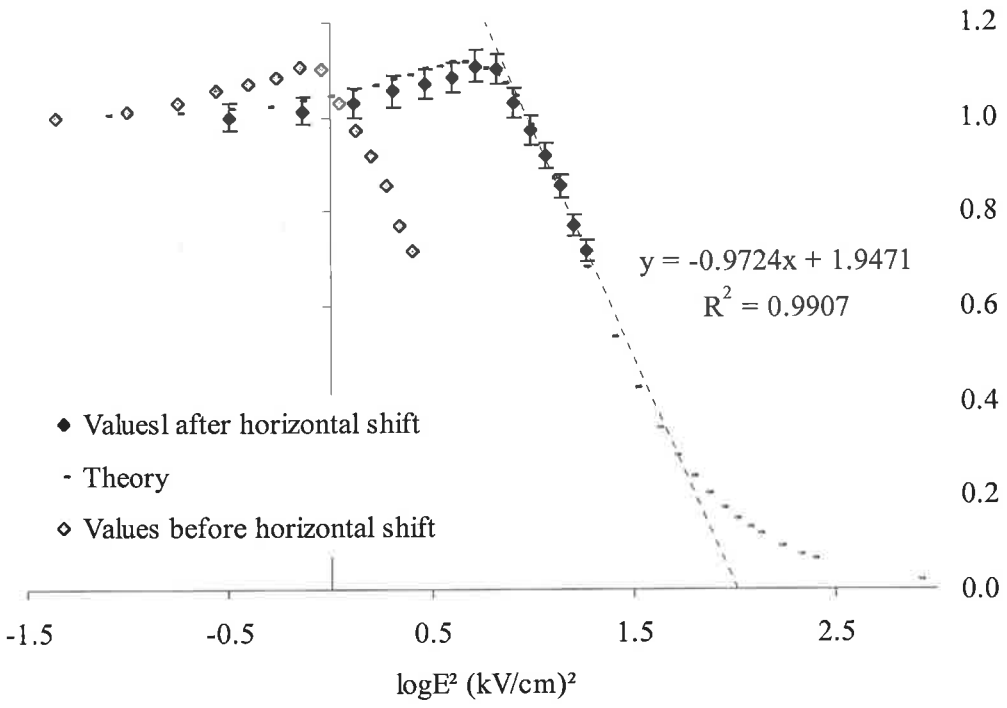

Figure C4: Normalized plot of $\Delta n/E^2$ vs. $logE^2$ for a CNT sample laid over the theoretical curve for an alignment mechanism represented by the ratio $[.27\beta^2 + .73(2\gamma)]$.

The polarizability anisotropy and permanent dipole moment of the carbon nanotubes are then obtained using Eq. **(4.29)**:

$$\Delta\alpha = 5.24x10^{-32}\,Fm^2 \qquad \mu = 1.92x10^{-27}\,Cm$$

$$\Delta\alpha' = 4.69x10^{-16}\,cm^3 \qquad \mu = 5.75x10^{2}\,D$$

C4. Conclusion

The above results suggest that the nanotubes can be aligned in an electric field. Although the exceedingly large aspect ratio makes the tubes rope like, a uniform coherence length is observed. Consequently, the response of CNT to an external field is identical to that of a monodisperse rod system. The strong alignment response, an order of magnitude faster than their decay, makes them a reasonable candidate for the synthesis of polymer composites containing aligned fillers.

C5. References

1. Donovan, K.J. and K. Scott, *Transient electric birefringence in suspensions of single-walled carbon nanotubes.* Physical Review B: Condensed Matter and Materials Physics, 2005. **72**(19): p. 195432/1-195432/8.